Active Layer Modification of Organic Photovoltaics – Studying Structural Impacts of Conjugated Polymer and Using Nanowires as Electron Transport Pathways

Pinyi Yang

A Doctoral Thesis
submitted in partial fulfillment of the
requirements for the degree of

Doctor of Philosophy

University of Washington

2013

Program Authorized to Offer Degree:
Materials Science and Engineering

Abstract

The potential of organic photovoltaics (OPVs) to be a low-cost and low-carbon renewable energy source has generated great interest in this field over the last decade. To obtain OPVs with higher efficiency, efforts have been devoted to improving the properties of the active layer materials (the conjugated polymers and n-type materials), improving the fabrication processes, and understanding the many operating mechanisms. Besides the intrinsic materials properties, the morphology of the active layer has also been found to dramatically affect the performance of OPVs. Among these studies, two strategies are often used to develop OPVs with higher efficiency: (1) Develop new device structure; (2) Design and synthesize conjugated polymer with better properties for OPV application. In this thesis, a project based on each strategy will be discussed. The first strategy leads to a serial studies and process method developments on using inorganic nanomaterial as charge transport pathways in OPVs (Chapter 2). On the other hand, as understanding the structure-property relationship of conjugated polymers is very helpful in using the second strategy to improve OPVs, two different structures -- silafluorene containing multi-fused heptacylic arenes as the donor in donor-acceptor conjugated polymer and fluorine substituents on the conjugated polymer backbone will be included in Chapter 3.

Table of Contents

List of Figures

List of Tables

1. Introduction

1.1 Solar Energy

Throughout the 21st century, our energy consumption has been increasing rapidly. Among the vast number of energy sources, the most common are fossil fuels (Figure 1.1(a)). Since they are non-renewable and release large amounts of carbon dioxide (CO_2,, Figure 1.1(b)) to the atmosphere, their over-consumption increases fuel prices and generates pollution, causing environmental problems.

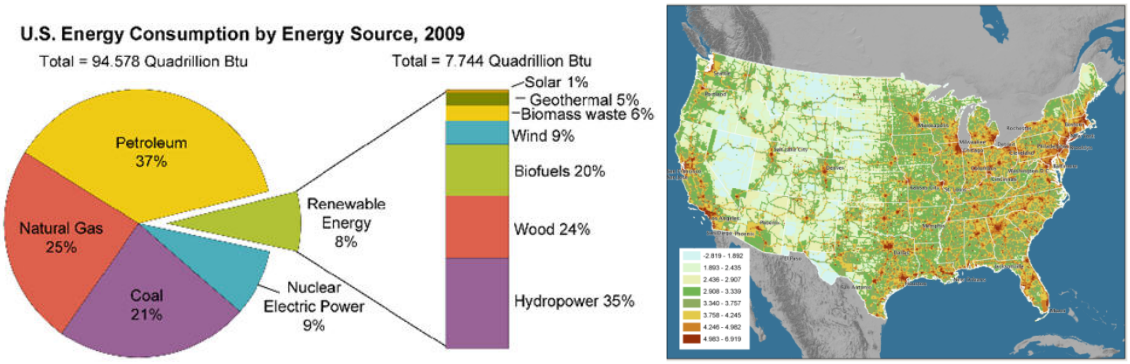

(a) (b)

Figure 1.1 (a) U.S. energy consumption by source[1] (b) CO_2 production in the U.S.[2]

As predicted by many people,[3,4] the need for clean and renewable energy, such as wind and solar energy, is urgent. Among the different types of renewable energy sources, solar power is one of the most attractive. The sun continually provides enormous amounts of energy to Earth. For example, in some places in Arizona, the solar energy density can reach as high as 8 kWh/m^2 per day (Figure 1.2(a)).[5] If we could capture and convert all of the solar energy shining on the State of Arizona to electricity, it would be more than enough to satisfy all the energy usage of the entire United States.[5]

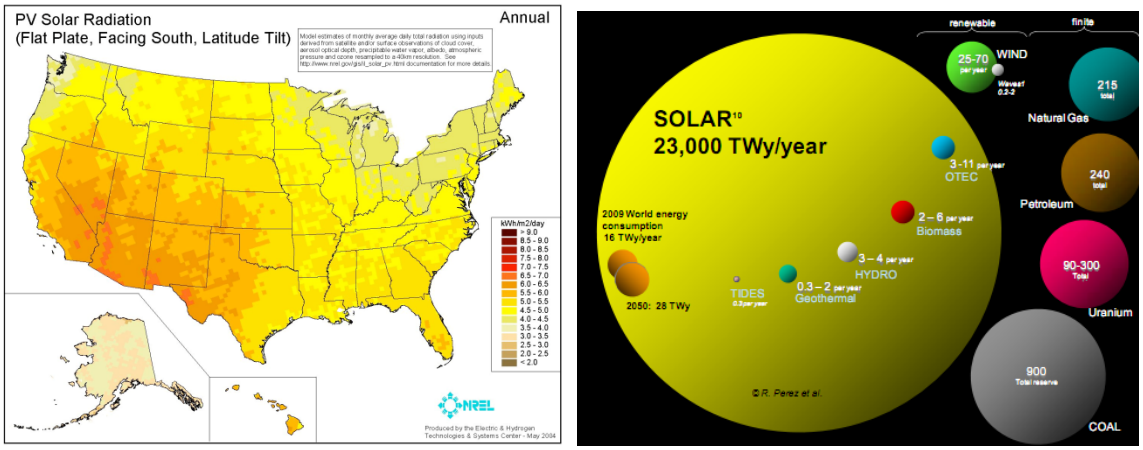

(a) (b)

Figure 1.2 (a) Photovoltaic solar radiation power over United States.[5] (b) Solar energy power comparing with other types of renewable energy and global energy consumption.[6]

It is true that solar power is unevenly distributed all over the world; sunlight may not be able to provide remarkable amounts of energy to countries near the poles. However, when the total available power of incident sunlight is compared to the availability of other renewable energy sources (Figure 1.2(b)), this disadvantage becomes trivial. Incident solar power can be as high as 86,000 TW, 100 times available wind power and nearly 6,000 times current global energy consumption.[6] It is this wealth of untapped renewable energy that makes solar energy appealing.

Solar cells are the devices used to convert energy from sunlight into electricity by the photovoltaic effect. Conventional solar cells, made from inorganic materials, are efficient at converting solar power into electrical power: the world record solar cell is capable of a 42.8% conversion efficiency.[7] Power conversion efficiency (PCE) is the ratio of the electrical power a solar cell produces to the solar power incident upon the device. The PCE of a commercially-available mono-crystalline silicon solar cell is around 25%

(Figure 1.3).[8] This efficiency is sufficient to meet current electricity demands. However, most inorganic solar cells are made from high-purity silicon, which is required in the information technology (IT) industry as well. The competition for this high-purity Si between the solar industry and IT industry raises the price of high-purity silicon and makes inorganic solar cells prohibitively expensive for residential usage. As a result, scientific research has been devoted to finding affordable solar cells appropriate for individual usage.

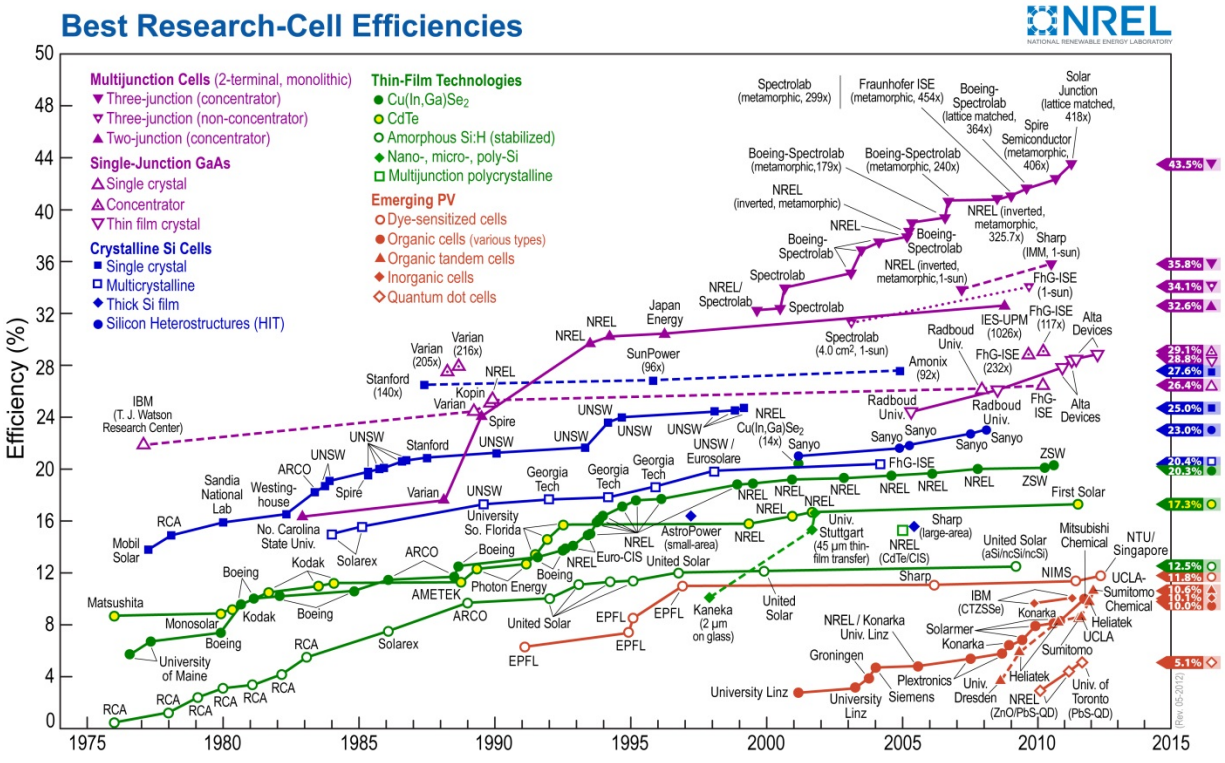

Figure 1.3 Best research-cell efficiencies of various solar devices.[8]

1.2 Organic Solar Cell

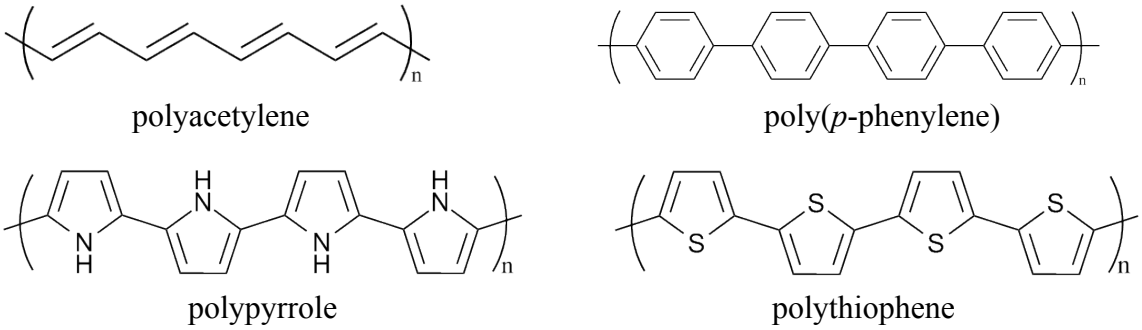

polyacetylene poly(*p*-phenylene)

polypyrrole polythiophene

Figure 1.4 Examples of conjugated polymers

Ever since conjugated polymers were found to be able to convert light into electricity,[9,10] they have attracted a lot of interest because of the possibility of creating cheaper organic electronic devices compared to their inorganic counterparts. Generally speaking, a conjugated polymer is a polymer with alternating single and double or triple bonds (Figure 1.4).[11,12] Within such a polymer, a delocalized π electron system forms, much the same as in an inorganic semiconductor.[13–17] Due to their low cost and the possibility of solution processability, a significant amount of expense can be cut by fabricating solar cells from organic materials, rather than inorganic materials.[18] However, a key issue of organic photovoltaics (OPVs) is the low efficiency; it is commonly thought that a 10% PCE is needed to make them commercially viable.[19]

The main obstacle of organic solar cells is the exciton formation on the conjugated polymer – after absorbing light, excitons (electrostatically-bound electron-hole pairs) are generated, which can only diffuse about 10 nm (Figure 1.5(a)) before recombination.[20] One way that has been found to overcome the small exciton diffusion length is to utilize a bulk heterojunction (BHJ) structure.[21,22] This active layer structure can be easily achieved

by spin-coating a blend solution of electron donor (conjugated polymer) and acceptor (usually a fullerene derivative) (Figure 1.5 (b), (c)). Upon annealing the spin-coated layer, the two components separate into two phases.[23] During this process, the size of the phase separation and morphology of active layer can be controlled by using different solvents,[23,24] and by controlling the solution evaporation rate.[25,26] It has also been found that the BHJ morphology can be further tuned by thermal treatment near the glass transition temperature of the conjugated polymer. All these methods are aimed to tailor the active layer architecture into the optimal condition for exciton diffusion and separation.

Other effects have also been used to further improve the PCE of organic solar cells. Buffer layers such as Ca and LiF[27–29] have been introduced between the top electrode and active layer to adjust energy levels for better charge collection and to protect the polymer from the hot metal source during electrode deposition.

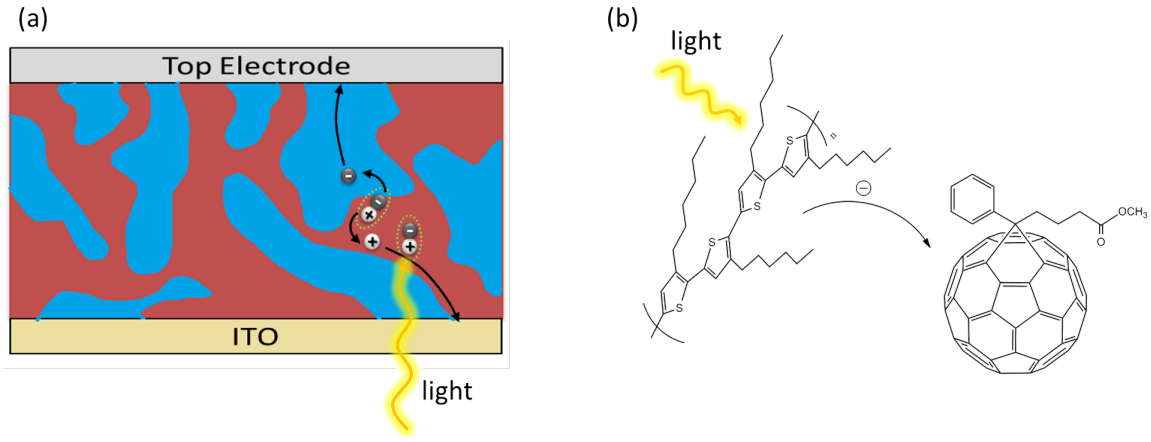

Figure 1.5 (a) Bulk heterojunction device structure. (b) Exciton separation between P3HT and PCBM.

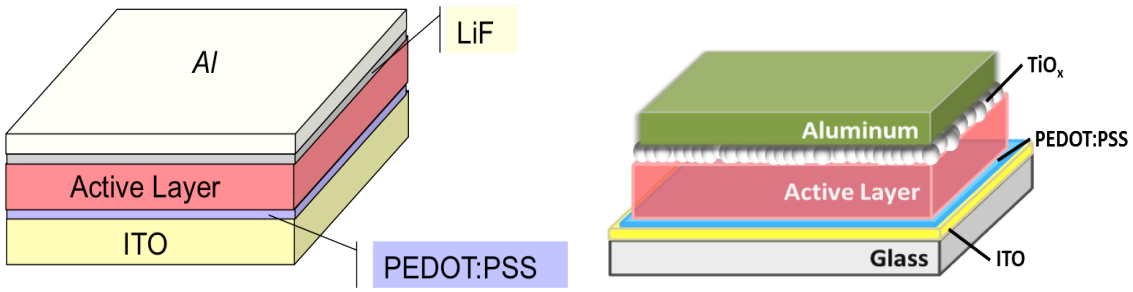

Figure 1.6 (a) Conventional device structure with LiF as buffer layer and Al as top electrode. (b) Conventional device structure with TiO_x as optical spacer and Al as top electrode.

The use of an optically transparent TiO_x layer[30,31] has been found not only to have a similar function as Ca and LiF buffer layers, but also serves to enhance the light absorption of OPVs. Additionally, a thin layer of PEDOT:PSS (about 20 to 30 nm) is generally used as a hole-transport layer (HTL) on the transparent indium tin oxide (ITO) to mediate the organic BHJ-inorganic ITO interface and enhance hole-collection on the ITO side.[29-31]

Additional improvements in the OPV area have been accomplished by novel device structures such as inverted structures,[32–35] solar power wires[36] and tandem organic solar cells.[37–42] With these modifications, a conventional structure solar cell with P3HT:PCBM active layer can achieve efficiencies around 5%.[43] Further improvement has come from the development of both novel p-type (PCDTBT,[44] PBDTTT-CF,[45] PDTSTPD[46] and PSBTBT[47]) and n-type ($PC_{61}BM$,[43] $PC_{71}BM$[48,49] and ICBA[50,51]) materials (Figure 1.7). With the use of these materials PCEs as high as 8.37% have been achieved in single-junction organic solar cells (organic solar cell with single active layer).

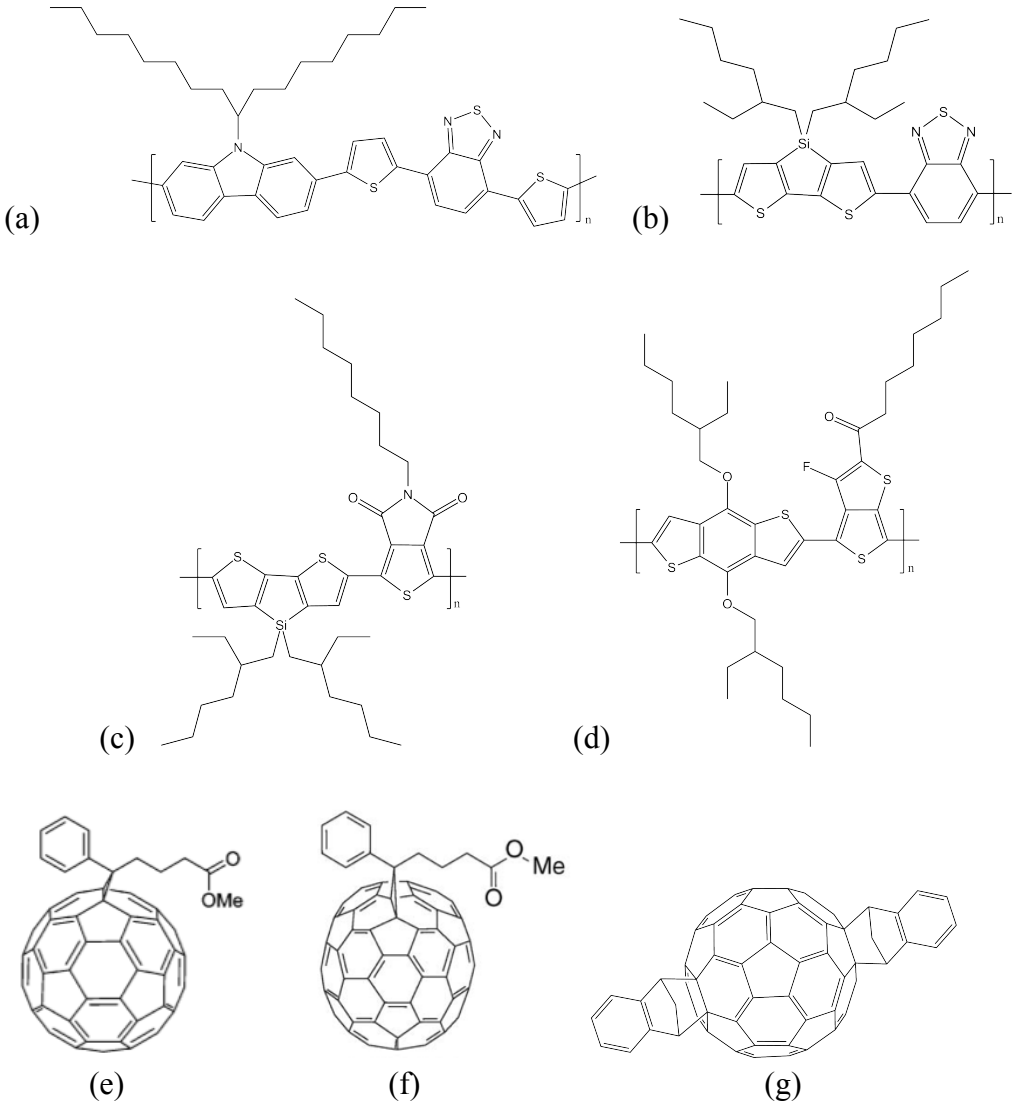

Figure 1.7 Molecular structure of (a) PCDTBT (b) PSBTBT, (c) PDTSTPD, (d) PBDTTT-CF, (e) $PC_{61}BM$, (f) $PC_{71}BM$ and (g) ICBA

These various ways of improving the performance of organic solar cells can be categorized into two strategies. One is interfacial modification, which usually consists of an extra layer introduced into solar cell, typically between one of the electrodes and the active layer. The buffer layer, optical spacer and PEDOT:PSS layer modifications are examples of this strategy. The other strategy mainly aims at improving properties of the

active layer. This includes synthesizing new materials that absorb more light or improve charge carrier transport, and optimizing the active layer morphology by annealing or by other methods.

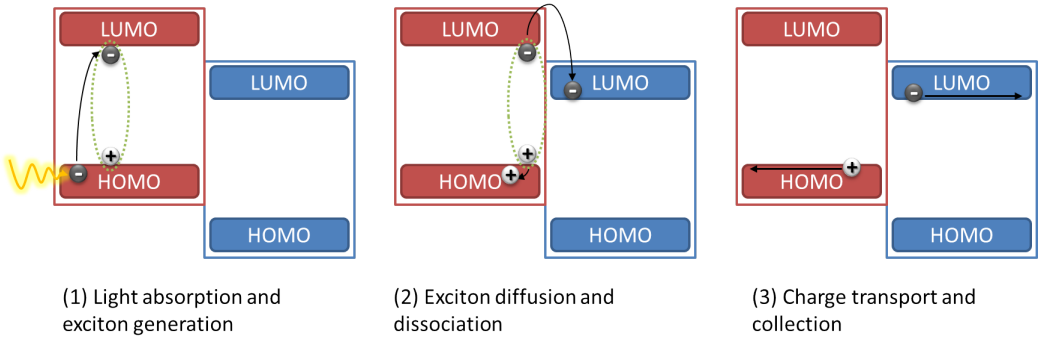

Figure 1.8 Main steps to produce photocurrent inside organic solar cells.

The main purpose to optimize the active layer morphology is to control its phase separation. In organic solar cells, there are three main steps involved in the operation to produce photocurrent: (1) light absorption and exciton generation; (2) exciton diffusion and dissociation and (3) charge transport and collection (Figure 1.8). The light absorption of an organic solar cell is primarily dependent on the materials of its active layer.[52,53] Meanwhile, exciton dissociation and charge transport are highly dependent on the morphology of the active layer.[54,55] The morphology of the active layer can either facilitate exciton separation or charge transport conditions by discouraging or encouraging phase separation (also increasing or decreasing donor-acceptor interfacial surface area), respectively. An active layer with insufficient phase separation is shown in Figure 1.9 (a). Although excitons can be dissociated efficiently, the power conversion efficiency of a cell containing this morphology in the active layer will be low due to lack

of a continuous or sufficiently conductive pathway to collect free charges. Alternatively, an active layer with excessive phase separation is shown in Figure 1.9(b). Although charges can transport freely to the electrodes, the PCE of the solar cell containing this morphology in the active layer will also be low because few excitons are able to separate to produce free charges. One solution to this issue is to control the degree of phase separation, feature size, and crystallinity of the active layer during the solar cell fabrication process. This can be accomplished through various treatment such as thermal annealing,[56–58] solvent annealing[59–61] and solvent additives[62–64]. In this manner, the morphology of active layer can be tailored to the proper size resulting in balanced exciton dissociation and charge transport (Figure 1.9 (c)), which can increase the PCE of the final solar cell.

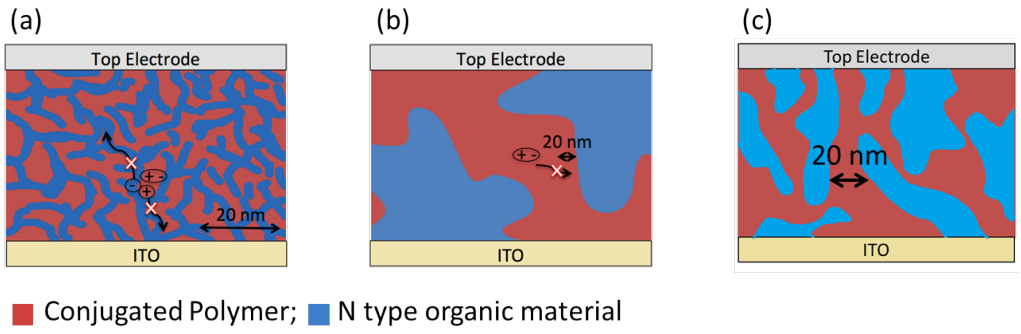

Figure 1.9 Active layer of organic solar cell with (a) insufficient phase separation, (b) excessive phase separation and (c) proper phase separation (balanced exciton dissociation and charge transport ability)

1.3 Photovoltaic Characterization

Photovoltaic devices are characterized in the lab, under the standard AM1.5G solar spectrum (Figure 1.10) developed and defined by the photovoltaic (PV) industry, in

conjunction with the American Society for Testing and Materials (ASTM) and government research and development laboratories.[65] Its incident power is 1000 W/m^2. This is accomplished by irradiating the cells under a spectrally matched and calibrated light source. The organic solar cells are connected to a source measurement unit to measure their current-voltage characteristics (*I-V* curve Figure 1.11) are measured. The *I-V* curve is a plot of the current produced by a solar cell versus applied voltage under a given light intensity.[66] The dark *I-V* curve is tested without any illumination, and shows the diode behavior of organic solar cell. Under illumination, photon current will be generated inside solar cell. Accordingly, the *I-V* curve will be shifted towards negative currents.

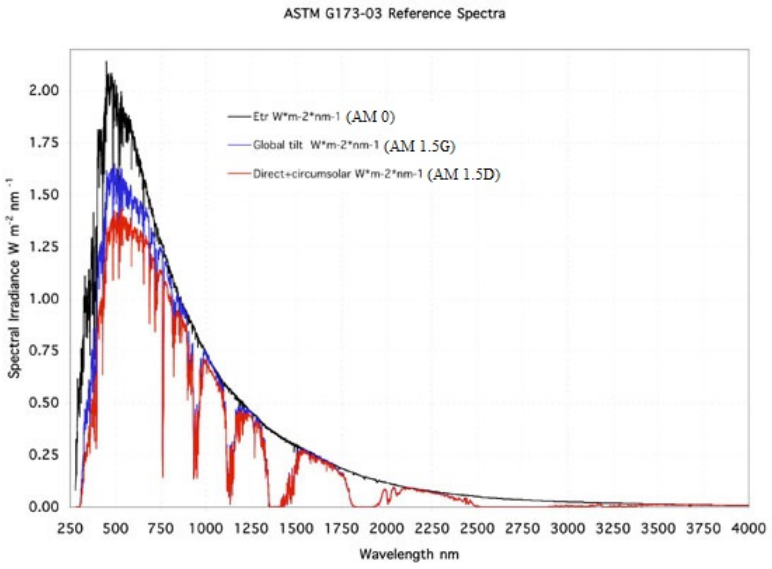

Figure 1.10 AM 1.5 solar spectrum used in the *I-V* characterization of solar cells.[65]

Important device parameters can be determined by the *I-V* curve including short-circuit current (I_{sc}), open-circuit voltage (V_{oc}), fill factor (FF) and power conversion

efficiency (PCE). The short-circuit current (I_{sc}) is the current that flows through the solar cell without an applied bias. The V_{oc} is the voltage at which no current flows through the device. In an organic solar cell, the value of V_{oc} has been found to strongly depend on the energy difference between the highest occupied molecular orbital (HOMO) of the donor material and lowest unoccupied molecular orbital (LUMO) of the acceptor material.[52] Thus, designing materials with appropriate HOMO and LUMO level offsets is one way to obtain a high V_{oc}. The FF is defined as the ratio of the current and voltage at the maximum power point (P_{max}) to the product of the short-circuit current and open-circuit voltage.

$$FF = \frac{P_{max}}{I_{sc}V_{oc}} = \frac{I_{max}V_{max}}{I_{sc}V_{oc}} \quad (1)$$

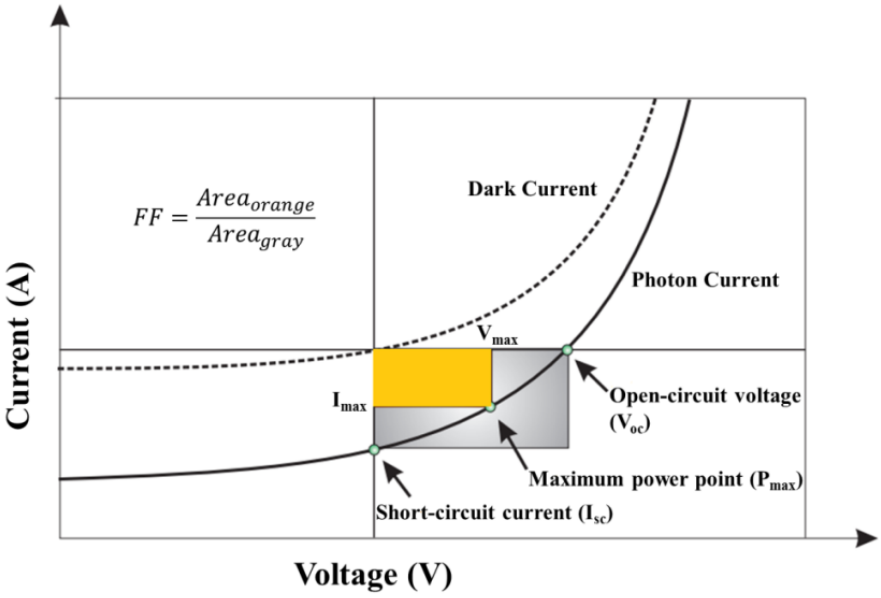

Figure 1.11 Typical Photon and dark current-voltage characteristics (*I-V* curve) for a solar cell.

The PCE is the most important parameter of a solar cell. It is the ratio of maximum electrical power (P_{max}) produced by the cell to the power of incident light (P_{light}).

$$\mathrm{PCE} = \frac{P_{max}}{P_{light}} = \frac{I_{sc}V_{oc}}{P_{light}}\mathrm{FF} \tag{2}$$

Equation (2) can be further modified by dividing both I_{sc} and P_{light} by device area which yields Equation (3) shown below,

$$\mathrm{PCE} = \frac{\frac{I_{sc}}{s}V_{oc}}{\frac{P_{light}}{s}}\mathrm{FF} = \frac{V_{oc}J_{sc}}{J_{light}}\mathrm{FF} \tag{3}$$

Where, J_{sc} is the short-circuit current density of solar cell, and J_{light} is the incident light power density. In order to improve the PCE of a solar cell, the FF, J_{sc}, and V_{oc} need to be simultaneously maximized.

1.4 Outline

Our work focuses on applying the active layer modification strategy to improve the properties and morphology of the active layer by making innovations or modifications during the processing. In our research, two methods have been applied and investigated: one, active layer property modification by introducing nanostructured materials as improved electron transport pathways and two, cooperating with chemists to develop new active layer materials through chemical synthesis.

This report focuses on improving organic solar cells by incorporating nanostructured materials to improve electron transport pathways, while keeping the advantages (low cost,

solution processability and flexibility) of organic solar cells intact. This report addresses the selection and characterization of nanostructured materials and details the development of a method to modify OPV device fabrication methods to incorporate said nanostructured materials. Finally, this report serves to assess the influence of adding nanostructured materials as improved electron transport pathways on the operation of organic solar cells. Chapter 2 delineates the experiments and summarizes the research results of incorporating improved electron transport pathways into organic solar cells. Chapter 3 describes the synthesis and solar cell characterization of a new variety of low bandgap copolymers that contain a multi-fused thienyl-fluorene-thienyl subunit.

2. Incorporating Improved Electron Transport Pathways into Organic Solar Cells

2.1 Introduction

The goal of this research is to develop an alternative way to optimize the PCE of organic solar cells by incorporating nanostructured materials to improve the electron transport pathway in the active layer. The nanostructured materials are designed to have good charge transport ability through which free charges can be extracted from the active layer. Meanwhile, they are also expected to have sizes larger than the phase size of active layer material so that separated phases can be bridged to provide continuous and high-mobility pathways to electrons to move across the active layer. The resulting electron transport characteristics in devices fabricated using the additional nanostructured materials is expected to be better than charge transport optimized by merely controlling the phase separation. At the same time, as the nanostructured materials are responsible for the charge transport, the phase separation of active layer can be controlled to prefer exciton dissociation. Thus, with nanotubes or nanowires as electron transport pathways, it is possible to achieve organic solar cells with both improved exciton dissociation and charge transport abilities.

2.2 Effect of TiO_2 Nanotube Aggregates (TiO_2-NA)

Due to the wide application and successes of TiO_2 nanotube aggregates in dye-sensitized solar cell as electron transporting material,[67–69] they were chosen as to modify

the most common organic solar cell active layer consisting of poly(3-hexyl thiophene) (RR-P3HT; P3HT) and [6,6]-phenyl-C_{61}-butyric acid methyl ester (PCBM) (Figure 2.1).[70–75]

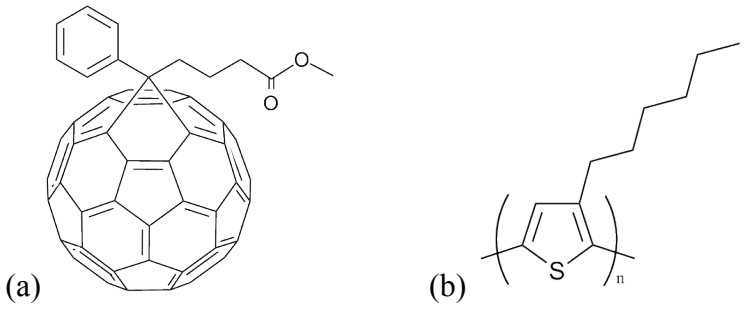

Figure 2.1 Chemical structure of a) PCBM, and b) P3HT

2.2.1 Results and Characterization

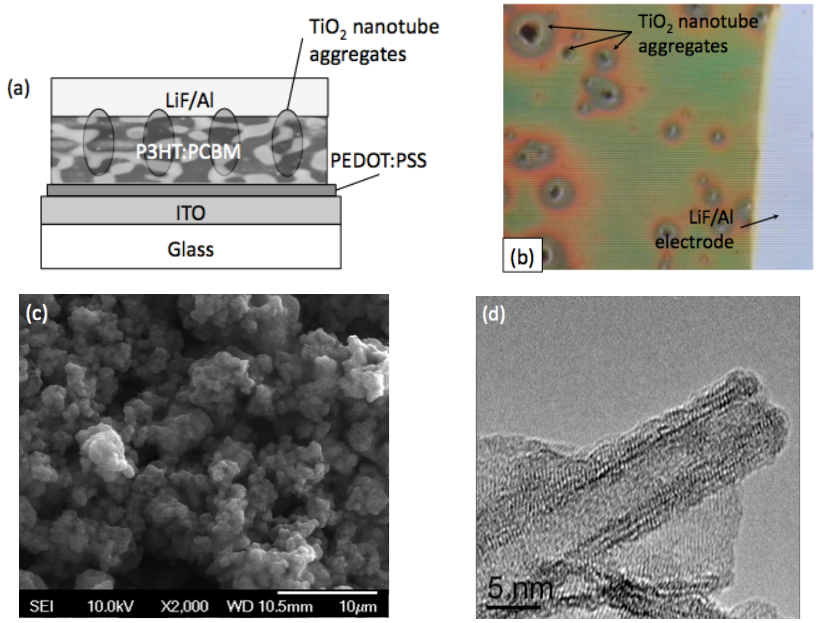

Figure 2.2 (a) Schematic diagram of solar cells with TiO_2 nanotube aggregates. (b) Optical microscope image of surface of solar cell with TiO_2 nanotube aggregates (×500). (c) SEM image of TiO_2 nanotube aggregates. (d) TEM image of a TiO_2 nanotube inside the aggregates.

Figure 2.2(a) illustrates a simplified structure of a solar cell with TiO_2 nanotube aggregates. In the scanning electron microscope (SEM) image of the TiO_2 nanotube aggregates (Figure 2.2(c)), it can be seen that TiO_2 nanotube aggregates is formed by a large number of TiO_2 nanotubes with a dimension of approximate 10 nm in diameter (Figure 2.2(d)). Because the size of aggregates (300~600 nm in diameter) are larger than the thickness of a P3HT:PCBM film (140 nm), they will cause bumps on the surface of active layer around it. This means the surface roughness of film will be increased by adding in TiO_2 nanotube aggregates. The increase in roughness was confirmed by the AFM images of the films with and without TiO_2 nanotube aggregates (Figure 2.3 (a)~(c)). For the conventional film (Figure 2.3(a)) the surface is very smooth having a root mean average (rms) roughness of only 0.63 nm. But for the film with TiO_2 nanotube aggregates, the rms roughness of the film increases, especially in the area close to the aggregates. In the area some distance away from the aggregates, the rms roughness is a little higher than the normal film reaching 0.95 nm (Figure 2.3(b)), while this value jumps to 1.92 nm (Figure 2.3(c)) when scanning around a medium size TiO_2 nanotube aggregate.

Furthermore, Figure 2.2(b) shows the optical microcroscopy image of the actual film that due to the poor control we had during processing, the size and distribution of the TiO_2 nanotube aggregates were not very uniform. Surprisingly, the final devices showed little shorting.

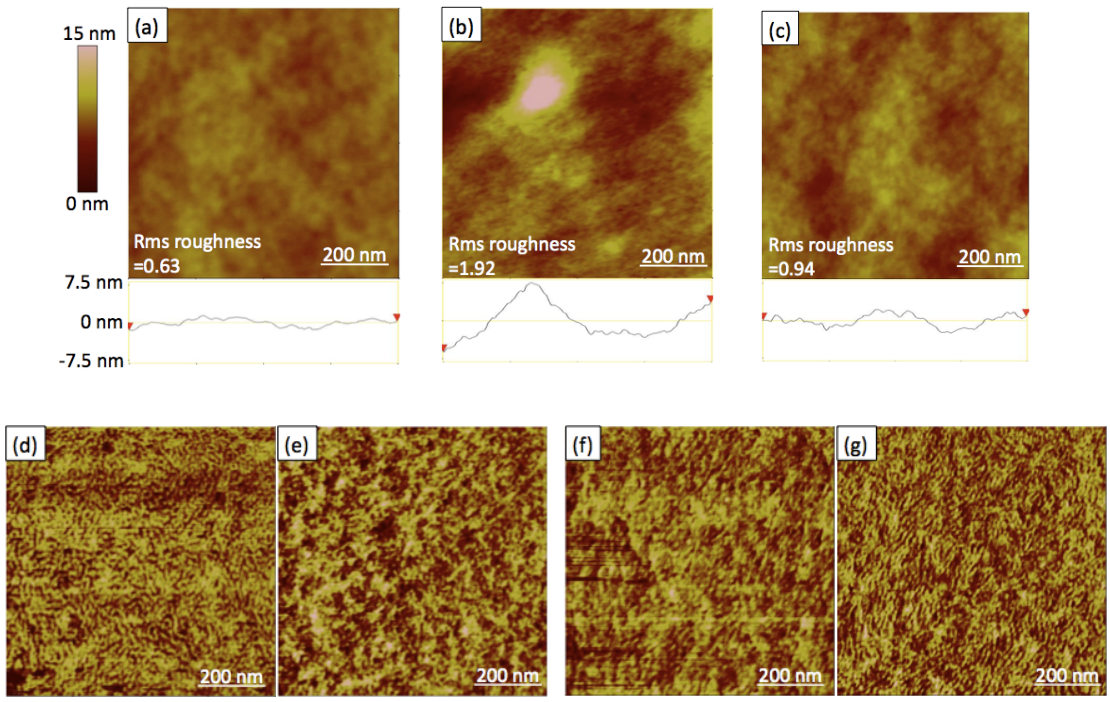

Figure 2.3 (a) AFM images of normal P3HT/PCBM active layer; AFM images of active layer with TiO_2 nanotube aggregates (b) near an aggregate and (c) some distance from an aggregate. Phase image of P3HT:PCBM film with TiO_2 nanotube aggregates annealed at 150 ˚C for 5 min (d) near an aggregate, (e) some distance away from an aggregate; Annealed for 9 min (f) near an aggregate, (g) some distance away from an aggregate.

The *J-V* curves of the best control device (annealed for 9 min) and the best devices with the TiO_2 nanotube aggregates annealed for 5 and 9 min are shown in the Figure 2.4. The power conversion efficiency () of the control sample is 2.8%. Under the same annealing conditions, efficiency of device with TiO_2 nanotube aggregates increased to 3.0%. Moreover, for devices modified by TiO_2 nanotube aggregates, even higher performance was reached by annealing for 5 min, with V_{oc}=0.68 V, J_{sc}=8.0 mA/cm^2, FF=0.60, PCE=3.2%. Compared to the control sample, the PCE value increased by 15%. In Figure 2.4, it can be seen that the value of J_{sc} and V_{oc} of all three devices were almost the same as each other. The 15% increase in device

efficiency can be attributed to the increase in FF in the TiO_2 containing samples, which is indicated by the area between the coordinate axis and the *J-V* curve.

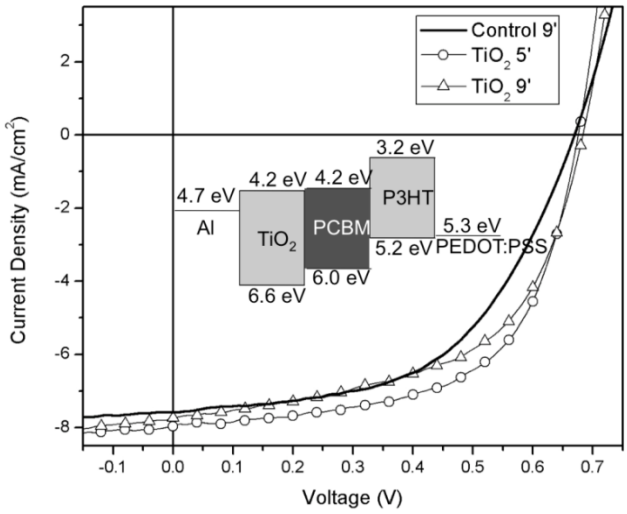

Figure 2.4 *J-V* curve of devices with normal active layer and active layer with 0.002 mol/100 mL TiO_2 nanotube annealed by different time at 150 ˚C

The change in device parameters were more clearly revealed in the summary of the average device performance in both types annealed from 4 to 10 min (Table 2.1 and Figure 2.4). Again, the values of V_{oc} and J_{sc} (Figure 2.5(a)) remained almost the same after adding TiO_2 nanotube aggregates, except the maximum J_{sc} of TiO_2 nanotube aggregates containing device appeared at 5 min annealing time. We believe that this early optimization of short current may be a result of the quicker phase change near the TiO_2 nanotube aggregates due to the higher thermal conductivity of TiO_2 compared to polymers. Because the region near the TiO_2 nanotube aggregates was heated faster than the rest of the film, the phase separation around the aggregates reached the optimal morphology after only 5 min. As shown in the AFM phase

images (Figure 2.3 (d)), after annealing for only 5 min, the area adjacent to the TiO_2 nanotube aggregates formed features which were approximately 20 nm in size (most suited for exciton dissociation), while a longer time (9 min) was needed to optimize for the regions further away from the TiO_2 aggregates (Figure 2.3(g)). After 9 min of annealing, the feature size of the area near the TiO_2 nanotube aggregates has already exceeded the optimal morphology with features with sizes greater than 100 nm appearing (Figure 2.3(f)).

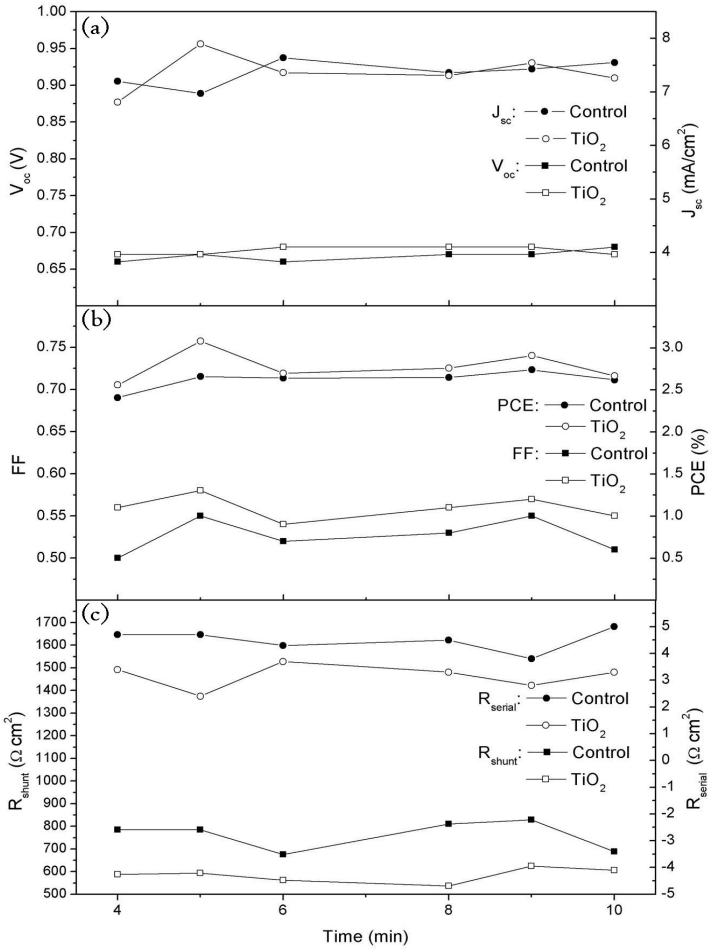

Figure 2.5 Device parameters plotted as a function of annealing time at 150 ˚C for solar cell with and without TiO_2 nanotube aggregates: (a) Open circuit voltage (V_{oc}), Short circuit current density (J_{sc}); (b) Fill factor (FF) and power conversion efficiency (PCE). (c) Serial resistance (R_{serial}) and shunt resistance (R_{shunt}).

Since there was little difference in the value of V_{oc} and J_{sc}, the enhancement in the PCE of TiO_2 nanotube aggregates solar cell is mainly due to the increase in the FF. It can be seen in Figure 2.5(b) that the FF of TiO_2 nanotube aggregates devices were always higher than the control group. This increase in FF can be traced to the decrease in the serial resistance (R_{serial}) of the active layer (Table 2.1 and Figure 2.5(c)). After adding in TiO_2 nanotube aggregates the R_{serial} values were reduced to half compared to the control group. The shunt resistance (R_{shunt}) decreased as well but to a lesser extent. As the surface roughness of the films plays a minor role in the device efficiency enhancement,[76] this dramatic reduction in serial resistance may be attributed to the TiO_2 nanotube aggregates' ability to improve the charge transportation through the active layer.

Table 2.1 Summary of devices parameters of normal active layer and active layer with 0.002 mol/100 mL TiO_2 nanotube annealed by different time at 150 ˚C

Devices	Anneal Time (min)	V_{oc} (V)	J_{sc} (mA/cm^2)	FF	PCE (%)	R_{shunt} (Ω•cm^2)	R_{serial} (Ω•cm^2)
Control	4	0.66±0.01	7.2±0.5	0.50	2.4±0.2	790	4.7
	5	0.67±0.00	7.0±0.3	0.55	2.7±0.1	790	4.7
	6	0.66±0.00	7.6±0.3	0.52	2.6±0.2	680	4.3
	8	0.67±0.00	7.4±0.3	0.53	2.7±0.1	810	4.5
	9	0.67±0.00	7.4±0.2	0.55	2.7±0.0	830	3.8
	10	0.68±0.01	7.6±0.4	0.51	2.6±0.2	690	5.0
0.002 mol/ 100 mL TiO_2 nanotube	4	0.67±0.00	6.8±0.4	0.56	2.6±0.2	590	3.4
	5	0.67±0.00	7.9±0.2	0.58	3.1±0.1	590	2.4
	6	0.68±0.00	7.4±0.5	0.54	2.7±0.2	560	3.7
	8	0.68±0.00	7.3±0.2	0.56	2.8±0.1	540	3.3
	9	0.68±0.00	7.5±0.3	0.57	2.9±0.1	620	2.8
	10	0.67±0.00	7.3±0.5	0.55	2.7±0.2	600	3.3

In order to investigate the increase in the PCE caused by the TiO_2 aggregates, we decided to study the different steps involved in device performance, namely light absorption, charge dissociation, charge transport and charge collection. It was originally expected that the TiO_2 aggregates may increase the light absorption since a similar effect had previously been observed for dye-sensitized solar cells.[68] By comparing the absorption spectrum (Figure 2.6(a)) of films with and without TiO_2 nanotube aggregates after annealing, it was found that rather than helping absorb more light, the annealed solar cells with TiO_2 nanotubeaggregates absorb less in the range of ~475 nm to ~550 nm, which is the main absorption range of P3HT. Meanwhile, only a slight increase in the spectra appears in the range from ~625 nm to ~675 nm. The drop of absorption in the range of 475 nm~550 nm is assumed to be a result of less P3HT present in the device with TiO_2 nanotube aggregates occupying the space where P3HT would otherwise be. Except for this decrease in the main absorption range of P3HT, the absorption of TiO_2 nanotube aggregate containing devices behave very similarly to the normal P3HT:PCBM devices during thermal treatment: after annealing at 150 ˚C, a redshift of the peak was seen in the absorption spectrum and shoulders at ~575 nm and 600 nm were distinguishable. However, from the values of short current density of devices (Table 2.1 and Figure 2.5(a)), it can be seen that the amount of current produced did not change much before and after adding TiO_2 nanotube aggregates. As TiO_2 nanotube aggregates devices had lower absorbance and exciton separation is almost 100% in P3HT:PCBM solar cell,[77] it was hypothesized that the TiO_2 nanotube aggregates help improve the charge collection or transportation of the active layer and prevent geminate recombination.

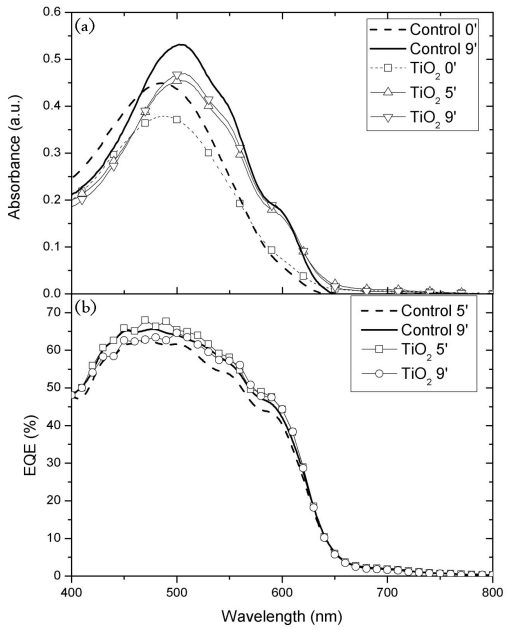

Figure 2.6 (a) Comparison of absorption spectrum between devices with normal active layer and active layer with 0.002 mol/100 mL TiO_2 nanotube. (b) External quantum efficiency (EQE) comparison between solar cell with and without TiO_2 nanotube aggregates annealed at 150 ˚C for different time.

In order to test the hypothesis, further investigations were performed. Figure 2.6(b) shows the external quantum efficiency (EQE) of both P3HT:PCBM only devices and TiO_2 nanotube aggregate containing devices annealed for 5 min and 9 min. For the control group, the 9 min device had a higher EQE than the 5 min device due to the improved morphology obtained by annealing.[76] The EQE of both TiO_2 nanotube aggregate containing devices were very close to the 9 min control sample. Comparing this with their absorbance (Figure 2.6), it confirms that even though the TiO_2 nanotube aggregate containing devices absorb less photons than the control devices, similar amount of charge carriers were collected in both devices. Consequently, the charge carrier collection was improved by adding TiO_2 nanotube aggregates. The charge transportation ability of devices in both types were compared

by measuring the electron only space-charge-limited current (SCLC). The electron mobility of the active layer in each type (Table 2.2) was calculated by applying the method in Ref. 78.[78] It can be seen that by adding the TiO_2 nanotube aggregates the electron mobility of devices increase from 5.1×10^{-5} $cm^2/V\bullet s$ to 7.2×10^{-5} $cm^2/V\bullet s$ for device annealed for 5 min and from 5.71×10^{-5} $cm^2/V\bullet s$ to 6.72×10^{-5} $cm^2/V\bullet s$ for devices annealed for 9 min. This is consistent with device performance and morphology study of TiO_2 nanotube aggregate containing devices annealed for 5 min. We speculate that after annealing for 5 min, the region close to the TiO_2 nanotube aggregates achieved the optimal phase separation (Figure 2.3(d)), which resulted in a larger population of electrons to be created that could be rapidly transported by the TiO_2 nanotube aggregates. At 9 min annealing time, although the rest of the film reached the optimal phase separation (Figure 2.3(g)), morphology in the area adjacent to TiO_2 nanotube aggregates had already further separated (Figure 2.3 (f)). This caused less electrons to be created that were capable of being rapidly transported by the TiO_2 nanotube aggregates.

Table 2.2 Electron mobility of active layer of devices with and without TiO_2 nanotube aggregates. (Derived from electron only SCLC)

	μ_e ($cm^2/V\bullet s$)	
Annealing time	5 min	9 min
Control	5.13×10^{-5}	5.71×10^{-5}
TiO_2	7.22×10^{-5}	6.72×10^{-5}

2.2.2 Conclusions

In conclusion, we have fabricated polymer solar cells based on P3HT:PCBM by adding TiO_2 nanotube aggregates into the active layer. Although the aggregates

decreased the absorbance of device, they also improved the charge transportation and collection inside the active layer. Due to the presence of TiO_2 nanotube aggregates, different morphologies of active layer and optimal annealing condition were observed between the control device and TiO_2 containing devices. The power conversion efficiency of the devices reached as high as 3.2%, which corresponds to a 15% increase in PCE as a result of improved electron transport. We believe that this is a simple method that can be used to improve the efficiency of other polymer solar cells. We are currently investigating how the aggregates size and shape can be changed to further improve the performance of OPVs.

2.2.3 Materials Preparation and Device Setup

Material Preparation: Commercial grade, nanosize TiO_2 (Degussa Aeroxide P25) was a gift from Degussa Corp. (Parsippany, NJ) and used without any purification or treatment. Degussa Aeroxide P25 powder (1.0 g) was added into a 40 mL aqueous solution of 10 M sodium hydroxide. After sonication for 30 min, the resulting suspension was put into a Teflon-lined autoclave and heated to 160 °C for 24 hours. The product was then washed by HCl solutions (0.1 M) followed by centrifugation. This acid washing was repeated three times. After that, the HCl washed samples were washed with ethanol five times to form nanotube structures. Finally the nanotubes were heat treated in air at 500 °C for 2 hours.

Device fabrication: The ITO-coated glass substrates (15 Ω/m^2) were cleaned in an ultrasonic bath with detergent, deionized (DI) water, acetone and isopropyl alchohol. Substrates were then taken out and dried under N_2 flow followed by air plasma

treatment for 15 min. A hole-transport layer of poly(3,4-ethylene-dioxylene thiophene): poly(styrene sulfonic acid) (PEDOT:PSS, Clevios P VP Al 4083) was spin-coated onto the ITO surface from its aqueous solution (40 nm thick). The films were baked at 140 ˚C for 10 min before being transferred into an argon-filled glove-box. The chlorobenzene solution, which contained 25 mg/mL P3HT (Reike Metal, Sepiolid P100) and 15 mg/mL PCBM (American Dye Source Inc. ADS61BFB), was stirred inside the glovebox for at least 3 h at 60 ˚C. The active layer of control devices were achieved by directly spin-coating the P3HT:PCBM solution to form a 140 nm thick layer. For devices with TiO_2 nanotube aggregates, 0.002 mol/100 mL aggregates were added into the solution and sonicated for 30 min to disperse the aggregates first. Then, this solution was kept stirring before it was spin-coated onto the PEDOT:PSS to achieve the same thickness active layer as the control group. Subsequently, all the devices were transferred into a deposition chamber inside the glovebox and 1 nm of LiF and 100 nm of Al were thermally evaporated under a vaccum of 2×10^{-6} Torr. Finally, the devices were completed by annealed at 150 ˚C for varying times.

Device Characterization: The *J-V* characteristics of the solar cells were tested in air using a Keithley 2400 source measurement unit, and an Oriel Xenon lamp (450 W) coupled with an AM1.5 filter was used as the light source. The light intensity was calibrated with a calibrated standard silicon solar cell with a KG5 filter which is traced to the National Renewable Energy Laboratory and a light intensity of 100 $mW\bullet cm^{-2}$ was used in all the measurements in this study. Devices parameters were obtained by taking the average of at least 15 samples for each processing condition. The series resistance and parallel resistance were calculated from the inverse of the

slope of the *J-V* curve at 1 V and 0 V, respectively. External quantum efficiency were measured using an Oriel Cornerstone 130 1/8m Monochromator with the same light source in the *J-V* characteristics. AFM images were taken on a Veeco multi- mode AFM with a nanoscope III controller in tapping mode. The AFM images were taken from actual devices fabricated for measurement of solar performance. Electron-only SCLC devices were fabricated according to the above procedure but the polymers were spin-coated on thermally deposited 100 nm Al instead of PEDOT:PSS.

2.3 Effect of TiO_2 Nanowire (TiO_2-NW)

2.3.1 Literature Review and Introduction

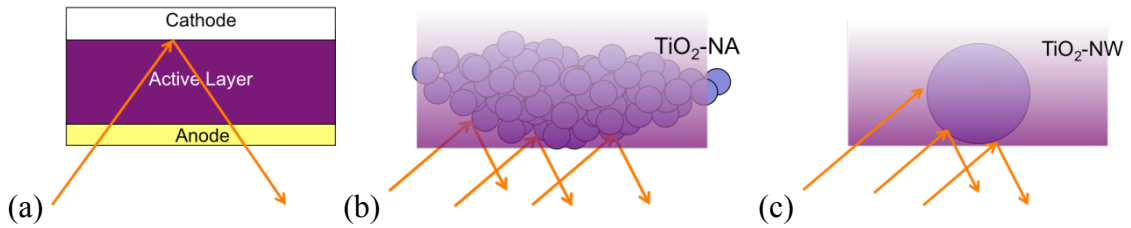

Figure 2.7 Light path illustrations for (a) normal active layer, active layer with (b) TiO_2-NA and (c) TiO_2-NW.

In the previous section, the electron mobility was improved by adding TiO_2 nanotube aggregates (TiO_2-NA) as electron transport pathways into the active layer of P3HT:PCBM organic photovoltaics (OPVs),[79] which led to a 15% increase in the power conversion efficiency (PCE) of our devices. After the TiO_2-NA were incorporated into the P3HT:PCBM active layer, the optimal thermal annealing time was found to be only half of the 10 minute annealing time used by many research groups. However, by adding TiO_2-NA, unfavorable decreases in both active layer absorption and shunt resistance were observed. Herein, we report our further study of this device fabrication methodology by replacing TiO_2-NAs with TiO_2 nanowires (TiO_2-NW) in hope of solving these insufficiencies for TiO_2-NWs' higher conductivity and better size match with the active layer.

The methods to make TiO_2-NW with controlled size and length have been well studied by many research groups in the past.[80–83] TiO_2-NW with around 150 nm in diameter and 1 µm in length were prepared. They are expected to be better than TiO_2-NA in several aspects. First, the TiO_2-NW has better electron conductivity than the TiO_2-NA

because there are fewer grain boundaries and defects inside each wire.[84–86] Also, with smaller diameters, the vertical size matchup between the TiO_2-NW and the thickness of P3HT:PCBM active layer should be better. This should lead to an improved interface between the active layer and top electrode. Finally, by using nanowires instead of larger aggregates, the loss of active layer absorption should be decreased because less light is directly scattered out without passing the active layer (Figure 2.7).

2.3.2 Device Characterization

Except for annealing time, the effect of TiO_2-NWs on P3HT:PCBM solar cell as an electron transport pathways was tested by following the same optimal conditions we found for TiO_2-NAs in the previous study. By varying the thermal annealing time at 150˚C, devices with TiO_2-NWs were also found to optimize at a shorter time (5 min) than 10 min, which is the same as the devices with TiO_2-NAs. Through the *J-V* characterization of these devices (Figure 2.8), although both devices with TiO_2-NWs and TiO_2-NAs significantly showed reduced serial resistant (R_{serial}) and improved performance comparing to the control devices (Table 2.3), the expected improvement by switching TiO_2-NAs to TiO_2-NWs was not observed at this point. In fact, at 6 wt% concentration, the devices with TiO_2-NWs performed slightly worse than the devices with TiO_2-NA (Table 2.3). However, by gradually reducing the amount of TiO_2-NWs added, from 6 wt% to 1 wt%, the performance of devices with TiO_2-NWs increased from 3.7% to 4.1%, which were 0.3% higher than the devices with TiO_2-NAs and 0.5% higher than the control. The reason the devices with TiO_2-NWs were optimized at lower (1 wt%) than the devices with TiO_2-NAs devices (6 wt%) can be attributed to the much smaller

size of TiO_2-NWs. At the same weight percentage, the number of TiO_2-NWs added into the P3HT:PCBM active layer is larger than the number of TiO_2-NAs. The best TiO_2-NWs devices were produced using 1 wt% TiO_2-NWs. Devices with TiO_2-NWs less than 1 wt% (0.5 wt% and 0.33 wt%) were tested as well. Those devices showed very similar performance as the devices with 1 wt% TiO_2-NWs. As a result, the data is not included here.

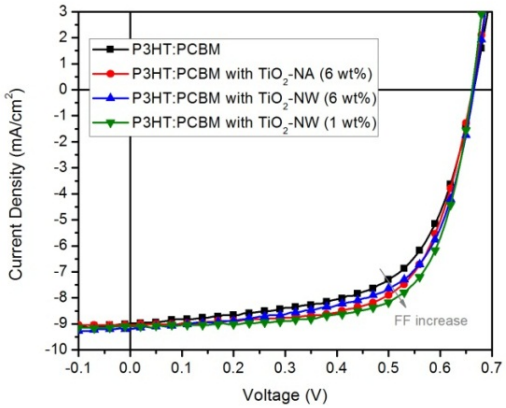

Figure 2.8 *J-V* curves of P3HT:PCBM solar cells with and with TiO_2-NA or TiO_2-NW.

For all devices with TiO_2-NWs, R_{serial} was lower than the control devices. Compared to devices with TiO_2-NAs, R_{serial} of devices with 3 wt% (1.4 Ω cm^2) and 1 wt% (1.4 Ω cm^2) TiO_2-NWs was even further reduced, and it was almost a half of the P3HT:PCBM device (2.3 Ω cm^2). Meanwhile, the shunt resistant (R_{shunt}), which previously decreased by adding TiO_2-NA (600 Ω•cm^2), increased in the case of TiO_2-NWs with all weight percentages. As a larger R_{shunt} is a symbol of lower current leakage in solar cells, the current leakage in the devices with TiO_2-NWs was less than both control devices and devices with TiO_2-NAs. This was in agreement with our assumption that since TiO_2-NWs

had a better vertical size match with the thickness of P3HT:PCBM active layer, and it would have less effect on the electrode and active layer-electrode interface. With a better interface, charge traps are less likely to be created and current leakage is less likely to occur. It was however unexpected that with TiO_2-NWs, the R_{shunt} (1400 Ω cm^2 for 1 wt%) of the devices could be elevated to over twice as much as the value of the control devices (660 Ω cm^2). However, it should also be noted that with increasing amount of TiO_2-NW from 1 wt% to 6 wt%, the R_{shunt} of devices reduced from 1400 to 880 Ω cm^2, while the R_{serial} increased from 1.4 to 1.9 Ω cm^2. This indicated the TiO_2-NWs would still cause some adverse effects on the devices, and at higher adding weight percentages, the adverse effects prevailed the benefits of TiO_2-NWs as electron transport pathways in devices. By reducing the vertical size of the incorporated nanomaterial by replacing TiO_2-NAs with TiO_2-NWs, we were able to reduce their detrimental effects on the active layer-electrode interface. This improvement led to the devices with TiO_2-NWs to perform better than devices with TiO_2-NAs.

Table 2.3 Device parameters of P3HT:PCBM solar cells and P3HT:PCBM solar cells with TiO_2- NAs and TiO_2-NWs.

Device	V_{oc} (V)	J_{sc} (mA cm^{-2})	FF (%)	PCE (%)	R_{shunt} (Ω cm^2)	R_{serial} (Ω cm^2)
P3HT:PCBM[a]	0.664 (±0.001)	9.0±0.1	60±2	3.6±0.1	660	2.3
TiO_2-NA[b] (6 wt%)	0.666 (±0.001)	9.0±0.2	62±2	3.8±0.2	600	1.6
TiO_2-NW[b] (1 µm)	V_{oc} (V)	J_{sc} (mA cm^{-2})	FF (%)	PCE (%)	R_{shunt} (Ω cm^2)	R_{serial} (Ω cm^2)
6 wt%	0.664 (±0.001)	9.0±0.2	62±1	3.7±0.2	880	1.9
3 wt%	0.664 (±0.001)	9.3±0.3	63±2	3.9±0.1	1000	1.4
1 wt %	0.665 (±0.004)	9.3±0.2	66±2	4.1±0.1	1400	1.4

[a] Annealed for 10 mins at 150 ˚C, [b] Annealed for 5 mins at 150˚C

2.3.3 Origin of the Performance Improvement

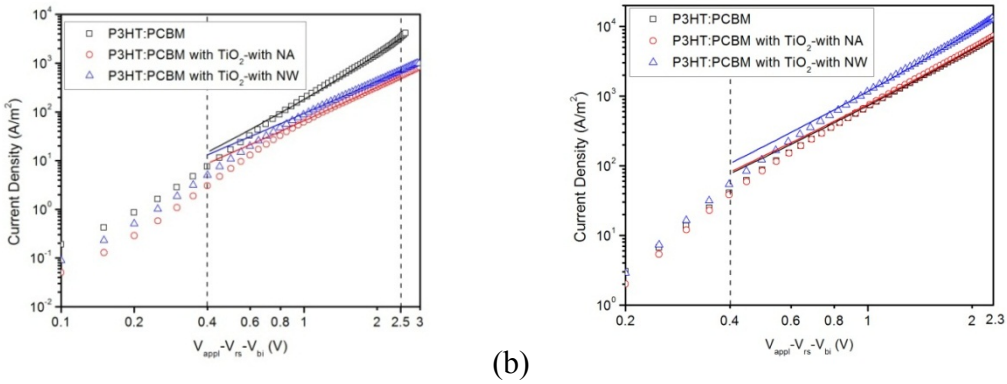

(a) (b)

Figure 2.9 (a) Electron-only and (b) hole-only space charge limited current (SCLC) fitting of P3HT:PCBM solar cells and P3HT:PCBM solar cells with TiO_2-NA and TiO_2-NW (1 μm).

In order to provide greater insight into why the device performance was improved, dark *J-V* characterization was done for the optimized devices with a device configuration designed to conduct only electrons and holes respectively (Figure 2.9). The zero-field electron and hole mobility of active layers in each device were subtracted through space charge limited current (SCLC) fitting and are summarized in Table 2.4. It can be seen that devices with both TiO_2-NAs and TiO_2-NWs had higher electron mobility than the control devices without incorporating any nanostructured materials, which is consistent with the previous findings. The electron mobility of devices with TiO_2-NW had the highest value – 6.1×10^{-9} m^2 V^{-1} s^{-1}, which was about 2.5 times the value of control devices (2.7×10^{-9} m^2 V^{-1} s^{-1}) and 1.5 times the value of devices with TiO_2-NAs (3.7×10^{-9} m^2 V^{-1} s^{-1}). This indicated that the electron transport inside devices with TiO_2-NWs was better than the other two. This is in agreement with the *J-V* curve characterization of devices under AM 1.5; higher electron mobilities were found in devices with better

performance. It also agreed with the fact that there are fewer defects and grain boundaries in TiO_2-NW. Conversely, the hole mobility obtained through the SCLC model showed very little difference between devices; all the fitting values were between 2.1×10^{-8} m^2 V^{-1} s^{-1} and 2.4×10^{-8} m^2 V^{-1} s^{-1}. With similar hole mobilities but obviously different electron mobilities, the hole mobility and electron mobility ratios (μ_h/μ_e) of devices were 7.9, 6.2 and 3.9 for control devices, devices with TiO_2-NAs and devices with TiO_2-NWs respectively (Table 2.4). It has been proven that the balance between electron and hole transport inside the active layer of organic solar cells largely affects their performance, and a more balanced charge transport (mobility ratio between holes and electrons closer to 1) is preferred within the organic solar cell.[87] By adding either TiO_2-NAs or TiO_2-NWs into the P3HT:PCBM active layer as electron transport pathways, the difference between the hole and electron transport was reduced. This helps to explain the trend of improving fill factors that is observed in Figure 2.8.

Table 2.4 Zero-field electron and hole mobility and field activation factors of P3HT:PCBM solar cells without any nanostructured materials and with TiO_2- NAs and TiO_2-NWs as electron transport pathways.

Device	μ_e (m^2 V^{-1} s^{-1})	γ_e ((V m^{-1})$^{-1/2}$)	μ_h (m^2 V^{-1} s^{-1})	γ_h ((V m^{-1})$^{-1/2}$)	μ_h/μ_e
P3HT:PCBM	2.73×10^{-9} (0.06×10^{-9})	7.6×10^{-4}	2.15×10^{-8} (0.02×10^{-8})	4.8×10^{-4}	7.9
TiO_2-NA	3.72×10^{-9} (0.05×10^{-9})	1.4×10^{-4}	2.30×10^{-8} (0.02×10^{-8})	4.6×10^{-4}	6.2
TiO_2-NW	6.08×10^{-9} (0.08×10^{-9})	2.0×10^{-4}	2.42×10^{-8} (0.03×10^{-8})	6.3×10^{-4}	3.9

The values in brackets are errors

2.3.4 TiO_2-NW Length Dependence on Performance Improvement

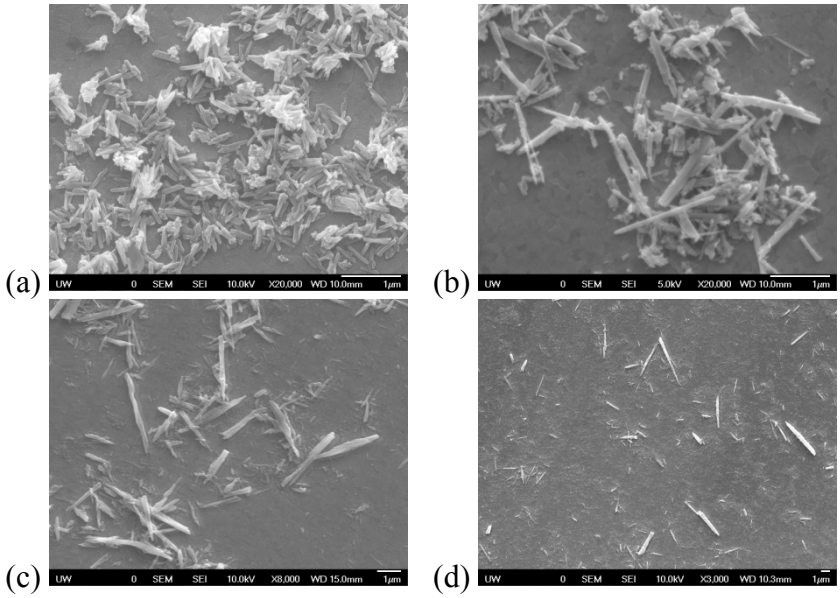

Figure 2.10 SEM image of (a) 500 nm, (b) 1 µm, (c) 3 µm and (d) 7 µm TiO_2-NWs after separation but before being added into the P3HT:PCBM active layer solution.

By replacing TiO_2-NAs with TiO_2-NWs, the vertical size of the incorporated material was reduced. This yielded a positive effect on the performance of final devices. The next logical question would be: will the lateral size of the incorporated nanostructured materials have any impact on the device performance? TiO_2-NWs with similar diameter but four different lengths (500 nm, 1 µm, 3 µm and 7 µm) were prepared by controlling the growth time. After they were separated but before they were added into the active layer solution, scan electron microscope (SEM) images were taken to check their size and separation (Figure 2.10). It was found that after sonication, the length ranges for TiO_2-NWs were: 200 nm~700 nm for '500 nm TiO_2-NWs'; 800nm~3 µm for '1 µm TiO_2-NWs'; 1 µm~4 µm for '3 µm TiO_2-NWs' and 6 µm~8 µm for '7 µm TiO_2-

NWs'.The variations in the length of TiO_2-NWs are likely due to the length deviation from the nanowire growth and breakage during the sonication.

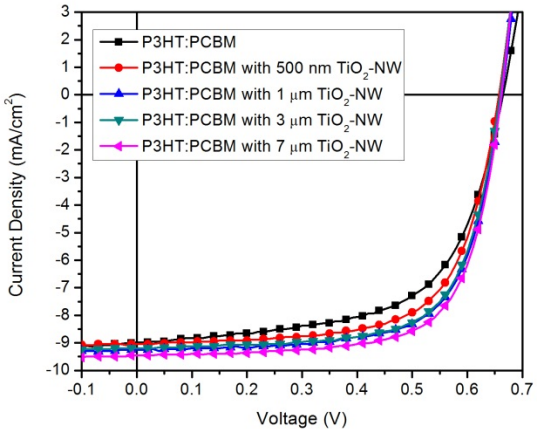

Figure 2.11 *J-V* curve characterization of P3HT:PCBM organic solar cells with 500 nm, 1 μm, 3 μm and 7 μm TiO_2-NWs as electron transport pathways.

All TiO_2-NWs were incorporated into the P3HT:PCBM active layer at a concentration of 1 wt%. Compared to the P3HT:PCBM solar cells without any nanowires, all devices showed improvements in the FF and PCE (Figure 2.11). Additionally, with increasing length of TiO_2-NWs, the R_{shunt} of devices also increased (Table 2.5). This suggests that with longer TiO_2-NWs, more charges are extracted from the active layers at their maximum power. Devices with 500 nm TiO_2-NWs (PCE=4.0%) were the only ones that showed a lower PCE than the devices with 1 μm TiO_2-NWs (PCE=4.1%), due to their lower J_{sc} (Table 2.5). From the SEM image of 500 nm TiO_2-NWs (Figure 2.10 (a)), it can be seen that the separation of 500 nm TiO_2-NWs was not as good as the other three. Several aggregates of TiO_2-NWs were observed in the image. The vertical size of these aggregates was much larger than the actual wires. With these aggregates inside the active

layer, the final devices might suffer from problems similar to the TiO_2-NAs mentioned earlier.

Table 2.5 Device parameters of P3HT:PCBM solar cells with TiO_2-NWs in different length.

TiO_2-NW (1 wt%)	V_{oc} (V)	J_{sc} (mA cm^{-2})	FF (%)	PCE (%)	R_{shunt} (Ω cm^2)	R_{serial} (Ω cm^2)
500 nm	0.657 (±0.002)	9.0±0.1	68±1	4.03±0.04	1400	1.3
1 μm	0.665 (±0.002)	9.3±0.2	66±2	4.1±0.1	1400	1.4
3 μm	0.663 (±0.004)	9.2±0.2	66±2	4.1±0.1	1500	1.3
7 μm	0.660 (±0.003)	9.2±0.3	70±2	4.3±0.1	2200	1.1
Control	0.664 (±0.001)	9.0±0.1	60±2	3.6±0.1	660	2.3

The devices with 3 μm TiO_2-NWs had an almost identical performance compared to the ones with 1 μm nanowires, except its slightly better average R_{shunt} and R_{serial} (Table 2.5). This can be attributed to the close size range of 1 μm TiO_2-NWs (800 nm~3 μm) and 3 μm TiO_2-NWs (1 μm~4 μm) after separation (Figure 2.10 (b), (c)). The best performing devices were achieved by incorporating the longest nanowires into the active layer. The PCE reached 4.4% and the FF reached an impressive value of 70% (Table 2.5). The reasons that devices with 7 μm TiO_2-NWs had the best performance can be attributed to two things. First, it has been reported that with decreased size, the resistant of nanowires will increase due to the increased surface to volume ratio (or interface to volume ratio) that limits both the mobility and availability of free carriers.[88–90] As a result, the 7 μm TiO_2-NWs should have the best electron mobility. Second, for collecting electrons inside

P3HT:PCBM active layer, with longer nanowires, more individual PCBM phases would be connected and larger film area would be benefited with one single nanowire. With further hole-only and electron-only SCLC characterization of films with TiO_2-NWs with each length (Figure 2.12), the films with 7 μm nanowires showed the highest electron mobility value of 9.1×10^{-9} m^2 V^{-1} s^{-1}. Because hole mobilities (around 2.4×10^{-8} m^2 V^{-1} s^{-1}) for all the films remained similar, the free charge transport inside films with 7 μm TiO_2-NWs was the most balanced with an hole:electron mobility ratio of 2.5.

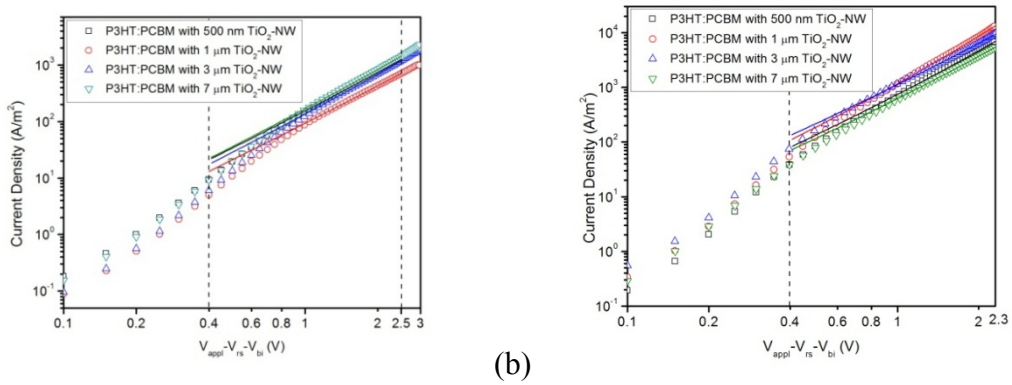

Figure 2.12 (a) Electron-only and (b) hole-only space charge limited current fitting of P3HT:PCBM solar cells TiO_2-NWs of different sizes.

Because incorporating TiO_2-NWs into P3HT:PCBM organic solar cells showed so much promise, a new polymer:PCBM active layer system (PSiF-BT:PCBM) was also tested, to see whether this method would also work for other active layer systems. The molecular structure of PSiF-BT is shown in Figure 2.13. With no further optimization on the incorporating weight percentage and active layer thickness, 7 μm TiO_2-NWs were incorporated into the PSiF-BT:PCBM active layer under the same conditions as for P3HT:PCBM active layer. A shorter annealing time was also preferred after TiO_2-NWs

was added. Again, device performance improvement was observed in devices with TiO_2-NW with V_{oc}=0.86 V, J_{sc}=8.8 mA cm^{-2}, FF=56% and PCE=4.2 % to V_{oc}=0.87 V, J_{sc}=8.8 mA cm^{-2}, FF=60% and PCE=4.6 % (Figure 2.13).

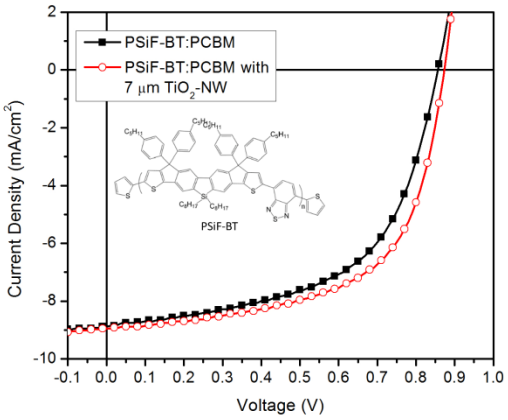

Figure 2.13 *J-V* curve characterization of PSiF-BT:PCBM organic solar cells and PSiF-BT:PCBM organic solar cells with 7 μm TiO_2-NWs as electron transport pathways.

2.3.5 Conclusions

In summary, the incorporation of TiO_2-NAs and TiO_2-NWs were found to improve the performance of OPVs, because they provided improved pathways to transport electrons. Comparing to TiO_2-NAs, TiO_2-NWs showed better abilities as electron transport pathways for its fewer defects and grain boundaries, and better vertical size (diameter) matching with the thickness of the active layer. As a result, devices with TiO_2-NWs showed higher electron mobility, more balanced free charge transport and larger amount of charges extracted at the maximum power. Moreover, the influence of the lateral size (length) of TiO_2-NWs on the performance and charge transport of organic solar cell were studied as well. With increasing length of TiO_2-NWs, the electron mobility and FF of devices increased. For device with 7 μm TiO_2-NWs, the FF reached

an impressive value of 70%. By further incorporating the 7 μm TiO_2-NWs to PSiF-BT:PCBM organic solar cell, similar device behaviors and improvements were also observed, which indicated this method could work for organic solar cells with active layer systems other than P3HT:PCBM. The success of the idea to improve the performance of organic solar cell by incorporating nanostructured materials as electron transport pathways makes it a promising method in future researches and optimization of organic solar cells.

2.3.6 Materials Preparation and Device Setup

Material Preparation: TiO_2 nanowires were grown on fluorine-doped tin oxide (FTO) coated glass (TEC 15, Hartford Glass Co.) by hydrothermal synthesis according to a modified literature procedure.[80] Titanium isopropoxide (0.15 g) was added to 10 mL of a 1:1 mixture of concentrated hydrochloric acid and water. After stirring for several minutes, the clear colorless solution was decanted into a Teflon lined stainless steel autoclave (45 mL, Parr Instrument Co.). Two FTO slides were placed at an angle inside the vessel with the conductive side facing downwards. The nanowires were grown at 150 ˚C for 1.5, 3, 7.5 and 15 hours to achieve 500 nm, 1 μm, 3 μm and 7 μm in length respectively. Then, the TiO_2-NW was scratched off the glass substrate and put in ethanol to sonicate for at least 3 h. After sonication, the ethanol with TiO_2-NW was drop cast on another glass substrate. Scan electron microscope (SEM) images were taken to check the separation of TiO_2-NW. If the TiO_2-NWs were well separated, they were scratched off again and weighed on a balance to get the desired amount.

Device fabrication: The ITO-coated glass substrates (15 Ω m^{-2}) were cleaned in an ultrasonic bath with detergent, deionized (DI) water, acetone and isopropyl alchohol. Substrates were then taken out and dried under N_2 flow followed by air plasma treatment for 15 min. A hole-transport layer of poly(3,4-ethylene-dioxylene thiophene): poly(styrene sulfonic acid) (PEDOT:PSS, Clevios P VP Al 4083) was spin-coated onto the ITO surface from its aqueous solution (40 nm thick). The films were baked at 140 ˚C for 10 min before being transferred into an nitrogen-filled glove-box. The chlorobenzene solution, which contained 25 mg mL^{-1} P3HT (Reike Metal, Sepiolid P100) and 15 mg mL^{-1} PCBM (American Dye Source Inc. ADS61BFB), was stirred inside the glovebox for at least 3 h at 60 ˚C. The active layer of control devices were achieved by directly spin-coating the P3HT:PCBM solution to form a 140 nm thick layer. For devices incorporated with TiO_2-NAs or TiO_2-NWs, the TiO_2-NAs and TiO_2-NWs were added into the solution and taken out of glovebox to sonicate for 30 min. This solution was kept stirring before it was spin-coated onto the PEDOT:PSS to achieve the same thickness active layer as the control group. Subsequently, all the devices were transferred into a deposition chamber inside the glovebox and 100 nm of Al were thermally evaporated under a vacuum of 5×10^{-7} Torr. Finally, the devices were completed by annealing at 150 ˚C for varying times.

Device Characterization: The *J-V* characteristics of the solar cells were tested using a Keithley 2400 source measurement unit, and an Oriel Xenon lamp (450 W) coupled with an AM1.5 filter (which was used as the light source). The light intensity was calibrated with a calibrated standard silicon solar cell with a KG5 filter which is traced to the National Renewable Energy Laboratory. A light intensity of 100 mW cm^{-2} was used in all

of the measurements in this study. Device parameters were obtained by taking the average of at least 20 samples for each processing condition. The series resistance and parallel resistance were calculated from the inverse of the slope of the *J-V* curve at 1 V and 0 V, respectively. The space charge limited current (SCLC) devices were fabricated according to the above procedure but different device configurations. They were ITO/Al (100 nm)/active layer (140 nm)/Al (100 nm) for electron-only SCLC devices and ITO/PEDOT:PSS (40 nm)/active layer (140 nm)/ Pd (50 nm) for hole-only devices. The dark current of the SCLC devices was measured under ambient by using an Agilent 4155B semiconductor parameter analyzer. The mobilities were determined by fitting the dark current to the model of a single carrier SCLC with field dependent mobility, which is described as:

$$J = \frac{9}{8}\varepsilon_0\varepsilon_r\mu_0 exp\left(0.891\gamma\sqrt{\frac{V}{L}}\right)\frac{V^2}{L^3} \quad (1)$$

where J is the current density, μ_0 is the zero-field mobility, γ is the field activation factor, ε_0 is the permittivity of free space, ε_r is the relative permittivity of the material, V is the effective voltage and L is the thickness of the active layer. In simulation, ε_r was assumed to be 3, which is a typical value for organic materials and fullerenes. The effective voltage can be obtained by subtracting the built-in voltage (V_{bi}) and the voltage drop (V_{rs}) from the substrate's series resistance from the applied voltage (V_{appl}), $V=V_{appl}-V_{rs}-V_{bi}$. The thickness of the film (L) was measured by using atomic force microscopy (AFM).

2.4 Identifying and Improving Effects of Inorganic Nanowires as Electron Transport Pathways for Charge Diffusion and Recombination inside Bulk Heterojunction Organic Photovoltaics

2.4.1 Literature review and Introduction

From the discussion in previous sections, it can be seen that using inorganic nanomaterials as electron transport pathways in active layers of bulk-heterojunction OPVs, can effectively improve the charge transport and performance of devices. This method not only utilizes the high conductivity of inorganic nanomaterials, but also diminishes charge loss at the small interface area for exciton dissociation that is often found in polymer/nanomaterial hybrid photovoltaic devices.[91–93] Although research has been performed to study the working principles of inorganic nanomaterials as electron transport pathway in OPVs by SCLC,[79,94] a deeper understanding regarding charge carrier dynamics such as charge separation, diffusion and recombination is still missing. Moreover, a better understanding of the carrier dynamics in OPVs implementing inorganic nanomaterials as electron transport pathways will undoubtedly help future research in this field.

Impedance Spectroscopy (IS) that uses a frequency analysis of the ac behavior of devices is a technique that has been widely applied in a broad class of devices and material systems.[95] It is a very useful tool and has shown good capability to determine carrier dynamics in the operations of different devices such as dye-sensitized solar cells (DSC),[96–99] quantum dot solar cells (QDSCs)[100,101] and solid hole conductors[102,103]. Recently IS has also been applied to investigate OPVs by Bisquert *et. al.*.[95,104,105] With IS

characterization, recombination lifetime, charge transit time and electron diffusion coefficients can be extracted to study the carrier dynamics in OPVs.[106]

In this study, we investigate and compare the carrier dynamics in P3HT:PCBM photovoltaic devices with and without TiO_2-NWs as electron transport pathways by using IS. As surface modification has been reported to be able to reduce back recombination[107–109] and charge traps[110–112] at the TiO_2-NW surface, the effects of surface-modified TiO_2-NW on OPVs will also be examined.

2.4.2 Results and Discussions

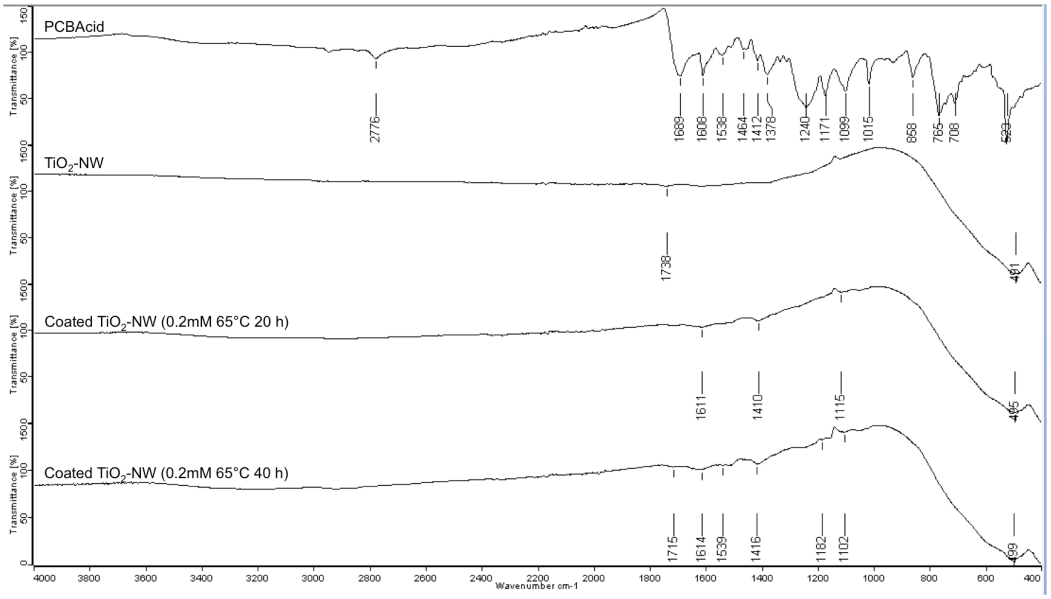

Figure 2.14 FTIR spectrum of PCBAcid, TiO_2-NW and TiO_2-NW after coating

First, TiO_2-NW and C_{60}-substitued benzoic acid (PCBAcid) were synthesized as described in *Material Preparation and Device Setup* section. Then TiO_2-NW (0.3 mg) and C_{60}-substituted benzoic acid (0.3 mg) were added to a tetrahydrofuran (THF):ethanol (1:1) solution (1 mL), which was heated to 60 ˚C and stirred continuously. Next, this

surface-modified TiO_2-NW was centrifuged and cleaned several times to remove any excessive PCBAcid. Fourier transform infrared (FTIR) spectrums (Figure 2.14) were taken to confirm the coating. In the FTIR spectrum of PCBAcid, the double peaks at 708 and 765 cm^{-1} correspond to the C-H bonds, the peaks at 1608 and 1099 cm^{-1} are from C=O and C-O bonds on the side chain, respectively, and the C_{60} in the PCBAcid has two peaks in the FTIR spectrum at 520 and 1378 cm^{-1}.[113,114] Conversely, for the TiO_2-NW, only one broad band from 900 to 450 cm^{-1} with a peak position at 491 cm^{-1} was found. After 20 h coating, a slight shift in peak position from 491 cm^{-1} to 495 cm^{-1} was observed in the TiO_2-NW and two new peaks were found at 1611 and 1410 cm^{-1}. With longer coating (40 h), these peaks were further shifted, and several new peaks appeared at 1102 cm^{-1}. The C_{60} coating causes the shift in the main peak of TiO_2-NW from 491 to 499 cm^{-1}, as well as the new peak at 1416 cm^{-1}. Moreover, the new peaks at 1614 and 1102 cm^{-1} on the coated TiO_2-NW are from C=O and C-O at chain connecting C_{60} and TiO_2-NW. The slight shifting of the peaks from these two bonds indicates formation of new bonds in the adjacent atoms. Therefore, the FTIR spectrum shows that a self-assembled monolayer from C_{60}-substitued benzoic acid was formed on the surface of TiO_2-NW.

The devices used for impedance spectrum characterization have the same structure as the photovoltaic devices (ITO/PEDOT:PSS/Active layer/Al). However, the impedance spectrum (Figure 2.15) was measured with a different illumination technique. In order to force the photovoltaic device to mainly operate under recombination conditions, voltages equal to the open-circuit voltage at each light intensity are applied so that the photocurrent is cancelled by the recombination flow.[106] Under this condition, a major *RC* arc plus additional minor features at high frequency characterize the spectra. At the high

frequency range, information regarding transport and series resistance elements can be extracted, while at the low frequency range, information about recombination in the active layer as well as effective charge life time can be obtained.[95,105,106]

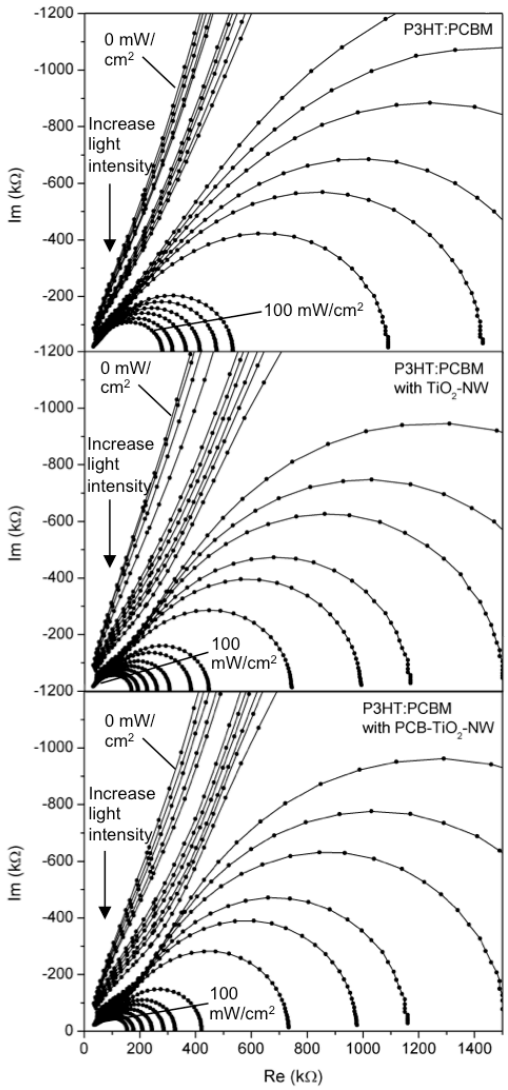

Figure 2.15 Impedance Spectrum of P3HT:PCBM, P3HT:PCBM with TiO_2-NW and P3HT:PCBM with PCB-TiO_2-NW active layers.

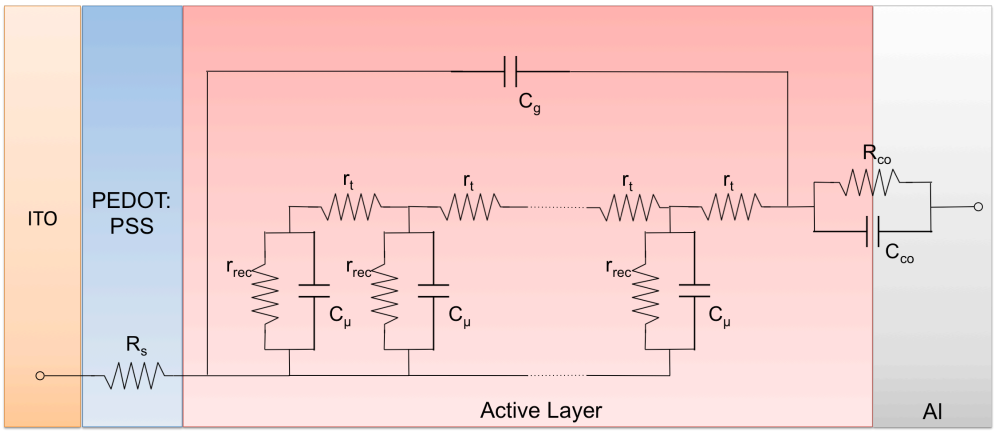

Figure 2.16 Transmission line representation of the equivalent circuit for OPVs. (distributed elements related to carrier transport (r_t), recombination (r_{rec}), chemical capacitance (C_μ); series resistance (R_s), R_{co} C_{co} parallel subcircuit simulates the contact between active layer and top electrode.

In order to obtain quantitative information on carrier dynamics in OPVs, the transmission line model (Figure 2.16) accounting for different impedance response was employed.[104–106] The equivalent circuit in this model (Figure 2.16) consists of: (1) distributed resistors standing for carrier transport, $r_t=R_t/L$, where L is the active layer thickness; (2) distributed chemical capacitance $c_\mu=C_\mu \bullet L$; (3) $r_{rec}=R_{rec}/L$, which accounts for the recombination resistance.[104,105] Furthermore, from these elements, several characteristic parameters related to the carrier dynamics in device can be derived, such as carrier transit time:[104–106]

$$\tau_{diff} = R_t C_\mu \qquad (1)$$

Recombination time (effective lifetime):

$$\tau_{rec} = R_{rec} C_\mu \qquad (2)$$

and diffusion coefficient:

$$D_n = \frac{L^2}{\tau_{diff}} \qquad (3)$$

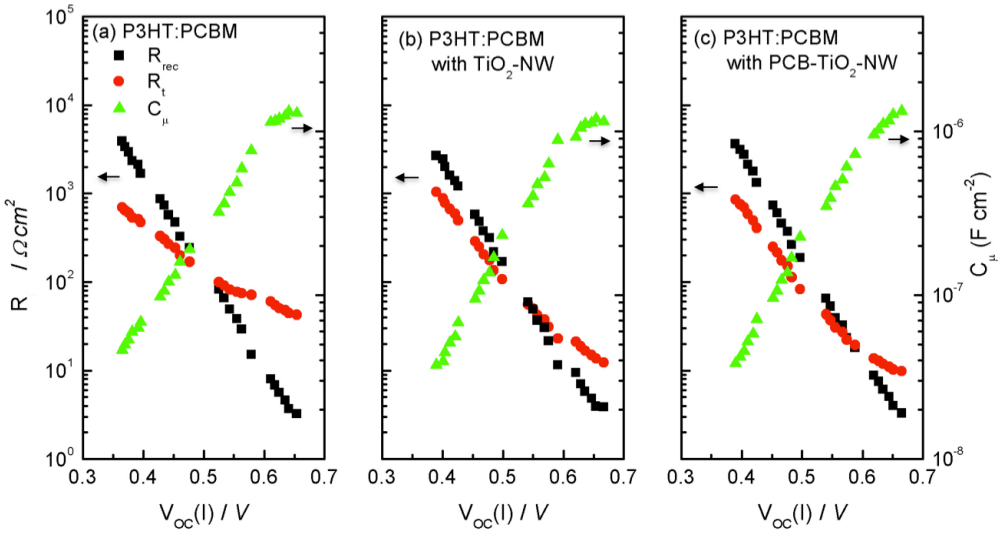

Figure 2.17 R_t, R_{rec} and C_μ extracted from fitting the circuit model to the impedance spectra of (a) P3HT:PCBM, (b) P3HT:PCBM with TiO_2-NWs and (c) P3HT:PCBM with PCB-TiO_2-NWs.

The fitting results of R_t, R_{rec} and C_μ for all three devices (Figure 2.17) shows a typical trend as previously reported in the other studies on OPVs.[106,115,116] The increase of chemical capacitance with V_{oc} follows the shape of a Gaussian distribution, and in the tested V_{oc} range it reflects the shape of the density of states of electrons.[95,106] Both R_t and R_{rec} of all devices decrease with increasing V_{oc} due to the higher charge carrier density from higher illumination. However, devices with TiO_2-NW and PCB-TiO_2-NW show a faster decay in R_t, while R_{rec} are similar in all devices. From the fitting results, the effective lifetime, charge transit time and diffusion coefficient were further calculated by using equations (1), (2) and (3) (Figure 2.18). At higher charge density (>10^{16} cm^{-3}), the effective lifetimes are similar in all three devices, indicating a close recombination rate in devices at high illumination intensity. However, in the lower charge density range (~10^{15} cm^{-3}), the effective lifetime was observed to be the highest in P3HT:PCBM and lowest in the P3HT:PCBM with TiO_2-NW. It is likely reduced by back recombination and surface

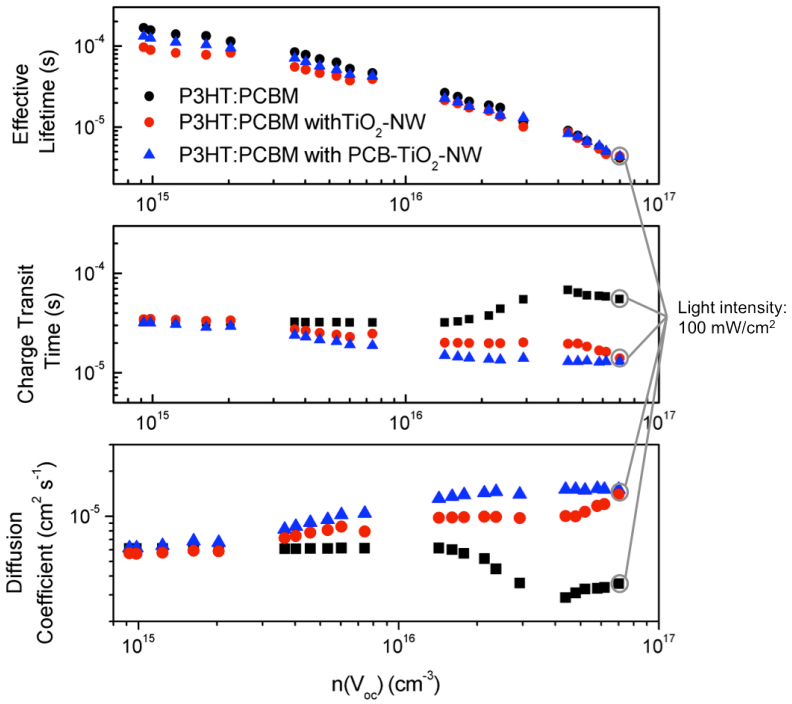

Figure 2.18 Effective lifetime (top), charge transit time (middle) and diffusion coefficient of P3HT:PCBM, P3HT:PCBM with TiO_2-NWs and P3HT:PCBM with PCB-TiO_2-NWs as a function of charge carrier density.

traps on the nanowires. Additionally, the improved effective lifetime in devices with PCB-TiO_2-NW comparing to devices with TiO_2-NW might be due to the effects of surface modification, which was also reported in previous studies on nanowires.[108,109,114] However, more advanced characterization studying recombination with better resolution is needed to confirm this point. Conversely, nearly one order of magnitude improvements were found in both the diffusion coefficient and charge transit time of devices with nanowires. This finding concisely explains the observed mobility increase that results from using nanowires as electron transport pathways in OPVs.[79,94] Additionally, although the charge transit time and diffusion coefficient indicate a similar charge transit and diffusion properties of both devices with TiO_2-NW and PCB-TiO_2-NW, the faster

increase in the diffusion coefficient with PCB-TiO_2-NW when comparing to the device with TiO_2-NW, reveals the interface improvement between the nanowires and organic components from the surface modification of nanowires.

	V_{oc} (V)	J_{sc} (mA/cm^2)	FF	PCE (%)
P3HT:PCBM	0.661 (0.009)	8.5 (0.2)	64% (2%)	3.61 (0.04)
P3HT:PCBM with TiO_2-NW	0.662 (0.005)	8.8 (0.1)	68% (1%)	3.95 (0. 08)
P3HT:PCBM with PCB-TiO_2-NW	0.658 (0.006)	8.8 (0.1)	69% (1%)	3.98 (0.05)

Table 2.6 Device parameters of P3HT:PCBM and P3HT:PCBM with TiO_2-NW or PCB-TiO_2-NW.

Figure 2.19 shows the *J-V* characterization of devices with and without nanowires. The important devices parameters are summarized in Table 2.6. From the characterization, both devices with nanowires show improvement in PCE, and the dominating factor in their efficiency enhancement is the increase in FF by using nanowires as electron transport pathways. Based on the IS analysis on the charge carrier dynamics of devices from above, the increase in FF can be attributed to the improved charge transit and electron diffusion coefficient by using nanowires. Moreover, slightly higher average J_{sc} values were also found in devices with nanowires. In order to elucidate the origin of increased J_{sc}, further IS analyses around short-circuit conditions will be performed; this will tell us carrier dynamics when charge is collected. In comparison to devices with TiO_2-NW, devices with PCB-TiO_2-NW exhibit no further improvement in PCE. This is consistent with their similar effective lifetime, diffusion coefficient and charge transit

time at high carrier density obtained from IS measured at 100 mW/cm^2 light intensity — the same light intensity used in *J-V* characterization (Figures 2.18).

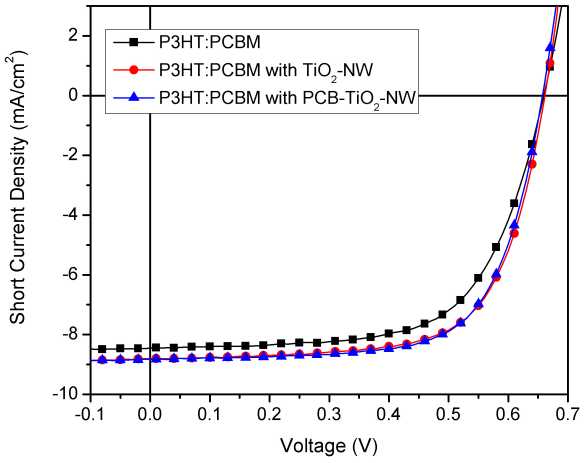

Figure 2.19 *J-V* characterization of P3HT:PCBM and P3HT:PCBM with TiO_2-NW or PCB-TiO_2-NW.

2.4.3 Conclusions

Through applying IS analysis at open-circuit conditions, the carrier dynamics of devices with nanowires as electron transport pathways was studied. Improvements in the charge transit time and electron diffusion coefficient were directly observed in devices with nanowires, which proved the advantageous function of using nanowires as electron transport pathways and is verified the PCE and FF improvement in the photovoltaic devices. In the comparison between devices with nanowires (TiO_2-NW) and surface-modified nanowires (PCB-TiO_2-NW), the faster increase in diffusion coefficient in device with PCB-TiO_2-NW than in devices with TiO_2-NW reflected an improved interface mechanism existing between the nanowires and organic materials in the active layer. More importantly, from the IS analysis and *J-V* characterization of both devices with nanowires, it was found that at high charge carrier density in devices (under 100

mW/cm^2 light intensity), similar diffusion coefficients were similar in devices PCB-TiO_2-NW and devices with TiO_2-NW, indicating the hindrance to charge transit and diffusion from the interface between nanowire and organic material became insignificant. Finally, we also noted that the IS analysis at open-circuit condition was not enough to fully reveal the functions of the nanowires on the operations of OPVs, IS analysis around short-circuit condition will be conducted to provide further information nanowire's function on the charge recombination.

2.4.4 Material Preparation and Device Setup

Material Preparation: TiO_2 nanowires were grown on fluorine-doped tin oxide (FTO) coated glass (TEC 15, Hartford Glass Co.) by hydrothermal synthesis according to a modified literature procedure.[80] Titanium isopropoxide (0.15 g) was added to 10 mL of a 1:1 mixture of concentrated hydrochloric acid and water. After stirring for several minutes, the clear colorless solution was decanted into a Teflon lined stainless steel autoclave (45 mL, Parr Instrument Co.). Two FTO slides were placed at an angle inside the vessel with the conductive side facing downwards. The nanowires were grown at 150 ˚C for 7.5 h to achieve 3 μm in length. Then, the TiO_2-NW was scratched off the glass substrate and put in ethanol to sonicate for at least 3 h. After sonication, the ethanol with TiO_2-NW was drop cast on another glass substrate. Scan electron microscope (SEM) images were taken to check the separation of TiO_2-NW. If the TiO_2-NWs were well separated, they were scratched off again and weighed on a balance to get the desired amount.

C_{60}-substitued benzoic acid used in surface modification of nanowires was synthesized according to Ref. [117]. A mixture of 4-carboxybenzaldehyde, C_{60}, and N-methylglycine were dissolved in chlorobenzene, and the solution was refluxed overnight under a nitrogen atmosphere (Figure 2.20). The solvent was removed by rotary evaporation under reduced pressure. The product was purified by silica gel column chromatography with toluene to toluene–THF (2:1) as the eluents to afford a brown-yellow solid. Then, C_{60}-subsituted benzoic acid was dissolved in THF-ethanol (1:1) at 0.2 mg/mL concentration After the solution was prepared, 0.2 mg/mL TiO_2-NW was added to start coating, and the mixture was kept stirring and heated at 60˚C for 40 h. The coated nanowires were isolated from the solution by centrifuge. At least three cycle of remixing in THF and centrifuge were then applied to wash away excessive C_{60}-substitued benzoic acid in the coated nanowires.

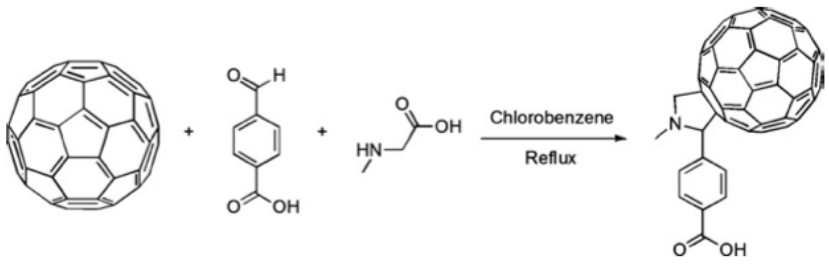

Figure 2.20 Synthesis of C_{60}-substitued benzoic acid

Device fabrication: The ITO-coated glass substrates (15 Ω m^{-2}) were cleaned in an ultrasonic bath with detergent, deionized (DI) water, acetone and isopropyl alchohol. Substrates were then taken out and dried under N_2 flow followed by air plasma treatment for 15 min. A hole-transport layer of poly(3,4-ethylene-dioxylene thiophene): poly(styrene sulfonic acid) (PEDOT:PSS, Clevios P VP Al 4083) was spin-coated onto the ITO surface from its aqueous solution (40 nm thick). The films were baked at 140 ˚C

for 10 min before being transferred into an nitrogen-filled glove-box. The chlorobenzene solution, which contained 25 mg mL^{-1} P3HT (Reike Metal, Sepiolid P100) and 15 mg mL^{-1} PCBM (American Dye Source Inc. ADS61BFB), was stirred inside the glovebox for at least 3 h at 60 ˚C. The active layer of control devices were achieved by directly spin-coating the P3HT:PCBM solution to form a 140 nm thick layer. For devices incorporated with TiO_2-NW, the TiO_2-NW was added into the solution and taken out of glovebox to sonicate for 30 min. And for PCB-TiO_2-NW, because of the better interface, it can easily disperse in solution by just stirring. This solution was kept stirring before it was spin-coated onto the PEDOT:PSS to achieve the same thickness active layer as the control group. Subsequently, all the devices were transferred into a deposition chamber inside the glovebox and 100 nm of Al were thermally evaporated under a vacuum of 5×10^{-7} Torr. Finally, the devices were completed by annealing at 150 ˚C for varying times.

Device Characterization: The *J-V* characteristics of the solar cells were tested using a Keithley 2400 source measurement unit, and an Oriel Xenon lamp (450 W) coupled with an AM1.5 filter (which was used as the light source). The light intensity was calibrated with a calibrated standard silicon solar cell with a KG5 filter which is traced to the National Renewable Energy Laboratory. A light intensity of 100 mW cm^{-2} was used in all of the measurements in this study. Device parameters were obtained by taking the average of at least 20 samples for each processing condition. Impedance spectroscopy IS measurements were performed with Agilent HP 4278A, and was recorded by applying a small voltage perturbation (20 mV rms). Measurements were carried out at different light

intensities and open-circuit voltage condition at each light intensity sweeping frequencies from 1 MHz down to 20 Hz.

3. Structural Impacts of Conjugated Polymers on Active Layers of their Organic Photovoltaic Devices

3.1 Introduction

As mentioned in Section 1.2, developing and synthesizing new conjugated polymers can improve the performance of organic photovoltaics (OPVs). When synthesizing new conjugated polymers for OPV applications, two strategies are often used – (1) lower the bandgap of the polymer so as to harvest more influx photons, which thereby increases the short-circuit current density (J_{sc}); (2) lower the highest occupied molecular orbital (HOMO) of the polymer to enhance the open-circuit voltage (V_{oc}).[118–121] The HOMO and LUMO of the conjugated polymer can be tuned by its donor and acceptor monomers.[122–124] Moreover, the sidechains of conjugated polymers can also affect their energy levels and polarity as well as the crystallinity of the active layer and so on.[125–129] Any of these effects can result a change in device parameters of resultant OPV devices. As a result, understanding the structure-property relationship of conjugated polymers is very helpful in designing new conjugated polymer to improve OPV performance. With this purpose, we studied two different structures in the following sections. In Section 3.2, impacts of silafluorene containing multi-fused heptacylic arenes as the donor monomer in donor-acceptor conjugated polymer were studied. Section 3.3 discusses the influence of fluorine substituents on the conjugated polymer backbone. Both sections describe the characterization and device performance of the aforementioned polymers.

3.2 Low Bandgap Polymers Based on Silafluorene containing Multi-fused Heptacylic Arenes for Photovoltaic Applications

3.2.1 Literature Review and Introduction

To achieve highly efficient OPVs, conjugated polymers with relatively low band gaps, high absorption-coefficients, balanced HOMO and LUMO energy levels, good solubility, and appropriate miscibility with fullerene derivatives in blended active-layers are important prerequisites. Extensive π-conjugation of a rigid polymer backbone will facilitate intermolecular interactions between polymer chains and increase the charge mobility of the polymers.[130,131] Recently, several ladder-type copolymers have been investigated for achieving efficient OPVs.[126,132–134] Specifically, silole-containing semiconducting polymers have been known to exhibit altered properties with respect to their carbon analogues. A variety of functionalized silole-containing semiconducting polymers have been reported to show promising characteristics as materials for PSCs.[124] The introduction of silicon atoms into the polymer backbone has proven to instill several desirable characteristics, such as lower HOMO and LUMO levels, improved molecular packing, and increased charge mobilities.[135–137]

In considering the above, we have designed and synthesized a new variety of low bandgap copolymers that contain a multi-fused thienyl-fluorene-thienyl subunit. Forced planarization by covalently fastening adjacent aromatic units within the polymer backbone helps to strengthen parallel π-orbital interactions to extend the effective conjugation length and facilitate π-electron delocalization, providing an effective way to reduce the band gap. Moreover, coplanar geometries and rigid structures can suppress

rotational disorder around interannular single bonds and lower the reorganization energy, which can in turn enhance intrinsic charge mobilities.[138]

In order to further modulate and optimize the electronic and optical properties, exploration of different electron-deficient units incorporated into multi-fused thienyl-fluorene-thienyl based polymeric backbone is highly desirable. Benzothiadiazole (BT) and thieno[3,4-c]pyrrole-4,6-dione (PD) units are widely used electron-deficient units introduced in the D-A copolymers due to their suitable electron affinity and easy synthesis.[123] In addition, diketopyrrolopyrrole (DPP) has also emerged as a useful acceptor unit because of its planar conjugated bicyclic structure and strong electron-withdrawing nature of polar amide group.[139,120,140] On the basis of the modified multi-fused thienyl-fluorene-thienyl as the core structure, we have successfully synthesized three D-A copolymers, PSiFDCTPD, PSiFDCTBT and PSiFDCTDPP (Scheme 3.1). The synthesis, characterization and photovoltaic applications of these polymers will be discussed.

3.2.2 Results and Discussion

Synthesis and Characterization. The synthetic route of the SiFDCT monomer **5** is depicted in the Scheme 1. Suzuki coupling of 2,7-diboronic ester silafluorene **1** with ethyl 2-bromothiophene-3-carboxylate afforded compound **3**. Double nucleophilic addition of freshly prepared 4-(*n*-pentyl)phenylmagnesium bromide to the ester groups of compound **3** led to formation of tertiary benzylic alcohol compound **4**, which was subjected to intramolecular annulation through Lewis acid-mediated Friedel-Crafts reaction to furnish the fused nonacyclic arene SiFDCT. SiFDCT was brominated in $CHCl_3$ to yield

compound **6** in good yield. Treatment of compound **6** with *t*-butyl lithium followed by quenching with trimethyltin chloride successfully afforded the distannyl compound **7**. Compound **7** was then copolymerized with 1,3-dibromo-5-octylthieno[3,4-c]pyrrole-4,6-dione (PD), 4,7-dibromo-2,1,3-benzothiadiazole (BT), and 3,6-bis(5-bromo-thiophene-2-yl)-2,5-bis[(2-ehtyl)-hexyl]pyrrolo[3,4-c]pyrrole-1,4-dione (DPP), by Stille coupling to give **PSiFDCTPD (**M_n = 16.3 kDa, PDI = 2.1), **PSiFDCTBT (**M_n = 37.4 kDa, PDI = 2.5), and **PSiFDCTDPP (**M_n = 10.4 kDa, PDI = 1.6), respectively. The structures of the polymers were determined by NMR spectroscopy. All polymers showed excellent solubilities in common organic solvents, such as chloroform, toluene and dichlorobenzene.

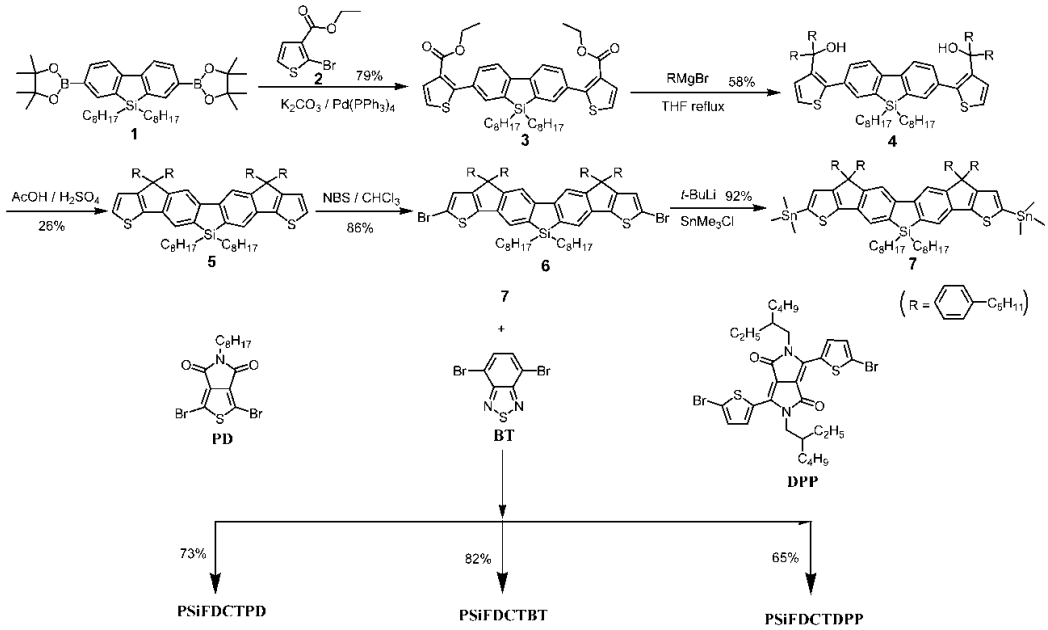

Scheme 3.1 Synthetic route for the SiFDCT monomer and the corresponding copolymers.

Optical Properties. As shown in Figure 3.1a, the absorption spectra of the three polymers in dilute chloroform exhibited two characteristic bands. Each polymer has an absorption band located between 300-550 nm with a second broad absorption from 500-

800 nm. The shorter wavelength absorption can be attributed to the π–π∗ transition of the heptacylic units, while the lower energy band can be attributed to the intramolecular charge transfer (ICT) between the electron-rich and electron-deficient segments.[119] Compared to PSiFDCTPD, which shows absorption maxima at 535 and 562 nm in solution, PSiFDCTBT exhibited a similar absorption maximum at 410 nm with a bathochromic shift of the ICT band to 646 nm. PSiFDCTDPP exhibited an absorption maximum at 430 nm with the ICT band at 714 nm. From Figure 1b, the absorption of all the polymers shifted toward longer wavelengths from solution to the solid state, indicating that the planar structure of SiFDCT is capable of inducing strong interchain interactions. The optical band-gaps (E_g^{opt}) deduced from the absorption edges of the thin film spectra are in the following order: PSiFDCTPD (188 eV) > PSiFDCTBT (1.76 eV) > PSiFDCTDPP (1.57 eV). The difference of their λ_{max} as well as E_g^{opt} indicates that the acceptor strength is in the order DPP > BT> DP.[118] Note that the intensities of the shorter wavelength bands of the polymer in the solid state are apparently stronger than those in the solution state, which suggests that the rigid and coplanar nonacyclic units can enhance their light absorption ability in the solid state.

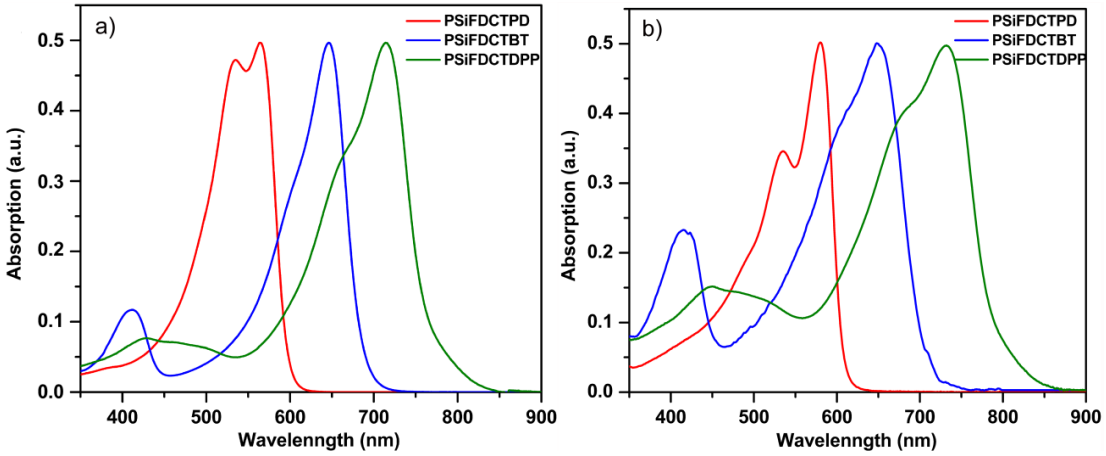

Figure 3.1 Normalized absorption spectra of PSiFDCTPD, PSiFDCTBT, PSiFDCTDPP in chloform (a) and as a thin film (b).

Theoretical Calculations. To further understand the effect of planarization on the molecular structures and properties, we performed theoretical calculations by density functional theory at the level of B3LYP/6-31G(d). Two repeating units SiFDCTPD, SiFDCTBT, and SiFDCTDPP were used as simplified models for simulation of the corresponding three copolymers. Methyl groups were used in the approximation of long alkyl chains in order to reduce calculation time. The optimized structures for PSiFDCTPD, PSiFDCTBT, and PSiFDCTDPP are shown in Figure 3.2. All three polymers show planar conformations through the entirety of the polymer backbone. The dihedral angles between the acceptor moieties and the neighboring SiFDCT fused-ring are ~ $\varphi = 0^{o}$.

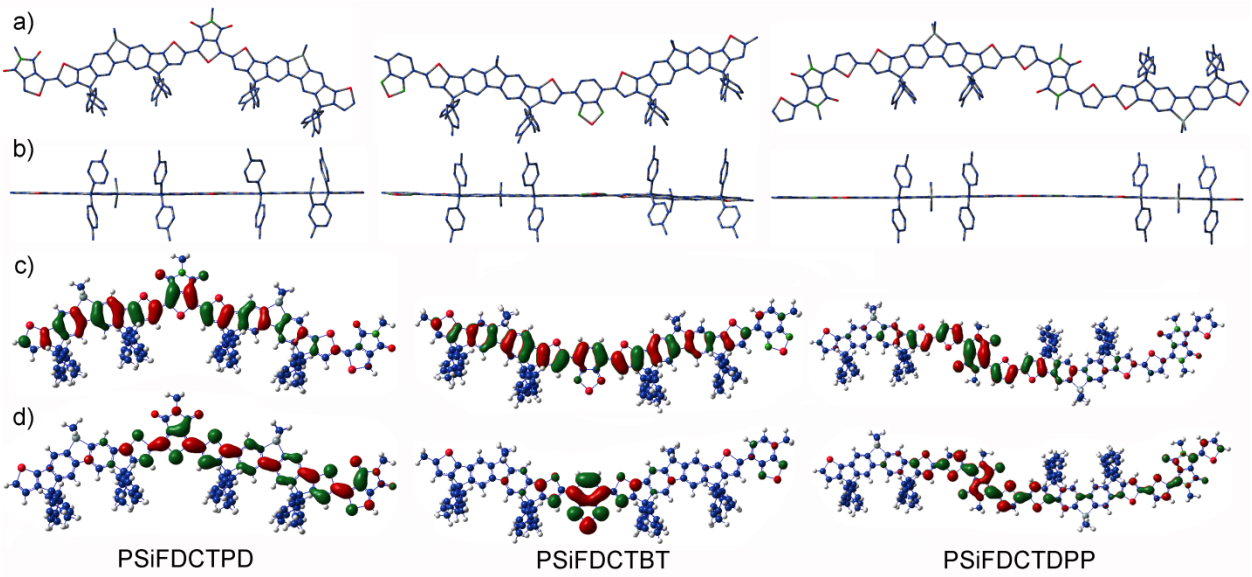

Figure 3.2 Optimized conformations for the structure of PSiFDCTPD, PSiFDCTBT, PSiFDCTDPP top view (a) and side view (b). Wave functions of the HOMO (c) and LUMO (d) orbitals of the corresponding polymers calculated at the level of B3LYP/6-31G (d,p).

The frontier orbitals of the model compounds SiFDCTPD, SiFDCTBT, and SiFDCTDPP are shown in Figure 3.2. The calculated HOMO energy levels of SiFDCTPD, SiFDCTBT, and SiFDCTDPP were -5.54, -5.72, and -5.68 eV, respectively, which are in general agreement with the experimentally determined values for the corresponding polymers (see cyclic voltammetry measurements below) albeit with a shift of 0.2-0.4 eV. For the corresponding alternating dimers, the electron density of the LUMO was primarily located on the electron-accepting unit (Figure 3.2d), whereas the electron density of the HOMO was more evenly distributed across both the donor and acceptor with the exception of PSiFDCTDPP (Figure 3.2c). This redistribution of electron-density shows a pronounced intramolecular charge separation between the donor and acceptor following excitation.

Electrochemical Properties. Cyclic voltammetry (CV) was employed to investigate the electrochemical properties and evaluate the HOMO and LUMO energy levels of the individual polymers. The HOMO and LUMO energy levels were calculated from the onset oxidation potentials (E^{ox}_{onset}) and onset reduction potentials (E^{red}_{onset}) vs Ag/Ag^{+}, respectively, according to Equations (1) and (2).

$$HOMO = -(E_{ox} + 4.75)\ (eV) \qquad \text{Equation (1)}$$

$$LUMO = -(E_{red} + 4.75)\ (eV) \qquad \text{Equation (2)}$$

The electrochemically determined band gaps were deduced from the difference of the onset oxidation and reduction potentials. The energy levels are summarized in Figure 3.3.

All of the polymers showed one stable and reversible p-doping and n-doping processes, which are important prerequisites for p-type semiconductor materials. The

HOMO energy levels were estimated to be -5.31 eV for PSiFDCTPD, -5.32 eV for PSiFDCTBT and -5.26 eV for PSiFDCTDPP, which are in an ideal range to ensure improved air stability and greater attainable V_{oc} in the final device. The LUMO energy levels are approximately located at -3.63 eV for PSiFDCTPD and -3.71 eV for PSiFDCTBT, which are much higher than the LUMO level of the $PC_{61}BM$ acceptor (-4.2 eV) to ensure energetically favorable electron transfer. It should be emphasized that the LUMO level for PSiFDCTDPP is around -3.85 eV from electrochemistry, which is not high enough compared the LUMO level of $PC_{61}BM$ to ensure efficient electron transfer. This can be evidenced by the complete photoluminescence quenching in the film of PSiFDCTPD/$PC_{61}BM$ and PSiFDCTBT/ $PC_{61}BM$, but partly photoluminescence quenching in the film of PSiFDCTDPP/ $PC_{61}BM$.

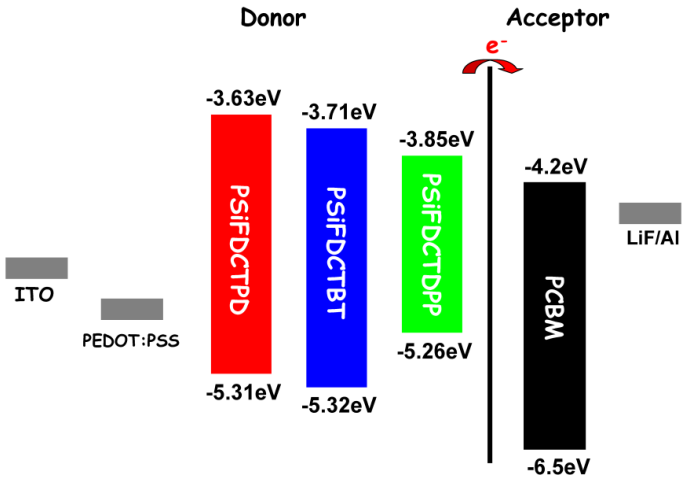

Figure 3.3 Energy level diagrams for PSiFDCTPD, PSiFDCTBT and PSiFDCTDPP.

Photovoltaic and Hole-Mobility Characteristics. BHJ photovoltaic cells were fabricated by spin-coating the blend from DCB solutions at optimized polymer-to-$PC_{61}BM$ (1:3.5) ratios on the basis of the ITO/PEDOT:PSS/Polymer:$PC_{61}BM$/Al configuration with an active layer of approximately 100 nm. Device performances were

measured under a simulated AM 1.5 G illumination of 100 mW/cm^2. Additionally, in order to evaluate the hole and electron mobility in the pure film and active-layer blend by space-charge limited current (SCLC) theory, devices with appropriate configurations were fabricated. The device data are summarized in Table 3.1.

Table 3.1 Photovoltaic and Hole-Mobility Characterization

	mobility (cm^2/(V•s))			V_{oc}	J_{sc}	FF	PCE
	Polymer	Blend		(V)	(mA/cm^2)	(%)	(%)
		hole	electron				
PSiFDCTPD	1.0×10^{-8}	2.5×10^{-6}	1.2×10^{-8}	0.84	7.3±0.1	44±1	2.7±0.1
PSiFDCTBT	1.0×10^{-8}	5.4×10^{-5}	4.8×10^{-8}	0.86	8.8±0.2	56±1	4.2±0.1
PSiFDCTDPP	1.1×10^{-8}	4.6×10^{-7}	3.1×10^{-8}	0.79	3.8±0.02	49±0.3	1.5±0.02

The hole mobilities of all three polymers prior to blending with $PC_{61}BM$ were similar, around 1.0×10^{-8} cm^2/(V•s). However, after blending with $PC_{61}BM$, the hole mobilities of the blended films exhibited an improvement in performance several orders of magnitude higher than the pure films. This is due to the intercalation of $PC_{61}BM$ between the polymer side chains which inhibits coiling of the polymer chains, thereby increasing the conjugation length, improving intermolecular interactions, and improving charge mobilities.[127] This notion is in agreement with an observed red-shift in the absorption spectra of blends films (Figure 3.4b) compared to pure polymer films (Figure 3.4a). The hole mobilities of the blended films followed the trend PSiFDCTDPP:$PC_{61}BM$ (4.6×10^{-7} cm^2/(Vs)) < PSiFDCTPD:$PC_{61}BM$ (2.5×10^{-6} cm^2/(Vs)) < PSiFDCTBT:$PC_{61}BM$ (5.4×10^{-5} cm^2/(Vs)), which might indicate PSiFDCTBT has a better match of side chain free space with $PC_{61}BM$ than PSiFDCTPD and PSiFDCTDPP.[141,142]

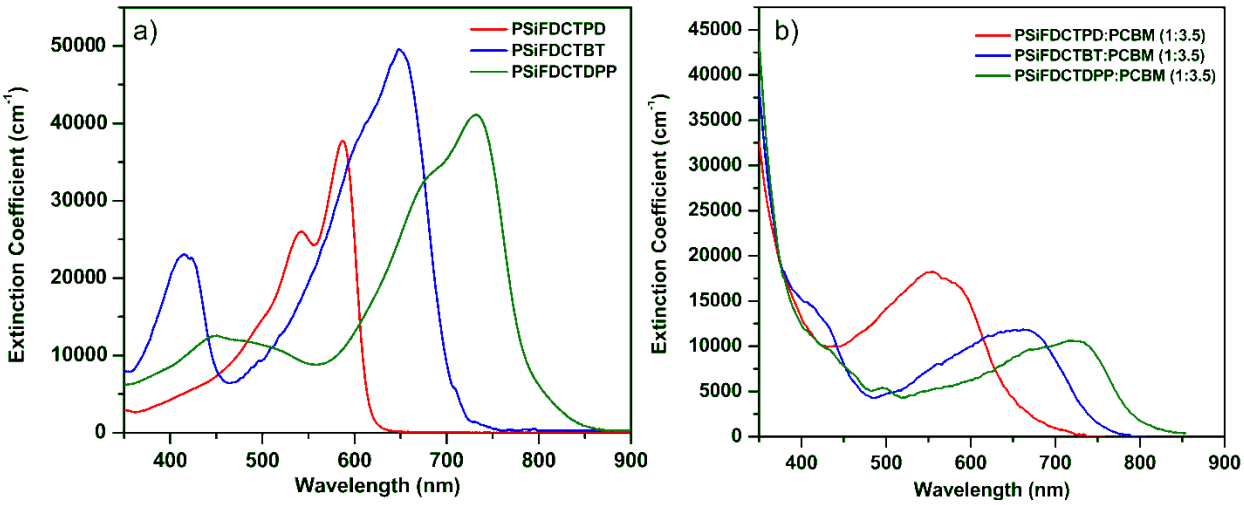

Figure 3.4 (a) Absorption spectra of PSiFDCTPD, PSiFDCTBT and PSiFDCTDPP pure polymer films. (b) Absorption spectra of PSiFDCTPD:$PC_{61}BM$, PSiFDCTBT:$PC_{61}BM$, and PSiFDCTDPP:$PC_{61}BM$ blend films.

The *J-V* and external quantum efficiency characteristics of the devices are shown in Figure 3.5. High V_{oc} values were obtained from all devices. As the V_{oc} can be linearly correlated with the difference between the HOMO level of electron donor (polymers) and the LUMO of electron acceptor ($PC_{61}BM$),[143] the V_{oc} values matched the expected values calculated from the energy levels of polymer materials. However, the 0.35 eV LUMO difference between PSiFDCTDPP and $PC_{61}BM$ is too close to the minimum exciton separation energy (0.3 eV), such that excitons are not efficiently separated in devices using this active layer blend. As mentioned above, this notion can be observed in the PL spectrum of all three polymers. Both PSiFDCTPD:$PC_{61}BM$ and PSiFDCTBT:$PC_{61}BM$ blends exhibited over 90% PL quenching, whereas only 20% PL quenching was observed in blends consisting of PSiFDCTDPP:$PC_{61}BM$. This is the primary justificiation for that devices fabricated using PSiFDCTDPP:$PC_{61}BM$ showing a much lower J_{sc} (3.8 mA/cm^2) and PCE (1.5%) than devices fabricated from the other polymer:$PC_{61}BM$ blends.

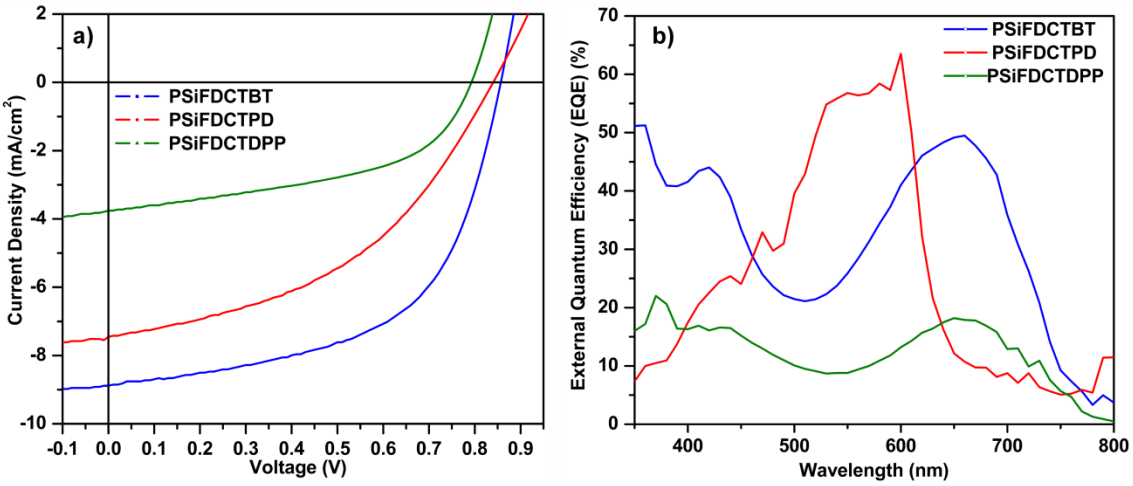

Figure 3.5 (a) *J-V* characteristics of ITO/PEDOT:PSS/polymer:$PC_{61}BM$/Al under illumination of AM 1.5, 100 mW/cm^2. (b) EQE characteristics of the same devices.

The highest performing devices were found from solar cells fabricated from PSiFDCTBT:$PC_{61}BM$ blends, with a PCE of 4.2 % (V_{oc}=0.86 V, J_{sc}=8.8 mA/cm^2, FF=56 %). Devices fabricated from PSiFDCTPD:$PC_{61}BM$ under the same processing conditions only showed a PCE of 2.7 %. From the EQE spectra it can be seen that although PSiFDCTPD:$PC_{61}BM$ achieved the highest maximum value of approximately 65%, PSiFDCTBT:$PC_{61}BM$ showed a broader profile and higher average EQE values. At short wavelengths, the EQEs of PSiFDCTBT:$PC_{61}BM$ blends were about 2 to 3 times higher than the other two active layer blends. This is one reason why PSiFDCTBT:$PC_{61}BM$ devices showed a higher overall PCE than PSiFDCTPD:$PC_{61}BM$ and PSiFDCTDPP:$PC_{61}BM$ devices. Moreover, it has been shown that achieving a balance between the hole and electron mobilities in organic solar cells is one of the key issues in obtaining high-performance devices.[87] The similar electron and hole mobilities in PSiFDCTBT:$PC_{61}BM$ (Table 3.1) may be another reason for their improved device performance.

3.2.3 Conclusions

We have successfully designed and synthesized a ladder-type multi-fused thienyl-fluorene-thienyl unit with rigid and coplanar backbone. The distannyl SiFDCT building block was copolymerized with electron-deficient thieno[3,4-c]pyrrole-4,6-dione (PD), benzothiadiazole (BT) and dithienyldiketopyrrolopyrrole (DPP) units by Stille polymerization to afford three alternating donor-acceptor copolymers, PSiFDCTPD, PSiFDCTBT and PSiFDCTDPP respectively. Through simple and straightforward engineering of molecular structures, the device based on the PSiFDCTBT:$PC_{61}BM$ (1:3.5 in wt%) blend performed a V_{oc} of 0.86 V, a J_{sc} of 8.8 mA/cm^2, a FF of 56%, delivering a PCE of 4.2%. The corresponding PSiFDCTBT:$PC_{61}BM$ blend also showed a high hole mobility of 5.4×10^{-5} cm^2/(V s), leading to a high current density and fill factor.

3.2.4 Materials Preparation and Device Setup

General Measurement and Characterization. All chemicals were purchased from Aldrich or VWR and used as received unless otherwise specified. ^{1}H NMR and ^{13}C NMR spectra were collected on a Brüker Avance DPS-300 spectrometer. Mass Spectrometry was performed using a Hewlett Packard 5971A Gas Chromatograph and Brüker Biflex III MALDI-TOF (both positive and negative ion reflector mode). The molecular weight of polymers was measured using Viscotek TDA 305 with polystyrene standards (room temperature, THF as eluent). The absorption spectra were measured using a Perkins-Elmer Lambda-9 spectrophotometer. Cyclic voltammetry of the polymer films was conducted in acetonitrile with 0.1 M of tetrabutylammonium hexafluorophosphate using

a scan rate of 100 mV s^{-1}. ITO, Ag/AgCl, and Pt mesh were used as the working electrode, reference electrode, and counter electrode respectively.

Fabrication and Characterization of BHJ Devices. ITO/Glass substrates were ultrasonically cleaned sequentially in detergent, water, acetone and isopropyl alcohol. The substrates were covered by a 30 nm layer of PEDOT:PSS by spin coating. After annealing in air at 140 ºC for 10 min, the samples were cooled to room temperature. Polymers were dissolved in *o*-dichlorobenzene (DCB) and $PC_{61}BM$ was added to reach the optimized ratio (1:3.5). The solutions were then heated at 90 ºC and stirred overnight. Prior to deposition, the solutions were filtered through a 0.2 μm filter and the substrates were transfered into a glovebox. The photoactive layer was then spin coated at different speeds to get a thickness about 100 nm. The aluminum cathode (100 nm thick) was thermally evaporated through a shadow mask under high vacuum about 4.0×10^{-7} torr. Devices were then transferred outside the glovebox to test in air using a Keithley 2400 source measurement unit, and an Oriel Xenon lamp (450 W) coupled with an AM1.5 filter was used as the light source. The light intensity was calibrated with a calibrated standard silicon solar cell with a KG5 filter which is traced to the National Renewable Energy Laboratory and a light intensity of 100 $mW\bullet cm^{-2}$ was used in all the measurements in this study. Devices parameters were obtained by taking the average of 15 samples for PSiFDCTBT and 7~8 samples for PSiFDCTPD and PSiFDCTDPP.

Hole-Only Devices. To investigate the hole mobility of polymer films, we chose specific top and bottom contact electrodes in order to measure the charge mobilities within our films (pure film: ITO/PEDOT:PSS/polymer/Al; blends films: electron mobility: ITO/Al/polymer:$PC_{61}BM$/Al, hole mobility: ITO/PEDOT:

PSS/polymer:$PC_{61}BM$/Pd). The hole mobilities were calculated according to space charge limited current theory (SCLC). The *J-V* curves were fitted according to the following equation.

$$J_{e(h)} = \frac{9}{8}\varepsilon_0\varepsilon_r\mu_{e(h)}\exp\left(0.891\gamma_{e(h)}\sqrt{\frac{V}{L}}\right)\frac{V^2}{L^3}$$

Where $J_{e(h)}$ is the electron (hole) current, $\mu_{e(h)}$ the zero-field mobility of the electrons (holes), $\gamma_{e(h)}$ the field activation factor, ε_0 the permittivity of free space, ε_r the relative permittivity of the material, and L the thickness of the active layer. The current was measured by Keithley 2400 source measurement unit. Polymer mobility was gained from the best fitted device.

Synthesis of Compound 3. To a 50 mL two neck flask was introduced compound **1** (2.54 g, 3.86 mmol)**,** ethyl 2-bromothiophene-3-carboxylate (2.35 g, 10 mmol), $Pd(PPh_3)_4$ (230 mg, 0.2 mmol, K_2CO_3 (2.76 g, 20 mmol), and Aliquat 336 (200 mg, 0.5 mmol) in a solution of degassed toluene (30 mL) and degassed H_2O (5 mL). The mixture was heated to 90 ºC under nitrogen overnight. The resulting solution was extracted with ethyl acetate and washed with brine. The combined organic layer was dried over Na_2SO_4. After removal of the solvent under reduced pressure, the residue was purified by column chromatography on silica gel (hexane/ethyl acetate, V/V, 25:1) to give compound **3** as a sticky liquid (2.18 g, 79%). ^{1}H NMR (300 MHz, $CDCl_3$): 7.81 (d, 2H), 7.48 (d, 2H), 7.53-7.46 (m, 4H), 7.22 (d, 2H), 4.21 (m, 4H), 1.98 (m, 4H), 1.21-1.11 (t, 30H), 0.88 (t, 6H). ^{13}C NMR (75 MHz, $CDCl_3$): 158.29, 151.03, 150.86, 140.45, 138.75, 134.62,

130.05, 129.47, 125.21, 124.97, 120.59, 56.32, 42.76, 34.61, 31.77, 30.20, 30.16, 25.36, 23.21, 14.52, 14.26. MS (MALDI-TOF) m/z ($C_{42}H_{54}O_4S_2Si$) calcd for 714.3 found 713.8

Synthesis of Compound 4. To a solution of 4-pentyl-1-bromobenzene (2.73 g, 12 mmol) in anhydrous THF under nitrogen was added *n*-BuLi (4.8 mL, 12 mmol, 2.5 M) dropwise at -78 ºC. The resulting solution was stirred for 1h at this temperature. Then a solution of compound **3** (1.43 g, 2 mmol) in anhydrous THF was added slowly to the above solution. After the addition, the resulting mixture was heated at reflux overnight. The resulting mixture was extracted with ethyl acetate and washed with brine. The combined organic layer was dried over Na_2SO_4. After removal of the solvent under reduced pressure, the residue was purified by column chromatography on silica gel (Chloroform) to give compound **4** as a sticky liquid (1.41 g, 58%). ^{1}H NMR (300 MHz, $CDCl_3$): 7.46 (d, 2H), 7.23 (d, 2H), 7.19 (m, 8H), 7.12 (d, 2H), 7.08 (m, 8H), 7.02 (s, 2H), 6.79 (d, 2H), 3.02 (s, 2H), 1.98-1.67 (m, 4H), 1.57-0.80 (m, 74H). ^{13}C NMR (75 MHz, $CDCl_3$): 154.13, 150.62, 145.23, 139.87, 139.45, 138.21, 132.92, 132.12, 129.85, 128.56, 125.02, 121.78, 120.15, 113.53, 74.32, 36.21, 32.48, 32.14, 30.55, 29.93, 29.51, 28.76, 25.26, 24.77, 24.39, 22.64, 15.36, 12.85. MS (MALDI-TOF) m/z ($C_{82}H_{106}O_2S_2Si$) calcd for 1214.7 found 1213.6

Synthesis of Compound 5. To a solution of compound **4** (2.5 g, 2 mmol) in acetic acid (150 mL) was added conc. H_2SO_4 (3 mL) in one portion. The resulting mixture was refluxed for 4 h and then was extracted with ethyl acetate and washed with brine. The combined organic layer was dried over Na_2SO_4. After removal of the solvent under reduced pressure, the residue was purified by silica gel chromatograph with hexane as the eluent to give a yellow oil product compound **5** (630 mg, 26%). ^{1}H NMR (300 MHz,

$CDCl_3$): 7.51 (s, 2H), 7.38 (s, 2H), 7.21 (d, 2H), 7.14 (m, 8H), 7.09 (m, 8H), 6.88 (d, 2H), 1.96-1.69 (m, 4H), 1.60-0.80 (m, 74H). ^{13}C NMR (75 MHz, $CDCl_3$): 156.34, 155.07, 152.46, 149.53, 142.12, 138.76, 137.23, 134.68, 129.94, 128.04, 125.01, 120.45, 117.39, 114.05, 75.16, 37.01, 33.21, 33.04, 31.39, 30.18, 30.01, 29.34, 25.97, 25.01, 24.84, 22.21, 16.24, 15.72. MS (MALDI-TOF) m/z ($C_{82}H_{102}S_2Si$) calcd for 1178.7 found 1177.1

Synthesis of Compound 6. Compound **5** (500 mg, 0.42 mmol) was dissolved in chloroform (15 mL) a, and then NBS (167 mg, 0.92 mmol) was added into the solution at 0 °C. The resulting mixture was stirred at room temperature for another 2 h. Then the solution was poured onto a sodium carbonate solution (2 M) and extracted with chloroform. The organic phase was dried over anhydrous Na_2SO_4, the solvent was removed under reduced pressure, and the residue was purified by silica gel chromatograph with hexane as the eluent to get compound **6** as a yellow solid (482 mg, 86%). ^1H NMR (300 MHz, $CDCl_3$): 7.53 (s, 2H), 7.39 (s, 2H), 7.19 (m, 8H), 7.12 (m, 8H), 7.06 (s, 2H), 1.94-1.62 (m, 4H), 1.60-0.75 (m, 74H). ^{13}C NMR (75 MHz, $CDCl_3$): 157.25, 155.46, 153.01, 150.11, 144.29, 139.31, 138.07, 134.47, 128.72, 127.96, 124.31, 121.25, 118.26, 114.67, 75.31, 38.53, 34.07, 33.26, 31.35, 31.09, 30.78, 30.01, 26.45, 25.72, 24.68, 22.53, 16.85, 15.31. MS (MALDI-TOF) m/z ($C_{82}H_{100}Br_2S_2Si$) calcd for 1334.5 found 1333.2

Synthesis of Compound 7. Compound **6** (400 mg, 3 mmol) and anhydrous THF were added to a flask under nitrogen atmosphere and cooled to -78 °C. Subsequently, *n*-butyllithium (3 mL, 7.5 mmol, 2.5 M) was added dropwise into the solution. After stirring at -78 °C for 1 h, trimethyltin chloride (7.5 mL, 7.5 mmol, 1 M) was added into the solution in one portion. The resulting solution was stirred at room temperature for

another 1 h. The solution was poured onto water and extracted with diethyl ether twice. The organic phase was dried over anhydrous Na_2SO_4, the solvent was removed under reduced pressure. The residue was washed with cold methanol and then dried under high vacuum overnight to give compound **7** as a white solid (416 mg, 92%). ^{1}H NMR (300 MHz, $CDCl_3$): 7.48 (s, 2H), 7.31 (s, 2H), 7.17 (m, 8H), 7.11 (m, 8H), 6.97 (s, 2H), 1.96-1.60 (m, 4H), 1.50-0.75 (m, 74H), 0.39 (s, 18H). ^{13}C NMR (75 MHz, $CDCl_3$): 155.68, 154.01, 153.64, 149.23, 143.52, 140.16, 138.75, 135.35, 129.13, 128.43, 125.14, 122.35, 119.37, 112.14, 76.23, 42.12, 35.63, 34.28, 32.38, 32.17, 31.59, 30.42, 30.21, 29.58, 28.74, 26.21, 25.84, 25.13, 23.08, 17.13 16.20. MS (MALDI-TOF) m/z ($C_{88}H_{118}S_2SiSn_2$) calcd for 1506.7 found 1507.4

General Synthetic Procedure for PSiFDCTPD, PSiFDCTBT and PSiFDCTDPP by Stille Coupling Reaction: All of the polymers were prepared by a similar procedure. To a Schlenk flask was introduced compound **7** (753.5mg, 0.5 mmol), corresponding acceptor monomer (0.5 mmol), and anhydrous chlorobenzene (4 mL). The solution was flushed with nitrogen for 10 min, and then a catalytic amount of tris(dibenzylideneacetone) dipalladium(0) (8.6 mg, 3 mol%) and tri(*o*-tolyl)phosphine (22.9 mg, 15 mol %) was added into the solution. After the resulting flask was degassed thrice via a freeze-pump-thaw cycle, the reactants were heated up to 100 °C for 48 h. Then, the reaction was cooled to room temperature and added into methanol dropwise. The precipitate was collected by filtration and washed by Soxhlet extraction with methanol, acetone, hexane, and chloroform. The chloroform fraction was then concentrated and precipitated into methanol. The solid was filtered and dried under vacuum for 1 day.

Polymer PSiFDCTPD: Red solid; Yield 73%; ^{1}H NMR (300 MHz, $CDCl_3$): 8.01 (br, 2H), 7.41 (m, 2H), 7.26 (m, 8H), 7.08(m, 8H), 6.74 (m, 2H), 3.09 (br, 4H), 2.87 (br, 2H), 2.08-0.72 (m, 93H). M_n = 16.3K; PDI = 2.1; M_w = 34.2K

Polymer PSiFDCTBT: Red-blue solid; Yield 82%; ^{1}H NMR (300 MHz, $CDCl_3$): 8.08 (br, 2H), 7.75 (br, 2H), 7.52 (m, 2H), 7.19 (m, 8H), 7.10 (m, 8H), 6.87 (m, 2H), 3.14 (br, 4H), 2.03-0.71 (m, 78H). M_n = 37.4K; PDI = 2.5; M_w = 93.5K

Polymer PSiFDCTDPP: Green solid; Yield 65%; ^{1}H NMR (300 MHz, $CDCl_3$): 8.23 (br, 2H), 7.61 (br, 4H), 7.36 (m, 2H), 7.22 (m, 8H), 7.14 (m, 8H), 6.81 (m, 2H), 3.25 (br, 4H), 2.95 (br, 4H), 2.12-0.83 (m, 104H). M_n = 10.4K; PDI = 1.6; M_w = 16.6K

3.3 Influence of Fluorine Substituents on the Film Dielectric Constant and Open-circuit Voltage in Organic Photovoltaics

3.3.1 Literature Review and Introduction

Conjugated polymers with fluorine atoms as substituents on the polymer backbone have drawn great attention recently because they have been shown to greatly enhance the performance of several high performing polymers.[144–148] Since they are strongly electron-withdrawing atoms, fluorine substituents lower the HOMO level of conjugated polymer when they replace hydrogen atoms on the backbone.[149–151] Because the V_{oc} of OPV devices is determined by the energy difference between the HOMO of the electron donor and LUMO of electron acceptor, an enhanced V_{oc} is expected in conjugated polymers with fluorine substituents, which is observed in some active layer systems. This effect has been proposed as the main factor for their performance improvement.[149,151–153] However, in other systems, polymers with fluorine substituents also improve J_{sc} and FF of OPVs when comparing to the non-fluorinated polymer.[148,154,155] This behavior aroused the interest of researchers and led to intensive studies on the underlying principles of fluorine substituents on conjugated polymers.[151,156,157] Recently, besides lowering the HOMO of conjugated polymers, two other functions of fluorine substituents have been reported to play a role in the V_{oc} enhancement of OPVs: (1) reducing bimolecular recombination and (2) increasing the charge dipole moment thereby suppressing geminate recombination.[151,156,157] However, because fluorine substitution shifts the HOMO level of the polymer, to what extent each of the 3 effects plays a role in enhancing V_{oc} remains ambiguous.

In order to isolate each of the effects and to obtain a better understand of the working principle of fluorine substituents on the V_{oc} of OPVs, we synthesized the following three polymers, PBnDT-DPNT (P0F), PBnDT-DPfNT (P1F) and PBnDT-DPffNT (P2F). With careful characterizations of their HOMO levels in three different ways (cyclic voltammetry (CV), photoelectron spectroscopy in air (PESA) and ultraviolet photoelectron spectroscopy (UPS)), we demonstrate that there is neglectable HOMO level difference between P1F and P2F. This allows the isolation of the effects of fluorine substituents on V_{oc} of devices. Further, we show the effect of fluorine substituents on the exciton binding energy, and build a quantitative relationship between the exciton binding energy and V_{oc} change in OPVs.

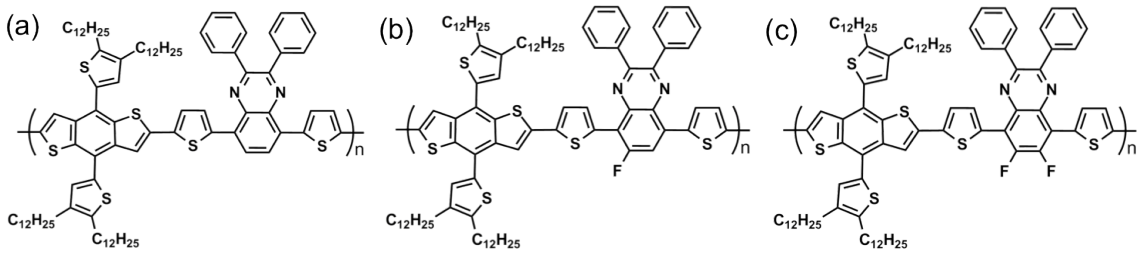

Figure 3.6 Molecular structures of (a) PBnDT-DPNT (P0F), (b) PBnDT-DPfNT (P1F) and (c) PBnDT-DPffNT (P2F).

3.3.2 Result and Discussion

First, these polymers were subjected to simulation software to optimize the structure, and then to quantum mechanical calculations at B3LYP/6-31G level to estimate the HOMO and LUMO energy levels.[158,159] To minimize the computing time, dimers of P0F, P1F and P2F were used during the simulation. The calculated HOMO and LUMO of the optimized structures are summarized in Figure 3.7. The calculated HOMO energy levels

are -4.73 eV, -4.75 eV and -4.75 eV for P0F, P1F and P2F respectively (Table 3.2), which made them potentially good candidates for this research. Following polymer synthesis, the HOMO levels and band gaps of P0F, P1F and P2F films were further characterized by ultraviolet-visible absorption spectroscopy (UV-Vis) (Figure 3.8), CV (Figure 3.9 (a)), PESA (Figure 3.9 (b)) and UPS (Figure 3.9 (c)). In order to make neat polymer films analogous to the OPV active layers, all the films were processed with same solution and concentration used for OPV device fabrication. The characterization results are summarized in Table 3.2.

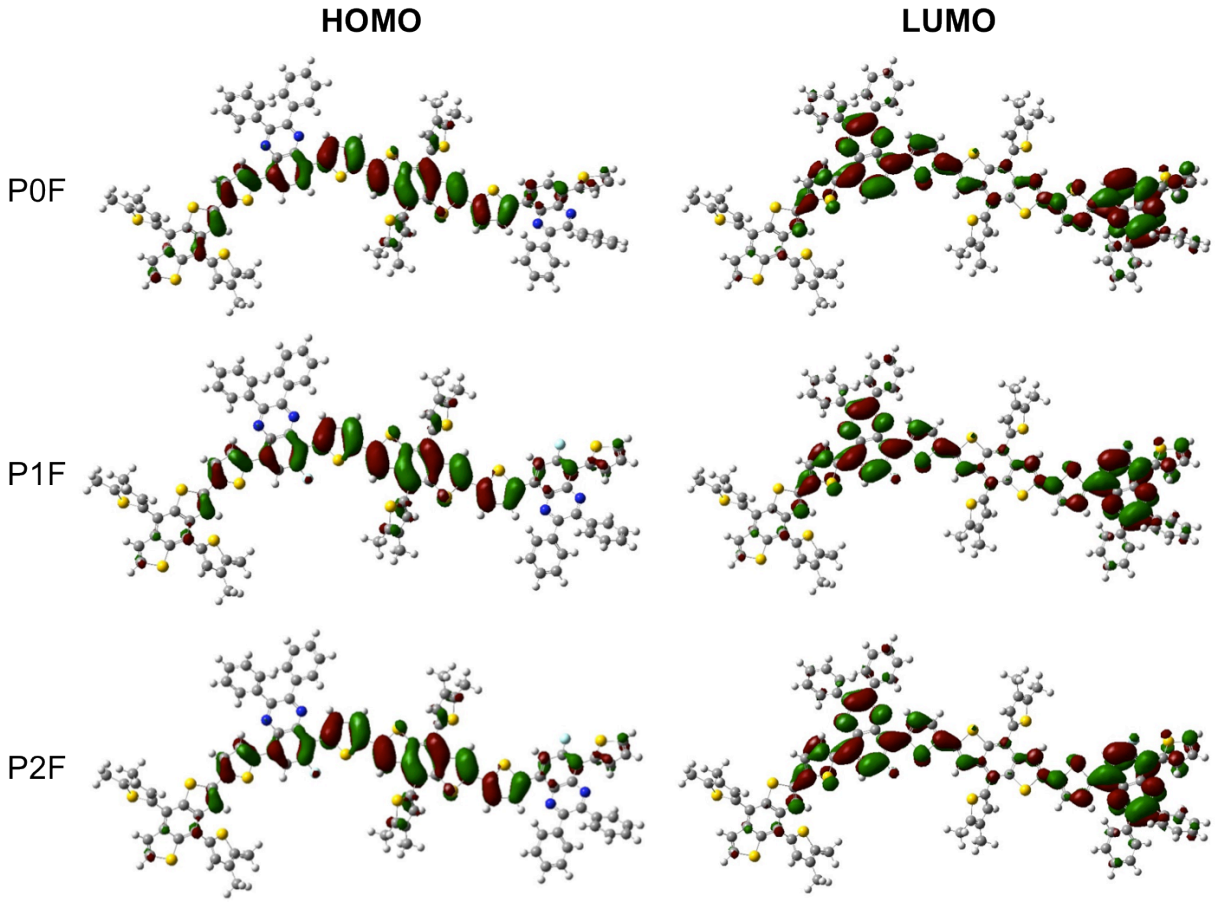

Figure 3.7 Optimized structures and calculated frontier orbitals for P0F, P1F and P2F.

	Gaussian HOMO (eV)	$E_{g\ opt}$ (eV)	CV HOMO (eV)	PESA HOMO (eV)	UPS HOMO (eV)
P0F	-4.73	1.80	-5.08	-5.23	-4.94
P1F	-4.75	1.80	-5.17	-5.30	-5.01
P2F	-4.75	1.81	-5.18	-5.31	-5.05

Table 3.2 Band gap and HOMO levels by different characterization methods of P0F, P1F and P2F.

The UV-Vis of all three polymers in thin film state are shown in Figure 3.8. Each of them shows an absorption band between 400 and 500 nm, and a second band between 500 and 700 nm. The first band can be attributed to the π-π^* transition, while the band with lower energy is due to the intramolecular charge transfer (ICT) between the electron-rich and electron-deficient segments.[158] Moreover, from the absorption edge of the thin films, it can be seen that their optical band gaps (E_g^{opt}) are nearly identical with values around 1.80 eV (Table 3.2). The small differences in the absorption spectra after fluorine substitution were previously reported in PBnDT-FTAZ and PTB4 as well.[160,121] However, it should also be pointed out that in PCPDT-DFBT, the addition of F atoms were found to cause a blue shift in the absorption spectrum.[121]

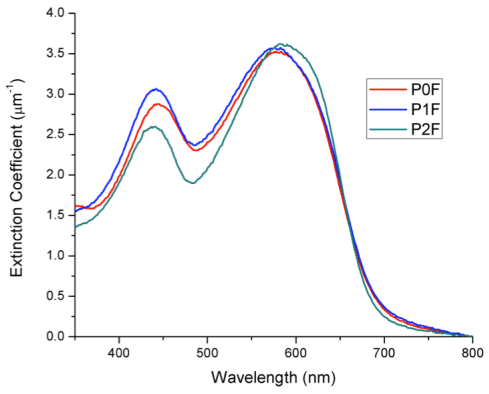

Figure 3.8 UV-Vis spectrum of P0F, P1F and P2F films.

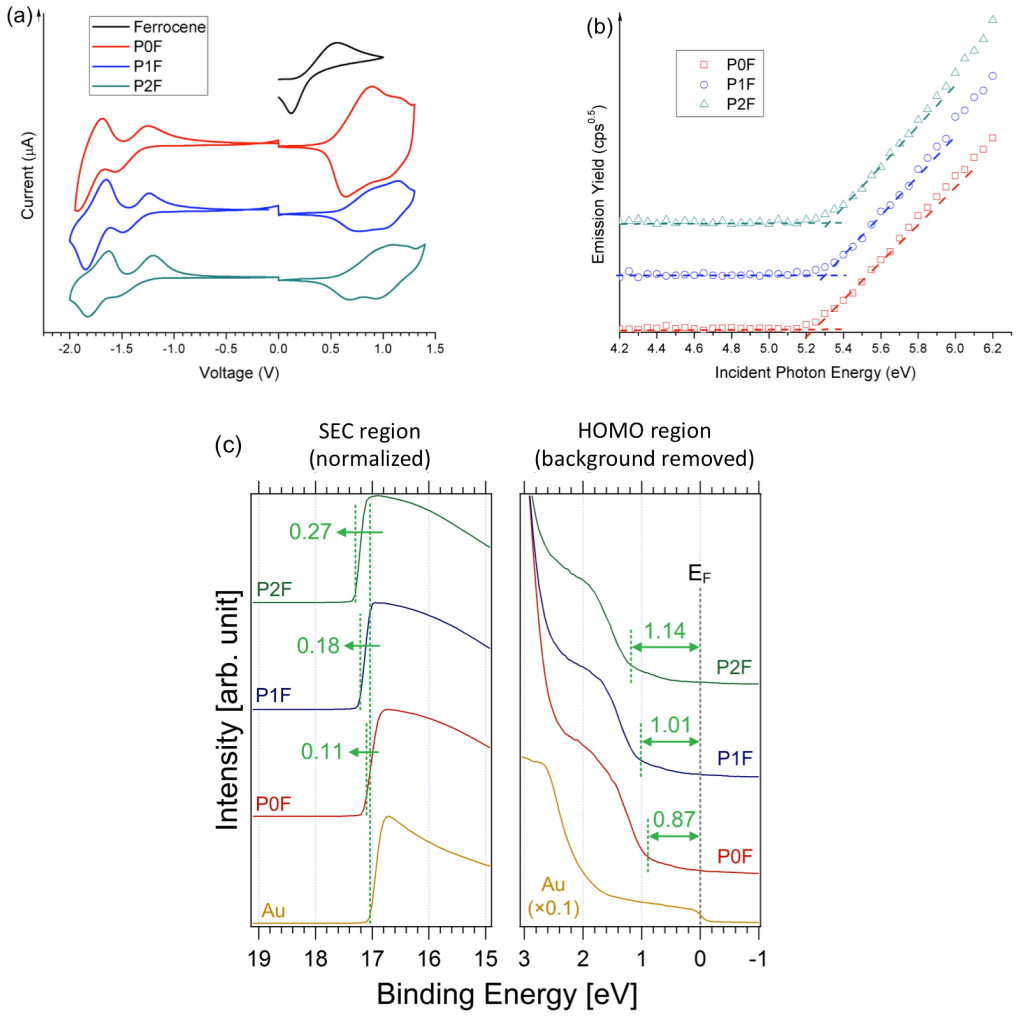

Figure 3.9 (a) Cyclic voltammetry, (b) photoelectron spectroscopy in air and (c) ultraviolet photoelectron spectroscopy of P0F, P1F and P2F films (the dash lines were added to help visualize the curve onsets).

As the V_{oc} of OPVs highly are highly related to the HOMO of electron donors (conjugated polymers) in the active layer,[161,162] it is necessary to know how much the HOMO energy levels are shifted by fluorine substituents before their effect on the V_{oc} of OPV devices can be probed. In order to determine the HOMO energy levels in polymers, cyclic voltammetry (CV) was first employed (Figure 3.9 (a)). The HOMO energy levels were calculated from the onset oxidation potential versus Ag/Ag^+ by the equation HOMO = $-q$ (E_{ox} + 4.57), where q is electric charge and E_{ox} is the onset oxidation potential.

Stable and reversible oxidation behavior was observed for all three polymers, revealing their p-type semiconductor nature. From the CV, the HOMO energy levels of P0F, P1F and P2F are located at -5.08 eV, -5.17 eV and -5.18 eV, respectively (Table 3.2). Although the HOMO differences between P0F and the other polymers are larger than the values from the DFT simulation, the small energy difference (0.01 eV) between the HOMO of P1F and P2F is sufficient to study the other functions of fluorine substituents on V_{oc} while the influence from differing HOMO levels is mostly excluded. To further confirm the HOMO levels, films of all three polymers (prepared identically to the CV films) were characterized by PESA as well (Figure 3.9 (b)). The HOMO levels were estimated to be -5.23 eV for P0F, -5.30 eV for P1F and 5.31 eV for P2F, with the same 0.01 eV difference between P1F and P2F HOMO levels. Finally, the HOMO levels of the three polymers were characterized by UPS (Figure 3.9(c)) and Table 3.2)). Using a gold

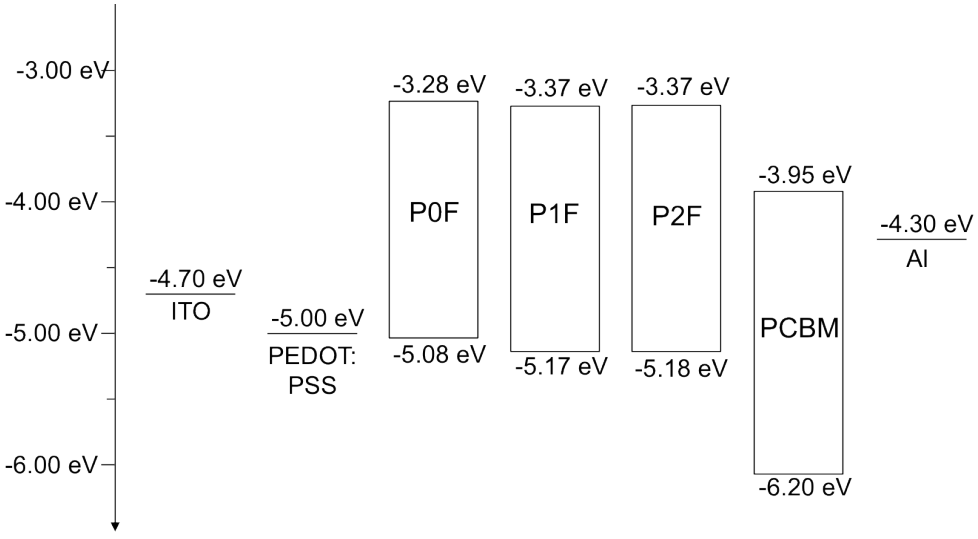

Figure 3.10 Energy level diagrams of P0F, P1F and P2F derived from data of cyclic voltammetry and UV-Vis (LUMO energy levels were calculated from optical band gap and HOMO energy levels in CV).

film as reference, the work function energy shifting (E_Δ) was obtained from the secondary electron cutoff energy onset, while the HOMO energy level position shifting (ΔE_F) was obtained from the cutoff energy onset at the HOMO region. The HOMO energy levels were calculated by HOMO = Ψ_{Au} - ΔE_F + E_Δ, where Ψ_{Au} is the work function of gold layer used as reference and equals -4.18 eV. The calculated HOMO energy levels of P0F, P1F and P2F from UPS are -4.94 eV, -5.01 eV and -5.05 eV, respectively. In Figure 3.10, as the PCBM energy levels obtained from literature[163,164] were characterized by CV, to keep characterization method consistent, the energy levels of all three polymers from CV were used to draw the energy diagram and in the following discussion. Because of the small HOMO level difference between P1F and P2F from CV, if there is a considerable change in V_{oc} of their OPV devices, the impact from fluorine substituents by deepening the HOMO levels will be almost neglectable. The change in V_{oc} should be mainly due to the other influence of fluorine substituents on the V_{oc} of OPVs.

	$HOMO_D$ - $LUMO_A$ (eV)	V_{oc} (V)	J_{sc} (mA/cm^2)	FF	(%)
P0F:PCBM	1.13	0.832 (0.003)	6.37 (0.05)	54% (1%)	2.9 (0.1)
P1F:PCBM	1.22	0.872 (0.003)	6.52 (0.07)	55% (1%)	3.1 (0.1)
P2F:PCBM	1.23	0.914 (0.002)	6.84 (0.03)	59% (1%)	3.7 (0.1)

Table 3.3 Device parameters of photovoltaic devices.

Optimized photovoltaic devices were fabricated by spin-casting polymer and [6,6]-phenyl-C61-butyric acid methyl ester (PCBM) blend solutions (1:3 ratio) in chlorobenzene onto indium tin oxide coated glass (ITO) with a pre-coated PEDOT:PSS

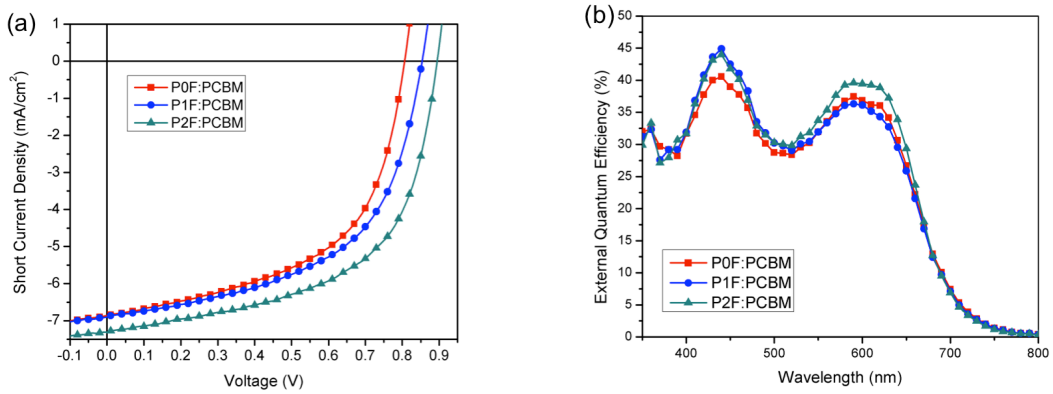

Figure 3.11 (a) *J-V* characteristics of ITO/PEDOT:PSS/polymer:$PC_{61}BM$/Ca/Al under illumination of AM 1.5, 100 mW/cm^2. (b) EQE characteristics of the same devices.

layer. After drying in a nitrogen atmosphere overnight, the active layer thicknesses of photovoltaic devices are about 100 nm. Figure 3.11 (a) shows the *J-V* characteristics of OPV devices for the three polymers. The device parameters are summarized in Table 3.3. All the device parameters similarly increase proportional to the number of fluorine substituents on the polymer backbone. In previously reported systems, the PCE enhancement of polymers with fluorine substituents was mainly due to either an increase in V_{oc}[151–153] or an increase in J_{sc} and FF.[154,155] However, in our case, all three parameters increased with the increasing number of fluorines. The J_{sc} increased from 6.37 mA/cm^2 in P0F to 6.52 mA/cm^2 in P1F and to 6.84 mA/cm^2 in P0F. The UV-Vis (Figure 3.8) and external quantum efficiency (EQE) (Figure 3.11 (b)) spectra provide possible reasons why the improvement in J_{sc} from P0F to P1F and P2F are different. The EQE spectra of

P0F and P1F show almost identical values from 475 nm to 700 nm, with higher values for P1F from 400 to 475 nm. The UV-Vis spectrum of P2F has the lowest absorption from 400 nm to 575 nm and similar value as P0F and P1F in the range between 575 nm to 800 nm. However, its EQE has the highest value in nearly all the wavelength. It indicates the J_{sc} improvement in P2F is mainly due to reasons other than the change in the UV-Vis, which will be discussed in a later section.

On the other hand, the change in V_{oc} from P0F to P2F is more noticeable. The V_{oc} of the photovoltaic devices increased by 0.040 V from P0F to P1F and by 0.042 V from P1F to P2F. It increased about the same amount with each additional fluorine. However, if the V_{oc} is only related to energy difference between the LUMO ($LUMO_A$) of acceptor and the HOMO of donor ($HOMO_D$),[161,162] the 0.042 eV from P1F to P2F cannot be explained because the difference in HOMO levels upon addition of the 2nd fluorine is neglible, leaving the energy difference ($HOMO_D$-$LUMO_A$) the same in both P1F and P2F photovoltaic devices. As a result, both devices should have similar V_{oc}. In order to further reveal the influence of fluorine substituents, a more precise relation between V_{oc} and energy levels of the active layer materials by using the concept of a charge transfer (CT) state is needed:[165–167]

$$V_{oc} = \frac{E_{LUMO}^{A} - E_{HOMO}^{D} - E_{B}^{CTE}}{q} - C \quad (1)$$

where E_{LUMO}^{A} is the LUMO energy level of acceptor, E_{HOMO}^{D} is the HOMO energy level of donor, E_{B}^{CTE} is the binding energy of charge transfer exciton (CTE), q is the elemental electron charge and C is a constant only related to illumination and temperature. It can be

mainly attributed to voltage losses at the interface.[167] The CTEs can be taken as the precursor of free carriers of which the binding energy (E_B^{CTE}) must be overcome to form free carriers. In case of P1F and P2F photovoltaic devices, since $E_{LUMO}^{A} - E_{HOMO}^{D}$ is similar in both devices, the only explanation for the V_{oc} improvement based on this equation is the second fluorine substituent should lower the E_B^{CTE} in device. Moreover, the E_B^{CTE} can be simply estimated by:[168]

$$E_B^{CTE} = \frac{q^2}{4\pi\varepsilon_0\varepsilon_r r} \quad (2)$$

where ε_0 is the vacuum dielectric constant, ε_r is the relative average dielectric constant of active layer and r the radius of average initial CTE after charge transfer.[168]

	Pure (ε_r)	Blend (ε_r)	E_B^{CTE} (eV)	$HOMO_D$-$LUMO_A$ (eV)	V_{oc} (V)
P0F	6.6	4.2	0.231	1.13	0.832
P1F	7.2	4.4	0.219	1.22	0.872
P2F	7.9	5.4	0.178	1.23	0.914
Δ(P0F⇒P1F)	0.6	0.2	0.012	0.09	0.040
Δ(P1F⇒ P2F)	0.7	1	0.039	0.01	0.042

Table 3.4 Relative dielectric constant and calculated E_B^{CTE} of P0F, P1F and P2F pure and blends films.

The relative dielectric constants of P0F, P1F and P2F pure and blends films were calculated from the capacitance of each film on 300 nm SiO_2 layer (Figure 3.12). Then the E_B^{CTE} were derived by using the calculated relative dielectric constants and r=1.5 nm which is common in OPVs.[166,167,169] The E_B^{CTE} values, related energy level difference and

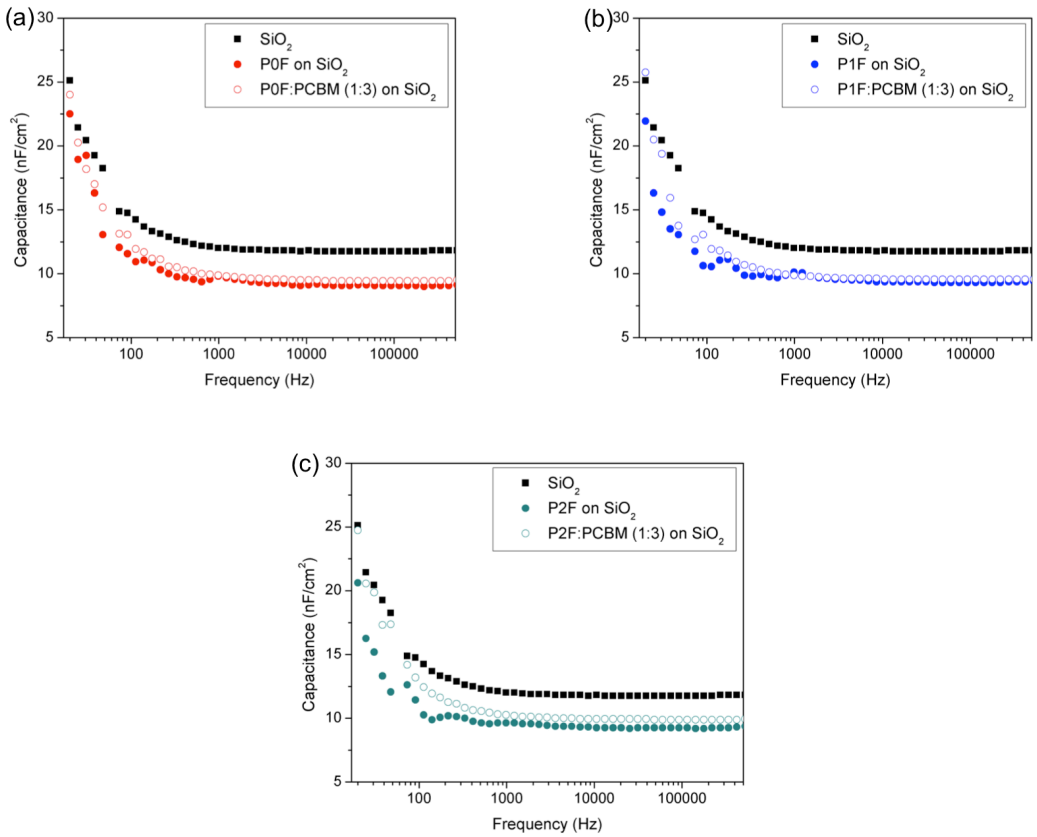

Figure 3.12 Capacitance measurement of P0F, P1F and P2F pure and blends film on 300 nm SiO_2 layer.

V_{oc} of all devices were summarized in Table 3.4. It can be seen that after adding the second fluorine, the relative dielectric constant of the blend film increased by 1 unit compared to a 0.2 increase by adding the first fluorine. As a result, The E_B^{CTE} in P2F:PCBM blend film has the lowest value of 0.178 eV, while in P0F:PCBM and P1F:PCBM, E_B^{CTE} are all over 0.2 eV with values of 0.231 eV and 0.219 eV, respectively. According to the equation (1), as the E_B^{CTE} decreases by 0.039 eV from P1F to P2F, the V_{oc} of their photovoltaic devices should increase by 0.039 V, which is very close to the experimental value (0.042 V) obtained. Moreover, because a lower E_B^{CTE} facilitates free carrier generation independent of incident light wavelength, the lower E_B^{CTE} also explains the high EQE value over all wavelengths in P2F:PCBM photovoltaic devices. From these

results, it can be concluded that the fluorine substituent can also improve V_{oc} OPVs by lowering the charge transfer exciton binding energy.

3.3.3 Conclusions

In summary, three conjugated polymers with 0, 1 and 2 fluorine substituents on the polymer backbone were synthesized. By carefully studying their HOMO and LUMO energy levels, the HOMO levels of P2F and P1F were found to be nearly identical. However, a V_{oc} enhancement was still observed in photovoltaic devices of P1F and P2F, which cannot be explained by the fluorine effect on the polymer HOMO. By further investigating the V_{oc} change with a more precise model involving the charge transfer exciton binding energy, it revealed that beside decreasing the HOMO levels of polymers, fluorine substituents are also able to affect the V_{oc} of OPVs by lower the exciton binding energy in devices.

3.3.4 Materials Preparation and Device Setup

General Measurement and Characterization All chemicals were purchased from Aldrich or VWR and used as received unless otherwise specified. Monomer 1[170], 5,[171] 9[172] and 10[171] were synthesized according to previous literature procedures. ^{1}H NMR and ^{13} C NMR spectra were collected on a Bruker Avance DPS-300 spectrometer. Mass spectrometry wasperformed using a Hewlett-Packard 5971A gas chromatograph and Bruker Bi flex III MALDI−TOF (both positive and negative ion reflector mode). The molecular weight of the polymers was measured using Viscotek TDA 305 with polystyrene standards (room temperature, THF as eluent). The absorption spectra were measured using a Perkins-Elmer Lambda-9 spectrophotometer.

Synthetic Section:

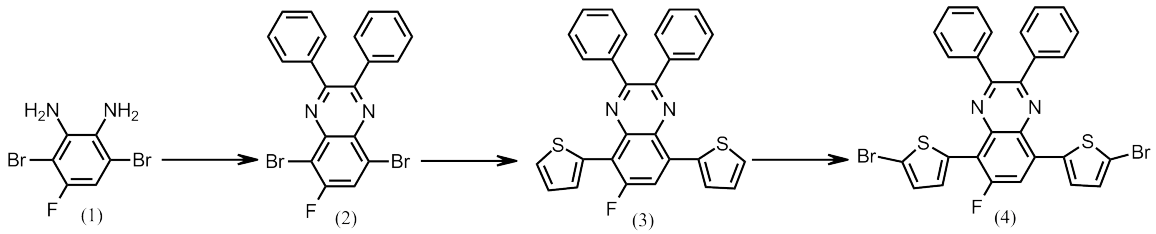

Scheme 3.2 Synthetic route for Monomer 4

5,8-dibromo-6-fluoro-2,3-diphenylquinoxaline (2):

The mixture of 2,5-dibromo-4-fluoro-5,6-benzenediamine (0.85 g, 3.0 mmol) and benzil (0.63 g, 3 mmol) in 30 mL of acetic acid was refluxed overnight. After cooling to room temperature, the solution was poured into water and extracted with dichloromethane. After removing solvent, the crude product was purified by column chromatography and followed by re-crystallization to give a light yellow solid (1.1 g, 83%). ^{1}H NMR ($CDCl_3$, ppm): 7.94 (s, 1H), 7.70-7.66 (m, 4H), 7.44-7.35 (m, 6H). ^{13}C NMR ($CDCl_3$, ppm): 158.72, 141.37, 140.25, 136.70, 133.25, 130.67, 129.43, 127.54. HRMS (ESI): ($[M^+H]^+$, $C_{20}H_{11}Br_2FN_2$), cacld, 455.9; found: 460.9

6-Fluoro-2,3-diphenyl-5,8-di(thiophene-2-yl)quinoxaline (3)

To a 50 mL two-neck flask was introduced compound **2** (0.9 g, 2 mmol), *2*-(Tributylstannyl)thiophene (1.87 g, 5 mmol), $Pd(PPh_3)_4$ (46 mg, 0.04mmol) in a solution of degassed toluene (30 mL). The mixture was heated to 90°C under nitrogen overnight. The resulting solution was extracted with ethyl acetate and washed with brine. The combined organic layer was dried over Na_2SO_4. After removal of the solvent under reduced pressure, the residue was purified by column chromatography on silica gel (hexane/DCM, v/v, 5:1) to give compound **3** as an orange crystals (659 mg, 71%). ^{1}H NMR ($CDCl_3$, ppm): 7.61 (s, 1H), 7.63-7.57 (m, 6H), 7.46-7.32 (m, 6H). 7.15 (m, 2H),

7.02 (d, 2h). ^{13}C NMR ($CDCl_3$, ppm): 163.21, 160.23, 154.17, 145.27, 142.35, 133.23, 130.06, 129.09, 127.98, 125.31. MALDI-TOF: ($C_{28}H_{17}FN_2S_2$), cacld, 464.1; found: 463.0

5,8-Bis(5-bromothiophen-2-yl)-6-fluoro-2,3-diphenylquinoxaline (4)

Compound **3** (464 mg, 1 mmol) was dissolved in chloroform (15 mL), and then NBS (360 mg, 2mmol) was added into the solution at 0°C. The resulting mixture was stirred at room temperature for another 2 h. Then the solution was poured onto a sodium carbonate solution (2 M) and extracted with chloroform. The organic phase was dried over anhydrous Na_2SO_4, the solvent was removed under reduced pressure, and the residue was purified by silica gel chromatograph with hexane as the eluent to get compound 6 as an orange solid (528 mg, 81%). 1H NMR ($CDCl_3$, ppm): 7.70 (s, 1H), 7.68-7.69 (m, 6H), 7.47-7.31 (m, 4H). 7.07 (m, 2H), 6.93 (d, 2h). ^{13}C NMR ($CDCl_3$, ppm): 165.72, 163.31, 156.07, 148.90, 144.6, 137.43, 136.27, 133.51, 128.12, 125.03. MALDI-TOF: ($C_{28}H_{15}Br_2FN_2S_2$), cacld, 619.9; found: 619.0

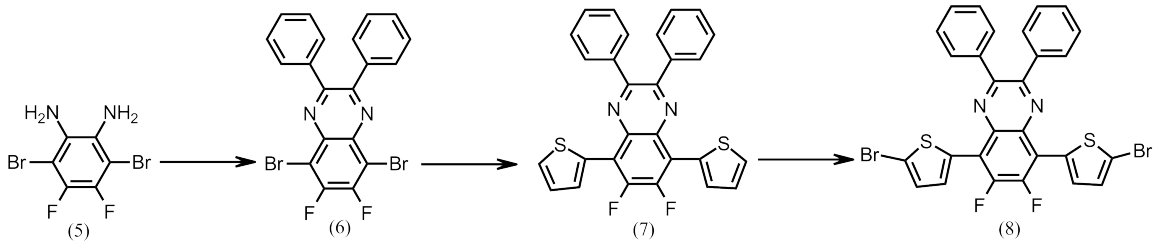

Scheme 3.3 Synthetic route for Monomer (8)

5,8-dibromo-6,7-difluoro-2,3-diphenylquinoxaline (6):

The mixture of 2,5-dibromo-3,4-difluoro-5,6-benzenediamine (0.6 g, 2.0 mmol) and benzil (0.42 g, 2 mmol) in 20 mL of acetic acid was refluxed overnight. After cooling to room temperature, the solution was poured into water and extracted with dichloromethane. After removing solvent, the crude product was purified by column chromatography and followed by re-crystallization to give a light yellow solid (0.74 g,

77%). ^{1}H NMR ($CDCl_3$, ppm): 7.70-7.66 (m, 4H), 7.44-7.35 (m, 6H). ^{13}C NMR ($CDCl_3$, ppm): 152.34, 144.37, 141.87, 139.15, 136.76, 135.47, 130.28, 125.73. MALDI-TOF: ($C_{28}H_{17}FN_2S_2$), cacld, 473.9; found: 472.6

6,7-Difluoro-2,3-diphenyl-5,8-di(thiophene-2-yl)quinoxaline (7)

To a 50 mL two-neck flask was introduced compound **6** (0.95 g, 2 mmol), *2*-(Tributylstannyl)thiophene (1.87 g, 5 mmol), $Pd(PPh_3)_4$ (46 mg, 0.04mmol) in a solution of degassed toluene (30 mL). The mixture was heated to 90°C under nitrogen overnight. The resulting solution was extracted with ethyl acetate and washed with brine. The combined organic layer was dried over Na_2SO_4. After removal of the solvent under reduced pressure, the residue was purified by column chromatography on silica gel (hexane/DCM, v/v, 5:1) to give compound **3** as an red crystals (659 mg, 71%). ^{1}H NMR ($CDCl_3$, ppm): 7.66-7.61 (m, 6H), 7.42-7.33 (m, 6H). 7.21 (m, 2H), 7.13 (d, 2h). ^{13}C NMR ($CDCl_3$, ppm): 166.67, 163.42, 158.03, 146.74, 144.11, 135.47, 132.52, 130.13, 125.02, 121.63. MALDI-TOF: ($C_{28}H_{17}FN_2S_2$), cacld, 482.1; found: 481.0

5,8-Bis(5-bromothiophen-2-yl)-6-fluoro-2,3-diphenylquinoxaline (8)

Compound **7** (482 mg, 1 mmol) was dissolved in chloroform (15 mL), and then NBS (360 mg, 2mmol) was added into the solution at 0°C. The resulting mixture was stirred at room temperature for another 2 h. Then the solution was poured onto a sodium carbonate solution (2 M) and extracted with chloroform. The organic phase was dried over anhydrous Na_2SO_4, the solvent was removed under reduced pressure, and the residue was purified by silica gel chromatograph with hexane as the eluent to get compound **8** as a red solid (427 mg, 67%). ^{1}H NMR ($CDCl_3$, ppm): 7.73-7.70 (m, 6H), 7.51-7.43 (m, 4H). 7.17 (m, 2H), 7.06 (d, 2h). ^{13}C NMR ($CDCl_3$, ppm): 162.07, 167.13, 154.76, 150.11, 141.37,

136.12, 135.97, 131.27, 127.83, 123.21. MALDI-TOF: ($C_{28}H_{17}FN_2S_2$), cacld, 637.9; found: 636.6

General procedure for the Polymerization:

All of the polymers were prepared by a similar procedure. To a Schlenk flask was introduced compound 7 (753.5 mg, 0.5 mmol), corresponding acceptor monomer (0.5 mmol), and anhydrous chlorobenzene (4mL). The solution was flushed with nitrogen for 10 min, and then a catalytic amount of tris(dibenzylideneacetone) dipalladium(0) (8.6mg, 3 mol %) and tri(o-tolyl)phosphine (22.9 mg, 15 mol %) was added into the solution. After the resulting flask was degassed thrice via a freeze−pump−thaw cycle, the reactants were heated up to 100°C for 48 h. Then, the reaction was cooled to room temperature and added into methanol dropwise. The precipitate was collected by filtration and washed by Soxhlet extraction with methanol, acetone, hexane, and chloroform. The chloroform fraction was then concentrated and precipitated into methanol. The solid was filtered and dried under vacuum for 1 day.

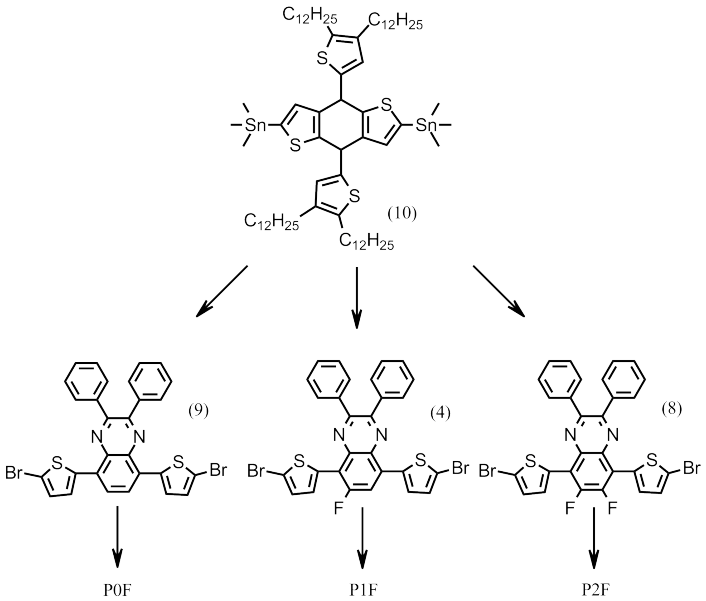

Scheme 3.4 Synthetic route for P0F, P1F and P2F.

Polymer PBDT-DTQU (P0F): Red Solid. ^{1}H NMR ($CDCl_3$, ppm): 8.27 (br, 2H), 8.13 (br, 1H), 7.59 (m, 2H), 7.13 (m, 8H), 7.12 (m, 8H), 2.36 (br, 8H), 1.58 (m, 8H), 1.45 (m, 24H), 0.80 (m, 12H). Molecular weight: M= 32.9 k, PDI = 2.70.

Polymer PBDT-DTFQU (P1F): Red Solid. ^{1}H NMR ($CDCl_3$, ppm): 8.25 (br, 2H), 8.04 (br, 1H), 7.57 (m, 2H), 7.26 (m, 8H), 7.12 (m, 8H), 2.59 (br, 8H), 1.58 (m, 8H), 1.35 (m, 24H), 0.89 (m, 12H). Molecular weight: Mn= 27.9 k, PDI = 3.20.

Polymer PBDT-DTDFQU (P2F): Red Solid. ^{1}H NMR ($CDCl_3$, ppm): 8.26 (s, 2H), 7.60 (s, 2H), 7.26 (br, 8H), 7.13 (br, 8H), 2.60 (br, 8H), 1 1.62 (m, 8H), 1.31 (m, 24H), 0.89 (m, 12H). Molecular weight: Mn= 33.4 k, PDI = 3.04.

Polymer films for CV characterization were prepared by spin coat 4 mg/mL polymer solution in chlorobenzene on to clean ITO substrate. Cyclic voltammetry was conducted in acetonitrile with 0.1 M of tetrabutylammonium hexafluorophosphate using a scan rate of 100 mVs^{-1}. ITO, Ag/AgCl, and Pt mesh were used as the working electrode, reference electrode, and counter electrode respectively. Films for PESA were coated using the same conditions mentioned above but on glass substrates. Samples were then well sealed and sent to Scott Watkins from CSIRO to characterized by PESA using a Riken Kekei AC-2 spectrometer. For UPS measurement, polymers were sent to Alex. L Briseño in University of Massachusetts. Polymer films were prepared at his lab by spin coating 2 mg/mL polymer solution in CB on gold (Au) deposited on ITO substrate at 4000 rpm. Both reference Au sample and polymer samples were prepared at same time, and were immediately transferred to vacuum chamber to perform the measurement. The photon energy used in the measurement was 21.22 eV.

Fabrication and Characterization of BHJ Devices. ITO/Glass substrates were ultrasonically cleaned sequentially in detergent, water, acetone and isopropyl alcohol. The substrates were covered by a 30 nm layer of PEDOT:PSS by spin coating. After annealing in air at 140 ºC for 10 min, the samples were cooled to room temperature. Polymers were dissolved in chlorobenzene (CB) at a concentration of 4 mg/mL and $PC_{61}BM$ was added to reach the optimized ratio (1:3). The solutions were then heated at 90 ºC and stirred overnight. Prior to deposition, the solutions were filtered through a 0.2 μm filter and the substrates were transferred into a glovebox. The photoactive layer was then spin coated at different speeds to get a thickness about 100 nm. The aluminum cathode (100 nm thick) was thermally evaporated through a shadow mask under high vacuum about 4.0×10^{-7} torr. Devices were then tested using a Keithley 2400 source measurement unit, and an Oriel Xenon lamp (450 W) coupled with an AM1.5 filter was used as the light source. The light intensity was calibrated with a calibrated standard silicon solar cell with a KG5 filter which is traced to the National Renewable Energy Laboratory and a light intensity of 100 $mW\bullet cm^{-2}$ was used in all the measurements in this study. Devices parameters were obtained by taking the average of 15 samples for each device.

4. Reference

1. U.S. Energy Information Adminstration, *2009 Annual Energy Review*, 2009
2. Purdue University, http://www.go-green.com/files/US 20CO2 20map.JPG
3. D. J. C. MacKay, *Sustainable Energy - Without the Hot Air*, UIT, 2009.
4. U.S. Energy Information Adminstration, *AEO2012 Early Release Overview*, .
5. National Renewable Energy Laboratory, .
6. R. Perez and http://solarenergyfactsblog. com/wp-content/uploads/2012/02/solar-energy-potential. pn. et al., *Solar Energy Potential*.
7. http://www.udel.edu/PR/UDaily/2008/jul/solar072307.html, *UD-led team sets solar cell record, joins DuPont on $100 million project*.
8. United States Department of Energy, .
9. B. A. Gregg, *J. Phys. Chem. B*, 2003, **107**, 4688–4698.
10. F. C. Krebs, *Sol. Energy Mater. Sol. Cells*, 2009, **93**, 394–412.
11. T. A. Skotheim, *Handbook of Conducting Polymers*, CRC Press, 2nd edn., 1997.
12. G. Hadziioannou and P. F. van Hutten, *Semiconducting Polymers: Chemistry, Physics, and Engineering*, Wiley-VCH, 2000.
13. B. Kippelen and J.-L. Brédas, *Energy Environ. Sci.*, 2009, **2**, 251.
14. B. J. Schwartz, *Nat Mater*, 2008, **7**, 427–428.
15. E. Collini and G. D. Scholes, *Science*, 2009, **323**, 369 –373.
16. J.-L. Brédas and R. Silbey, *Science*, 2009, **323**, 348 –349.
17. R. Österbacka, C. P. An, X. M. Jiang, and Z. V. Vardeny, *Science*, 2000, **287**, 839 –842.
18. F. C. Krebs, *Polymeric Solar Cells: Materials, Design, Manufacture*, DEStech Publications, Inc, 2010.

19. R. Tipnis, J. Bernkopf, S. Jia, J. Krieg, S. Li, M. Storch, and D. Laird, *Sol. Energy Mater. Sol. Cells*, 2009, **93**, 1457.

20. S. Günes, H. Neugebauer, and N. S. Sariciftci, *Chem. Rev.*, 2007, **107**, 1324–1338.

21. J. J. M. Halls, C. A. Walsh, N. C. Greenham, E. A. Marseglia, R. H. Friend, S. C. Moratti, and A. B. Holmes, *Nature*, 1995, **376**, 498–500.

22. F. Padinger, R. S. Rittberger, and N. S. Sariciftci, *Adv. Funct. Mater.*, 2003, **13**, 85–88.

23. H. Hoppe and N. S. Sariciftci, *J. Mater. Chem.*, 2006, **16**, 45.

24. K. Sivula, Z. T. Ball, N. Watanabe, and J. M. J. Fréchet, *Adv. Mater.*, 2006, **18**, 206–210.

25. W. Ma, C. Yang, X. Gong, K. Lee, and A. J. Heeger, *Adv. Funct. Mater.*, 2005, **15**, 1617–1622.

26. H. Hoppe, M. Niggemann, C. Winder, J. Kraut, R. Hiesgen, A. Hinsch, D. Meissner, and N. S. Sariciftci, *Adv. Funct. Mater.*, 2004, **14**, 1005–1011.

27. E. Ahlswede, J. Hanisch, and M. Powalla, *Appl.Phys.Lett.*, 2007, **90**, 163504.

28. Xiaoxia Jiang, Hao Xu c, Ligong Yang, Minmin Shi, Mang Wang, and Hongzheng Chen, *Sol. Energy Mater. Sol. Cells*, 2009, **1**, 1–4.

29. C. J. Brabec, S. E. Shaheen, C. Winder, N. S. Sariciftci, and P. Denk, *Appl.Phys.Lett.*, 2002, **80**, 1288–1290.

30. J. Y. Kim, S. H. Kim, H.-H. Lee, K. Lee, W. Ma, X. Gong, and A. J. Heeger, *Adv. Mater.*, 2006, **18**, 572–576.

31. S. H. Park, A. Roy, S. Beaupre, S. Cho, N. Coates, J. S. Moon, D. Moses, M. Leclerc, K. Lee, and A. J. Heeger, *Nat Photon*, 2009, **3**, 297–302.

32. L.-M. Chen, Z. Hong, G. Li, and Y. Yang, *Adv. Mater.*, 2009, **21**, 1434–1449.

33. G. Li, C.-W. Chu, V. Shrotriya, J. Huang, and Y. Yang, *Appl. Phys. Lett.*, 2006, **88**, 253503.

34. S. K. Hau, H. L. Yip, J. Zou, and A. K. . Jen, *Organic Electronics*, 2009, **10**, 1401–1407.

35. S. K. Hau, H.-L. Yip, H. Ma, and A. K.-Y. Jen, *Appl. Phys. Lett.*, 2008, **93**, 233304.

36. M. R. Lee, R. D. Eckert, K. Forberich, G. Dennler, C. J. Brabec, and R. A. Gaudiana, *Science*, 2009, **324**, 232–235.

37. J. Gilot, M. M. Wienk, and R. A. J. Janssen, *Appl. Phys. Lett.*, 2007, **90**, 143512–143512–3.

38. J. Y. Kim, K. Lee, N. E. Coates, D. Moses, T.-Q. Nguyen, M. Dante, and A. J. Heeger, *Science*, 2007, **317**, 222–225.

39. S. Sista, M.-H. Park, Z. Hong, Y. Wu, J. Hou, W. L. Kwan, G. Li, and Y. Yang, *Adv. Mater.*, 2009, **22**, 380–383.

40. J. Gilot, M. M. Wienk, and R. A. J. Janssen, *Adv. Mater.*, 2009, **22**, E67–E71.

41. T. Ameri, G. Dennler, C. Lungenschmied, and C. J. Brabec, *Energy Environ. Sci.*, 2009, **2**, 347.

42. A. Hadipour, B. de Boer, J. Wildeman, F. B. Kooistra, J. C. Hummelen, M. G. R. Turbiez, M. M. Wienk, R. a. J. Janssen, and P. W. M. Blom, *Adv. Funct. Mater.*, 2006, **16**, 1897–1903.

43. B. C. Thompson and J. M. J. Fréchet, *Angew. Chem. Int. Ed.*, 2008, **47**, 58–77.

44. E. Wang, L. Hou, Z. Wang, S. Hellström, F. Zhang, O. Inganäs, and M. R. Andersson, *Adv. Mater.*, 2010, **22**, 5240–5244.

45. H.-Y. Chen, J. Hou, S. Zhang, Y. Liang, G. Yang, Y. Yang, L. Yu, Y. Wu, and G. Li, *Nat. Photon.*, 2009, **3**, 649–653.

46. H.-Y. Chen, J. Hou, A. E. Hayden, H. Yang, K. N. Houk, and Y. Yang, *Adv. Mater.*, 2009, **22**, 371–375.

47. T.-Y. Chu, J. Lu, S. Beaupré, Y. Zhang, J.-R. Pouliot, S. Wakim, J. Zhou, M. Leclerc, Z. Li, J. Ding, and Y. Tao, *J. Am. Chem. Soc.*, 2011, **133**, 4250–4253.

48. P. Boland, S. S. Sunkavalli, S. Chennuri, K. Foe, T. Abdel-Fattah, and G. Namkoong, *Thin Solid Films*, 2010, **518**, 1728–1731.

49. P. Boland and G. Namkoong, *Jpn. J. Appl. Phys.*, 2010, **49**, 030205.

50. G. Zhao, Y. He, and Y. Li, *Adv. Mater.*, 2010, **22**, 4355–4358.

51. Z. He, C. Zhong, X. Huang, W.-Y. Wong, H. Wu, L. Chen, S. Su, and Y. Cao, *Adv. Mater.*, 2011, **23**, 4636–4643.

52. M. C. Scharber, D. Mühlbacher, M. Koppe, P. Denk, C. Waldauf, A. J. Heeger, C. J. Brabec, M. C. Scharber, D. Mühlbacher, M. Koppe, P. Denk, C. Waldauf, A. J. Heeger, and C. J. Brabec, *Adv. Mater.*, 2006, **18, 18**, 789, 789–794, 794.

53. E. Bundgaard and F. C. Krebs, *Sol. Energy Mater. Sol. Cells*, 2007, **91**, 954–985.

54. A. J. Moulé and K. Meerholz, *Adv. Funct. Mater.*, 2009, **19**, 3028–3036.

55. C. J. Brabec, S. Gowrisanker, J. J. M. Halls, D. Laird, S. Jia, and S. P. Williams, *Adv. Mater.*, 2010, **22**, 3839–3856.

56. F. Padinger, R. S. Rittberger, and N. S. Sariciftci, *Adv. Funct. Mater.*, 2003, **13**, 85–88.

57. T. Erb, U. Zhokhavets, G. Gobsch, S. Raleva, B. Stühn, P. Schilinsky, C. Waldauf, and C. J. Brabec, *Adv. Funct. Mater.*, 2005, **15**, 1193–1196.

58. F. Demir, N. Brande, B. Mele, S. Bertho, D. Vanderzande, J. Manca, and G. Assche, *J. Therm. Anal. Calorim.*, 2011, **105**, 845–849.

59. G. Li, Y. Yao, H. Yang, V. Shrotriya, G. Yang, and Y. Yang, *Adv. Funct. Mater.*, 2007, **17**, 1636–1644.

60. G. Li, V. Shrotriya, J. Huang, Y. Yao, T. Moriarty, K. Emery, and Y. Yang, *Nat. Mater.*, 2005, **4**, 864–868.

61. G. Wei, R. R. Lunt, K. Sun, S. Wang, M. E. Thompson, and S. R. Forrest, *Nano Lett.*, 2010, **10**, 3555–3559.

62. F. Zhang, K. G. Jespersen, C. Björström, M. Svensson, M. R. Andersson, V. Sundström, K. Magnusson, E. Moons, A. Yartsev, and O. Inganäs, *Adv. Funct. Mater.*, 2006, **16**, 667–674.

63. J. K. Lee, W. L. Ma, C. J. Brabec, J. Yuen, J. S. Moon, J. Y. Kim, K. Lee, G. C. Bazan, and A. J. Heeger, *J. Am. Chem. Soc.*, 2008, **130**, 3619–3623.

64. H. Xin, X. Guo, G. Ren, M. D. Watson, and S. A. Jenekhe, *Adv. Energy Mater.*, 2012, **2**, 575–582.

65. *ASTM International*, 2006.

66. A. Luque and S. Hegedus, *Handbook of Photovoltaic Science and Engineering*, John Wiley & Sons, 2011.

67. Q. Zhang, T. P. Chou, B. Russo, S. A. Jenekhe, and G. Cao, *Angew. Chem. Int. Ed.*, 2008, **47**, 2402–2406.

68. Q. Zhang, T. P. Chou, B. Russo, S. A. Jenekhe, and G. Cao, *Adv. Funct. Mater.*, 2008, **18**, 1654–1660.

69. Q. Zhang, C. S. Dandeneau, X. Zhou, and G. Cao, *Adv. Mater.*, 2009, **21**, 4087–4108.

70. J.-F. Chang, B. Sun, D. W. Breiby, M. M. Nielsen, T. I. Sölling, M. Giles, I. McCulloch, and H. Sirringhaus, *Chem. Mater.*, 2004, **16**, 4772–4776.

71. X. Yang, J. Loos, S. C. Veenstra, W. J. H. Verhees, M. M. Wienk, J. M. Kroon, M. A. J. Michels, and R. A. J. Janssen, *Nano Lett.*, 2005, **5**, 579–583.

72. W.-H. Baek, H. Yang, T.-S. Yoon, C. J. Kang, H. H. Lee, and Y.-S. Kim, *Sol. Energy Mater. Sol. Cells*, 2009, **93**, 1263–1267.

73. Z. Xu, L. Chen, G. Yang, C. Huang, J. Hou, Y. Wu, G. Li, C. Hsu, and Y. Yang, *Adv. Funct. Mater.*, 2009, **19**, 1227–1234.

74. H. Hoppe and N. S. Sariciftci, *J. Mater. Res.*, 2011, **19**, 1924–1945.

75. A. G. Jones, C. Balocco, R. King, and A. M. Song, *Appl. Phys. Lett.*, 2006, **89**, 013119.

76. G. Li, V. Shrotriya, Y. Yao, and Y. Yang, *J. Appl. Phys.*, 2005, **98**, 043704.

77. H. Ohkita, S. Cook, Y. Astuti, W. Duffy, S. Tierney, W. Zhang, M. Heeney, I. McCulloch, J. Nelson, D. D. C. Bradley, and J. R. Durrant, *J. Am. Chem. Soc.*, 2008, **130**, 3030–3042.

78. C. Goh, R. J. Kline, M. D. McGehee, E. N. Kadnikova, and J. M. J. Fréchet, *Appl. Phys. Lett.*, 2005, **86**, 122110.

79. P. Yang, X. Zhou, G. Cao, and C. K. Luscombe, *J. Mater. Chem.*, 2010, **20**, 2612–2616.

80. B. Liu and E. S. Aydil, *J. Am. Chem. Soc.*, 2009, **131**, 3985–3990.

81. E. Hosono, S. Fujihara, K. Kakiuchi, and H. Imai, *J. Am. Chem. Soc.*, 2004, **126**, 7790–7791.

82. J.-M. Wu, H. C. Shih, and W.-T. Wu, *Nanotechnology*, 2006, **17**, 105–109.

83. J.-J. Wu and C.-C. Yu, *J Phys. Chem. B*, 2004, **108**, 3377–3379.

84. G. K. Mor, K. Shankar, M. Paulose, O. K. Varghese, and C. A. Grimes, *Nano Lett.*, 2005, **6**, 215–218.

85. K. Zhu, N. R. Neale, A. Miedaner, and A. J. Frank, *Nano Lett.*, 2006, **7**, 69–74.

86. B. Liu and E. S. Aydil, *J. Am. Chem. Soc.*, 2009, **131**, 3985–3990.

87. V. D. Mihailetchi, H. X. Xie, B. de Boer, L. J. A. Koster, and P. W. M. Blom, *Adv. Funct. Mater.*, 2006, **16**, 699–708.

88. V. Schmidt, J. V. Wittemann, S. Senz, and U. Gösele, *Adv. Mater.*, 2009, **21**, 2681–2702.

89. M. T. Bj| [ouml]|rk, H. Schmid, J. Knoch, H. Riel, and W. Riess, *Nat. Nanotechnol.*, 2009, **4**, 103.

90. B. Weber, S. Mahapatra, H. Ryu, S. Lee, A. Fuhrer, T. C. G. Reusch, D. L. Thompson, W. C. T. Lee, G. Klimeck, L. C. L. Hollenberg, and M. Y. Simmons, *Science*, 2012, **335**, 64–67.

91. Y.-Y. Lin, T.-H. Chu, S.-S. Li, C.-H. Chuang, C.-H. Chang, W.-F. Su, C.-P. Chang, M.-W. Chu, and C.-W. Chen, *J. Am. Chem. Soc.*, 2009, **131**, 3644–3649.

92. Y.-Y. Lin, T.-H. Chu, C.-W. Chen, and W.-F. Su, *Appl. Phys. Lett.*, 2008, **92**, 053312–053312–3.

93. H.-C. Liao, C.-H. Lee, Y.-C. Ho, M.-H. Jao, C.-M. Tsai, C.-M. Chuang, J.-J. Shyue, Y.-F. Chen, and W.-F. Su, *J. Mater. Chem.*, 2012, **22**, 10589.

94. P. Yang, D. K. Zhong, M. Yuan, A. H. Rice, D. R. Gamelin, and C. K. Luscombe, *Phys. Chem. Chem. Phys.*, 2013, **15**, 4566–4572.

95. F. Fabregat-Santiago, G. Garcia-Belmonte, I. Mora-Seró, and J. Bisquert, *Phys. Chem. Chem. Phys.*, 2011, **13**, 9083–9118.

96. T. Hoshikawa, R. Kikuchi, and K. Eguchi, *Journal of Electroanalytical Chemistry*, 2006, **588**, 59–67.

97. J. Bisquert, *J. Phys. Chem. B*, 2002, **106**, 325–333.

98. Q. Wang, S. Ito, M. Grätzel, F. Fabregat-Santiago, I. Mora-Seró, J. Bisquert, T. Bessho, and H. Imai, *J. Phys. Chem. B*, 2006, **110**, 25210–25221.

99. J. Bisquert, F. Fabregat-Santiago, I. Mora-Seró, G. Garcia-Belmonte, and S. Giménez, *J. Phys. Chem. C*, 2009, **113**, 17278–17290.

100. V. González-Pedro, X. Xu, I. Mora-Seró, and J. Bisquert, *ACS Nano*, 2010, **4**, 5783–5790.

101. H. Lee, M. Wang, P. Chen, D. R. Gamelin, S. M. Zakeeruddin, M. Grätzel, and M. K. Nazeeruddin, *Nano Lett.*, 2009, **9**, 4221–4227.

102. F. Fabregat-Santiago, J. Bisquert, L. Cevey, P. Chen, M. Wang, S. M. Zakeeruddin, and M. Grätzel, *J. Am. Chem. Soc.*, 2009, **131**, 558–562.

103. M. Wang, P. Chen, R. Humphry-Baker, S. M. Zakeeruddin, and M. Grätzel, *ChemPhysChem*, 2009, **10**, 290–299.

104. J. Bisquert, *J. Phys. Chem. B*, 2002, **106**, 325–333.

105. T. Ripolles-Sanchis, A. Guerrero, J. Bisquert, and G. Garcia-Belmonte, *J. Phys. Chem. C*, 2012, **116**, 16925–16933.

106. G. Garcia-Belmonte, P. P. Boix, J. Bisquert, M. Sessolo, and H. J. Bolink, *Solar Energy Materials and Solar Cells*, 2010, **94**, 366–375.

107. Y.-Y. Lin, T.-H. Chu, S.-S. Li, C.-H. Chuang, C.-H. Chang, W.-F. Su, C.-P. Chang, M.-W. Chu, and C.-W. Chen, *J. Am. Chem. Soc.*, 2009, **131**, 3644–3649.

108. Y.-C. Huang, J.-H. Hsu, Y.-C. Liao, W.-C. Yen, S.-S. Li, S.-T. Lin, C.-W. Chen, and W.-F. Su, *J. Mater. Chem.*, 2011, **21**, 4450–4456.

109. Y.-Y. Lin, T.-H. Chu, C.-W. Chen, and W.-F. Su, *Appl. Phys. Lett.*, 2008, **92**, 053312–053312–3.

110. M. Jankulovska, T. Berger, S. S. Wong, R. Gómez, and T. Lana-Villarreal, *ChemPhysChem*, 2012, **13**, 3008–3017.

111. S. H. Kang, J.-Y. Kim, Y. Kim, H. S. Kim, and Y.-E. Sung, *J. Phys. Chem. C*, 2007, **111**, 9614–9623.

112. E. Enache-Pommer, J. E. Boercker, and E. S. Aydil, *Appl. Phys. Lett.*, 2007, **91**, 123116–123116–3.

113. S. H. Yoo, J. M. Kum, and S. O. Cho, *Nanoscale. Res. Lett.*, 2011, **6**, 1–7.

114. Y. Gao, X. Pu, D. Zhang, G. Ding, X. Shao, and J. Ma, *Carbon*, 2012, **50**, 4093–4101.

115. G. Garcia-Belmonte, A. Munar, E. M. Barea, J. Bisquert, I. Ugarte, and R. Pacios, *Organic Electronics*, 2008, **9**, 847–851.

116. J. Bisquert, G. Garcia-Belmonte, A. Munar, M. Sessolo, A. Soriano, and H. J. Bolink, *Chemical Physics Letters*, 2008, **465**, 57–62.

117. S. K. Hau, H.-L. Yip, O. Acton, N. S. Baek, H. Ma, and A. K.-Y. Jen, *J. Mater. Chem.*, 2008, **18**, 5113–5119.

118. C.-H. Chen, C.-H. Hsieh, M. Dubosc, Y.-J. Cheng, and C.-S. Hsu, *Macromol.*, 2009, **43**, 697–708.

119. M. Yuan, A. H. Rice, and C. K. Luscombe, *J. Polym. Sci., Part A: Polym. Chem.*, 2011, **49**, 701–711.

120. A. B. Tamayo, X.-D. Dang, B. Walker, J. Seo, T. Kent, and T.-Q. Nguyen, *Appl. Phys. Lett.*, 2009, **94**, 103301–103301–3.

121. J. You, L. Dou, K. Yoshimura, T. Kato, K. Ohya, T. Moriarty, K. Emery, C.-C. Chen, J. Gao, G. Li, and Y. Yang, *Nat. Commun.*, 2013, **4**, 1446.

122. Y.-J. Cheng, S.-H. Yang, and C.-S. Hsu, *Chem. Rev.*, 2009, **109**, 5868–5923.

123. Y. Zou, A. Najari, P. Berrouard, S. Beaupré, B. Réda Ai□ch, Y. Tao, and M. Leclerc, *J. Am. Chem. Soc.*, 2010, **132**, 5330–5331.

124. J.-Y. Wang, S. K. Hau, H.-L. Yip, J. A. Davies, K.-S. Chen, Y. Zhang, Y. Sun, and A. K.-Y. Jen, *Chem. Mater.*, 2010, **23**, 765–767.

125. L. Yang, J. R. Tumbleston, H. Zhou, H. Ade, and W. You, *Energy Environ. Sci.*, 2012, **6**, 316–326.

126. Y.-J. Cheng, J.-S. Wu, P.-I. Shih, C.-Y. Chang, P.-C. Jwo, W.-S. Kao, and C.-S. Hsu, *Chem. Mater.*, 2011, **23**, 2361–2369.

127. N. C. Cates, R. Gysel, Z. Beiley, C. E. Miller, M. F. Toney, M. Heeney, I. McCulloch, and M. D. McGehee, *Nano Lett.*, 2009, **9**, 4153–4157.

128. S. Yue, G. C. Berry, and R. D. McCullough, *Macromol.*, 1996, **29**, 933–939.

129. D. A. M. Egbe, L. H. Nguyen, H. Hoppe, D. Mühlbacher, and N. S. Sariciftci, *Macromolecular Rapid Communications*, 2005, **26**, 1389–1394.

130. C. Du, C. Li, W. Li, X. Chen, Z. Bo, C. Veit, Z. Ma, U. Wuerfel, H. Zhu, W. Hu, and F. Zhang, *Macromol.*, 2011, **44**, 7617–7624.

131. M. Yuan, K. Okamoto, H. A. Bronstein, and C. K. Luscombe, *ACS Macro Lett.*, 2012, **1**, 392–395.

132. Y.-J. Cheng, C.-H. Chen, Y.-S. Lin, C.-Y. Chang, and C.-S. Hsu, *Chem. Mater.*, 2011, **23**, 5068–5075.

133. Y.-J. Cheng, Y.-J. Ho, C.-H. Chen, W.-S. Kao, C.-E. Wu, S.-L. Hsu, and C.-S. Hsu, *Macromol.*, 2012, **45**, 2690–2698.

134. Y.-J. Cheng, S.-W. Cheng, C.-Y. Chang, W.-S. Kao, M.-H. Liao, and C.-S. Hsu, *Chem. Commun.*, 2012, **48**, 3203.

135. H. Usta, G. Lu, A. Facchetti, and T. J. Marks, *J. Am. Chem. Soc.*, 2006, **128**, 9034–9035.

136. H. Chen, J. Hou, A. E. Hayden, H. Yang, K. N. Houk, and Y. Yang, *Adv. Mater.*, 2010, **22**, 371–375.

137. M. Morana, H. Azimi, G. Dennler, H. Egelhaaf, M. Scharber, K. Forberich, J. Hauch, R. Gaudiana, D. Waller, Z. Zhu, K. Hingerl, S. S. van Bavel, J. Loos, and C. J. Brabec, *Adv. Funct. Mater.*, 2010, **20**, 1180–1188.

138. Y.-J. Cheng, S.-H. Yang, and C.-S. Hsu, *Chem. Rev.*, 2009, **109**, 5868–5923.

139. C. He, Q. He, X. Yang, G. Wu, C. Yang, F. Bai, Z. Shuai, L. Wang, and Y. Li, *J. Phys. Chem. C*, 2007, **111**, 8661–8666.

140. B. Walker, A. B. Tamayo, X. Dang, P. Zalar, J. H. Seo, A. Garcia, M. Tantiwiwat, and T. Nguyen, *Adv. Funct. Mater.*, 2009, **19**, 3063–3069.

141. N. C. Cates, R. Gysel, J. E. P. Dahl, A. Sellinger, and M. D. McGehee, *Chem. Mater.*, 2010, **22**, 3543–3548.

142. A. C. Mayer, M. F. Toney, S. R. Scully, J. Rivnay, C. J. Brabec, M. Scharber, M. Koppe, M. Heeney, I. McCulloch, and M. D. McGehee, *Adv. Funct. Mater.*, 2009, **19**, 1173–1179.

143. L. Huo, J. Hou, S. Zhang, H. Chen, and Y. Yang, *Angew. Chem. Int. Ed.*, 2010, **49**, 1500–1503.

144. S. C. Price, A. C. Stuart, L. Yang, H. Zhou, and W. You, *J. Am. Chem. Soc.*, 2011, **133**, 4625–4631.

145. Y. Liang, Z. Xu, J. Xia, S.-T. Tsai, Y. Wu, G. Li, C. Ray, and L. Yu, *Adv. Mater.*, 2010, **22**, E135–E138.

146. H. Zhou, L. Yang, A. C. Stuart, S. C. Price, S. Liu, and W. You, *Angew. Chem. Int. Ed.*, 2011, **50**, 2995–2998.

147. H.-Y. Chen, J. Hou, S. Zhang, Y. Liang, G. Yang, Y. Yang, L. Yu, Y. Wu, and G. Li, *Nat. Photon.*, 2009, **3**, 649–653.

148. Z. Li, J. Lu, S.-C. Tse, J. Zhou, X. Du, Y. Tao, and J. Ding, *J. Mater. Chem.*, 2011, **21**, 3226–3233.

149. S. C. Price, A. C. Stuart, L. Yang, H. Zhou, and W. You, *J. Am. Chem. Soc.*, 2011, **133**, 4625–4631.

150. Hsiang-Yu Chen, Jianhui Hou, Shaoqing Zhang, Yongye Liang, Guanwen Yang, Yang Yang, Luping Yu, Yue Wu, and Gang Li, *Nature Photonics*, 2009, **3**, 649–653.

151. A. C. Stuart, J. R. Tumbleston, H. Zhou, W. Li, S. Liu, H. Ade, and W. You, *J. Am. Chem. Soc.*, 2013, **135**, 1806–1815.

152. P. Heremans, D. Cheyns, and B. P. Rand, *Accounts of Chemical Research*, 2009, **42**, 1740–1747.

153. S. Günes, H. Neugebauer, and N. S. Sariciftci, *Chem. Rev.*, 2007, **107**, 1324–1338.

154. Y. Zhang, J. Zou, C.-C. Cheuh, H.-L. Yip, and A. K.-Y. Jen, *Macromolecules*, 2012, **45**, 5427–5435.

155. B. C. Schroeder, R. S. Ashraf, S. Thomas, A. J. P. White, L. Biniek, C. B. Nielsen, W. Zhang, Z. Huang, P. S. Tuladhar, S. E. Watkins, T. D. Anthopoulos, J. R. Durrant, and I. McCulloch, *Chem. Commun.*, 2012, **48**, 7699–7701.

156. B. Carsten, J. M. Szarko, H. J. Son, W. Wang, L. Lu, F. He, B. S. Rolczynski, S. J. Lou, L. X. Chen, and L. Yu, *J. Am. Chem. Soc.*, 2011, **133**, 20468–20475.

157. L. Yang, J. R. Tumbleston, H. Zhou, H. Ade, and W. You, *Energy Environ. Sci.*, 2012, **6**, 316–326.

158. M. Yuan, P. Yang, M. M. Durban, and C. K. Luscombe, *Macromolecules*, 2012, **45**, 5934–5940.

159. T. M. McCormick, C. R. Bridges, E. I. Carrera, P. M. DiCarmine, G. L. Gibson, J. Hollinger, L. M. Kozycz, and D. S. Seferos, *Macromolecules*, 2013, **46**, 3879–3886.

160. S. C. Price, A. C. Stuart, L. Yang, H. Zhou, and W. You, *J. Am. Chem. Soc.*, 2011, **133**, 4625–4631.

161. A. Gadisa, M. Svensson, M. R. Andersson, and O. Inganäs, *Applied Physics Letters*, 2004, **84**, 1609–1611.

162. M. F. Lo, T. W. Ng, T. Z. Liu, V. A. L. Roy, S. L. Lai, M. K. Fung, C. S. Lee, and S. T. Lee, *Applied Physics Letters*, 2010, **96**, 113303–113303–3.

163. J. A. Mikroyannidis, A. N. Kabanakis, S. S. Sharma, and G. D. Sharma, *Adv. Funct. Mater.*, 2011, **21**, 746–755.

164. S. H. Yoo, J. M. Kum, and S. O. Cho, *Nanoscale Res Lett*, 2011, **6**, 545.

165. M. A. Loi, S. Toffanin, M. Muccini, M. Forster, U. Scherf, and M. Scharber, *Adv. Funct. Mater.*, 2007, **17**, 2111–2116.

166. C. Deibel, T. Strobel, and V. Dyakonov, *Adv. Mater.*, 2010, **22**, 4097–4111.

167. K. Vandewal, A. Gadisa, W. D. Oosterbaan, S. Bertho, F. Banishoeib, I. Van Severen, L. Lutsen, T. J. Cleij, D. Vanderzande, and J. V. Manca, *Adv. Funct. Mater.*, 2008, **18**, 2064–2070.

168. B. Yang, J. Cox, Y. Yuan, F. Guo, and J. Huang, *Appl. Phys. Lett.*, 2011, **99**, 133302–133302–3.

169. M. Hallermann, I. Kriegel, E. Da Como, J. M. Berger, E. von Hauff, and J. Feldmann, *Adv. Funct. Mater.*, 2009, **19**, 3662–3668.

170. Y. Zhang, S.-C. Chien, K.-S. Chen, H.-L. Yip, Y. Sun, J. A. Davies, F.-C. Chen, and A. K.-Y. Jen, *Chem. Commun.*, 2011, **47**, 11026–11028.

171. L. Huo, S. Zhang, X. Guo, F. Xu, Y. Li, and J. Hou, *Angew. Chem. Int. Ed.*, 2011, **50**, 9697–9702.

172. Y. Zhang, J. Zou, H.-L. Yip, K.-S. Chen, D. F. Zeigler, Y. Sun, and A. K.-Y. Jen, *Chem. Mater.*, 2011, **23**, 2289–2291.